STRUCTURE DESIGN AND PROPERTY STUDY OF II-VI, VI-VI AND I-VII

BASED INORGANIC-ORGANIC HYBRID SEMICONDUCTORS

by

XIAO ZHANG

A Dissertation submitted to the

Graduate School – New Brunswick

Rutgers, The State University of New Jersey

in partial fulfillment of the requirements

for the degree of

Doctor of Philosophy

Graduate Program in Chemistry and Chemical Biology

written under the direction of

Professor Jing Li

and approved by

_____

_____

_____

_____

New Brunswick, New Jersey

May 2013

ABSTRACT OF THE DISSERTATION

Structure Design and Property Study of II-VI, VI-VI AND I-VII Based Inorganic-

Organic Hybrid Semiconductors

By XIAO ZHANG

Dissertation Director:

Professor Jing Li

We have developed and studied selected properties of three novel classes
of inorganic organic hybrid semiconductors based on II-VI, VI-VI and I-VII
binary phases in order to enhance the functionality over their parent structures.

As a continuing effort, we have synthesized, modified, and characterized
a number of selected structures of II-VI inorganic organic hybrid materials with
general formula ZnSe(L)$_{0.5}$ (L = *organic diamine*). The thermal expansion
coefficients along the layer stacking (L$_3$) axis are between -1×10^{-6} and 4×10^{-6} K^{-1}
in the temperature range between 5K and 300K for all structures, indicating a
nearly-zero linear thermal expansion in the direction. A very small negative

thermal expansion coefficient of -7.8×10^{-7} K^{-1} is achieved for ZnSe(*ptda*)$_{0.5}$ along the L$_3$ axis, which is among the smallest values reported to date.

Secondly, we have designed a new class of inorganic organic hybrid semiconductors under mild solvothermal conditions. By controlling the dimensionality and topology of the VI-VI inorganic component using organic spacers, hybrid semiconductors with tunable optical properties can be effectively designed. The new VI-VI hybrid structures display the low thermal conductivities and high dielectric constants caused by interface induced phonon scattering and space charge polarization respectively. A significant negative thermal expansion behavior was also observed in some of the new VI-VI hybrid structures.

To further explore the unique properties of inorganic organic hybrid semiconductors, we have developed a novel class of I-VII inorganic organic hybrid semiconductors. A number of new 1D-CuI(*L*) (*L* = organic ligand) inorganic organic hyrbid materials were acquired using a solvent diffusion method. The 1D-CuI(*L*) hybrid structures display tunable optical absorption and emission behavior with some structures able to give close-to–white-light photoluminesence. By adjusting the functional group on the organic molecules, their LUMO energy levels and the band gap of hybrid structures can be

systematically tuned. This discovery further leads us to design ligand substituted 1D-CuI(*L*) structures to attain white light emission. We have successfully syntheisized pyrimidine substituted CuI(*pyridine*) crystals which demonstrate pure and strong white light emission, with the CIE cordinates of (0.31,0.33) under the UV excitation.

Acknowledgement

First, I would like to express my deepest gratitude to my supervisor, Prof. Jing Li, who has provided me an opportunity to work and study in her laboratory while providing me constant support, guidance, and encouragement throughout my graduate career. Her enthusiasm and hard-working spirit have set an example for me, which never fails to inspire me to overcome all the obstacles I meet both in my career and life.

I would also like to give thanks to China Scholarship Council and Rutgers University for the financial support during my Ph.D study.

I gratefully thank Prof. Ki-Bum Lee, Prof. Tewodros Asefa, and Dr. Long Pan, not only for serving on my thesis committee, but also for their valuable advice and suggestions.

Many thanks to current and former group members for all the support and for creating a joyful work environment. I would especially like to thank Mojgan Roushan for coaching me in the synthesis and characterization of inorganic organic hybrid semiconductors as well encouraging me to work hard on this challenging project. Moreover, I would like to thank Dr. Debasis Banerjee for his hard work, solving the many crystal structures. Without his help, I could not have nearly made nearly as much progress in the project of I-VII inorganic organic hybrid semiconductor project in such a short period of time as I have. Also I would like to thank all the undergraduate and high

school students who worked with me: George, Jon and Pratyusha. I want to give my greatest appreciation especially to George, who has worked very hard this year and shared the pressures of a last year graduate student with me.

I would also like to thank our collaborators: Mehdi, Raj, Bill, Wenqian, Vishnu, Yang, Tom, Ronggui and Suraj for helping me with different measurements.

I am also grateful to my parents for their love, encouragement and support.

Lastly I thank my wife, Qihan Gong, for her constant encouragement and advice during my years of graduate work. Without her love and constant support, I would not have the necessary diligence to complete this work.

Table of Contents

List of Tables

List of Figures

xix

1. Introduction

Besides the stability and rigidity of the crystal structure, the superior properties of solid state materials, such as electronic, optical and magnetic properties, have made inorganic materials highly attractive in the search for new semiconducting materials. Organic compounds built upon molecular building-blocks hold great promises for flexibility, structural diversity, and processability. They also possess a strong potential for the systematic control of size, shape, and symmetry. Integration and combination of the two counterparts into a single crystal lattice may generate inorganic-organic hybrid crystalline materials that enhance or combine the useful properties of both components. Based on this consideration, we and others have made great effort to develop new inorganic organic hybrid materials with different types and combinations of inorganic and organic chemicals inside the crystal structure and to explore their unique physical properties.[1] Many examples have been reported in which organic species enter the inorganic structures through either ionic bonding or relatively weak H-bonding and van der Waals interactions.[2-5] However, inorganic organic covalent architectures with explicit bonding directions between electrically neutral inorganic clusters and organic molecules are needed, but rare.[6] Therefore, our research group has laid a focus on this area in the past 10 years and has developed an unprecedented class of organic- inorganic hybrid materials.[7-10] With a general formula of [MQ(L)$_x$](M = Mn, Zn, Cd; Q = S, Se, Te; L=

mono- or diamine, x = 0.5 or 1), these crystalline hybrid structures are extended one-, two- and three- dimensional networks that are made of alternating II–VI binary semiconductor (inorganic component) modules and organic amines (organic component) at nano- or sub-nanometer scale and in periodic arrangement by coordinate bonds. (see Figure 1) These new types of hybrid structures possess a number of enhanced properties over their parent II–VI semiconductors, as well as interesting new phenomena derived from blending of the two distinctively different components in a single crystal lattice.[11]
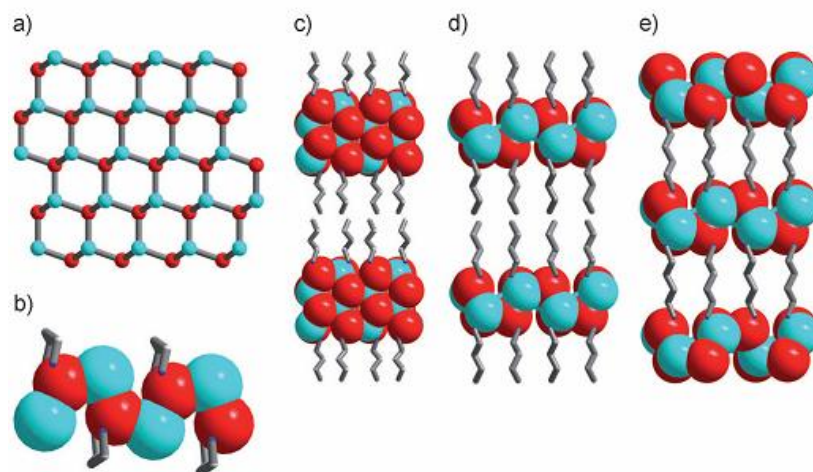
Figure 1[11]: View of a) single layer of honeycomb-like net of ZnS in the [MnQn(L)x]-type hybrid structure (M=Zn, Cd; Q=S, Se, Te; L = mono- or diamine), b) single-chain 1D-[MQ(L)] structure, c) double-layer 2D-[M$_2$Q$_2$(L)] structure, d) single-layer 2D-[MQ(L)] structure, and e) single-layer 3D-[MQ(L)$_{0.5}$] structure. Blue M, red Q, in (b)–(d) the stick model corresponds to L. (Reproduced with permission from ref 11. Copyright © 2012 WILEY-VCH Verlag GmbH & Co. KGaA, Weinheim.)

One important property found in the II-VI inorganic organic hybrid structures is UV light excited direct white light emission which was first demonstrated in $Cd_2S_2(ba)$ (ba = 1-butylamine)[12]. The broad emission covers the entire visible spectrum from 400 nm to 750 nm, and interestingly, the band edge emission is significantly reduced, leading to a well-balanced white-light spectrum. The compound has been proved to be the first semiconductor bulk materials that is capable of generating direct white light and has potential application in LEDs as a single-phase white-light emitting diode. More importantly, these hybrid semiconductors have kept perfectly ordered and extended (infinite) structures as their parent II-VI semiconductors and, thus, are capable of attaining high carrier conductivity and mobility that are necessary for high-efficiency light-emitting diodes.

Although the first discovery is inspiring, the results only serve as a concept proving case because their quantum efficiency is very low (quantum yield is around 4–5%). In an effort to enhance the performance of this type of materials we have further developed a series of ZnS based $[Zn_2S_2(L)]$ (L=propylamine (pa), butylamine (ba), hexylamine (ha), and octylamine (oa)) compounds with the same space group that are built on 2D nano-modules of ZnS with a uniform layer thickness. Investigation of their emission properties reveals drastically improved quantum efficiencies over the CdQ (Q = S, Se) based hybrid structures.[11] An optimized composition of $[Zn_{1.7}Cd_{0.3}S_2(ha):Mn]$ gives rise to a strong and well-balanced white light emission, as shown in Figure 2. The

International Commission on Illumination (CIE) coordinates of [$Zn_{1.7}Cd_{0.3}S_2$(ha):Mn] are calculated to be (0.31, 0.29), which are well within the white region of the colour space chromaticity diagram. The quantum yield has also been strongly enhanced to 31–37%, a value that is approaching some of the phosphors currently used in commercial WLED productions.
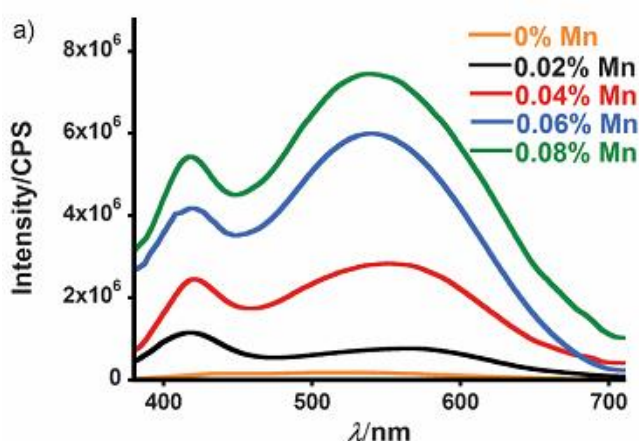
Figure 2[11]: White-light emission spectra of [$Zn_{1.7}Cd_{0.3}S_2$(*ha*):Mn] at various Mn concentrations (λ_{ex} =365 nm). (Reproduced with permission from ref 11. Copyright © 2012 WILEY-VCH Verlag GmbH & Co. KGaA, Weinheim.)

Another interesting phenomenon found in II-VI inorganic organic hybrid materials is nearly zero thermal expansion (ZTE). In general crystal structures expand when the temperature increase and contract when the temperature decrease, so there are very few materials exhibit zero thermal expansion, that is, the length and volume of the material are independent of temperature change. This phenomenon is even rare with the materials which are appropriate for electronic and optoelectronic applications.[13] The first

inorganic organic hybrid structure to demonstrate the zero thermal expansion is ZnTe(en)$_{0.5}$ (en denotes ethylenediamine) which showed uniaxial ZTE in a very broad temperature range of 4–400 K, and concurrently possesses superior electronic and optical properties. The ZTE behavior is caused by the compensation of contraction and expansion of different segments along the inorganic-organic stacking axis.[14] To be specific, the inorganic component (ZnTe) remains to be positive thermal expansion (PTE) but the organic diamine shows strong negative thermal expansion NTE in the hybrid structure. This study suggests that hybrid structures may have the following advantages as possible candidates for ZTE materials: (a) ZTE may be achieved by the two opposing effect (PTE and NTE) within a single crystal lattice to avoid grain boundary associated cracks, and (b) both PTE and NTE can be independently and systematically tuned by varying the inorganic layers and organic molecules.[15]
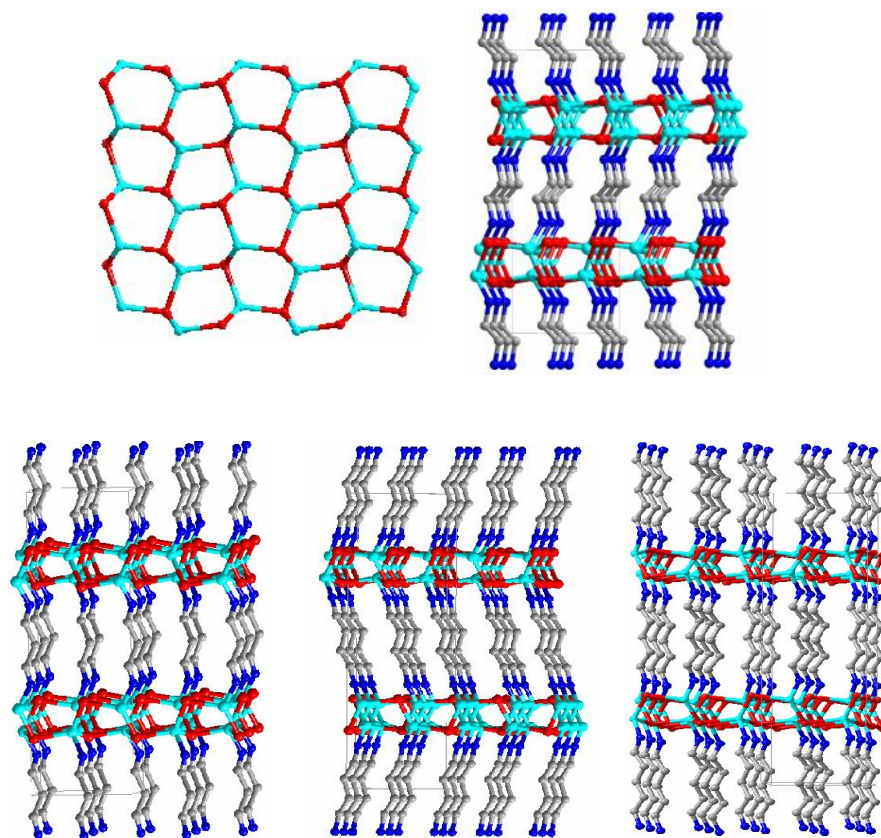
Figure 3: Refined crystal structures of α-[ZnSe(L)$_{0.5}$] series. (a) ZnSe single-atomic slab. (b) α-[ZnSe(en)$_{0.5}$] (**1**), (c) α-[ZnSe(pda)$_{0.5}$] (**2**), (d) α-[ZnSe(bda)$_{0.5}$] (**3**), (e) α-[ZnSe($ptda$)$_{0.5}$] (**4**). Hydrogen atoms are omitted for clarity. (Reproduced with permission from ref 16. Copyright © 2012 WILEY-VCH Verlag GmbH & Co. KGaA, Weinheim.)

As an extension of previous work, we report a family of inorganic-organic hybrid semiconductors with a general formula of ZnSe(L)$_{0.5}$ (L = organic diamine) that exhibit nearly-zero thermal expansion along the layer-stacking axis in the temperature range of 5-300K.[16] The unit cell parameters and crystal structures of ZnSe(en)$_{0.5}$, ZnSe(pda)$_{0.5,}$

ZnSe(*bda*)$_{0.5}$ and ZnSe(*ptda*)$_{0.5}$ (*en* = ethylenediamine, *pda* = propanediamine, *bda* = butanediamine, and *ptda* = pentanediamine) are refined by Rietveld method using powder samples, and their thermal expansion properties are analyzed and rationalized based on their crystal structures and symmetry. ZnSe(*ptda*)$_{0.5}$ features a very small negative linear thermal expansion coefficient (-7.8×10^{-7} K^{-1}) that approaches the smallest values reported to date. Details about the results will be discussed in Chapter 1

Inspired by the success obtained from II-VI chalcogenide derived hybrid semiconductors, we are further looking into important oxide semiconductors as parent structures for new hybrid systems. The WO_3 and MoO_3 semiconductors and their derivatives have been extensively studied owing to their unusual electric, optic and thermal properties with many potential applications.[17-32] For example, WO_3 has widely been studied in photochemical water oxidation due to its desirable band structure. WO_3 is an indirect band gap semiconductor (band gap is ~2.5–2.8 eV) that can capture approximately 12% of the solar spectrum and can absorb light in the visible spectrum up to 500 nm. The band gap of WO_3 is a more suitable for photoelectrochemical water splitting than TiO_2 (band gap is ~3.0–3.2 eV) since TiO_2 absorbs only in the ultraviolet region of the spectrum and captures approximately 4% of solar irradiation. The theoretical maximum conversion efficiency of solar energy into H_2 is merely 2.2% in a photoelectrochemical cell using TiO_2 as a photoanode and is approximately 4.8% using WO_3 as a photoanode. Furthermore, WO_3 exhibits attractive photo stability and chemical

stability in acidic aqueous solutions (pH = 4) under solar illumination. In addition, WO3 has a moderate hole diffusion length (B150 nm) compared with α-Fe_2O_3 (2–4 nm) and TiO_2 (104 nm) and inherently good electron transport properties. In recent years to further increase water oxidation efficiency and photoelectric conversion efficiency, people have made great efforts in adjusting the band gap and femi level by making nanostructures or doping in WO_3.[33-35]

WO3 have also been most extensively studied as electrochromic window due to the outstanding coloration efficiency. Up until now, WO3 films have exhibited the highest coloration efficiency in the visible region of the electromagnetic spectrum. By fabricating EC films from crystalline WO3 nanoparticles, the state-of-the-art technology of producing Electrochromic materials has been largely improved. Nanoparticle films deposited by electrophoresis exhibit vastly superior electrochemical-cycling stability in acidic electrolytes, a higher charge density, and comparable coloration efficiency.

MoO_3, with same perovskite crystal structure as WO_3, is a well-known lithium insertion compound and was investigated from the early years of lithium battery research.[36-66] Sodium-substituted molybdenum oxide was shown to have a high initial capacity of 940 mAh/g when cycled in a voltage window of 3.0–0.005V, but this material suffered from poor cycling stability, with the capacity degrading to 400 mAh/g in 100 cycles. By increasing the cut-off potential to 0.2V and employing a slow rate (discharge and charge at C/15 and C/20, respectively), the cycling was more stable, ranging from

600–400 mAh/g in 100 cycles. More recently, the anodes fabricated from crystalline MoO_3 nanoparticles perform both a durable high rate capability and durable reversible capacity of 630 mAh/g with no capacity degradation for 150 cycles between 3.5 to 0.005V with both charge and discharge at C/2. This result is appealing compared to micrometer-sized particles where the capacity quickly fades.[57,59]

Furthermore, MoO_3 could be also combined with polymers to make composite thermoelectric source. [67] By increasing the interface induced phonon scattering, the thermoconductivity is apparently reduced, which is the most important approach to increase figure of merit in thermoelectrics.
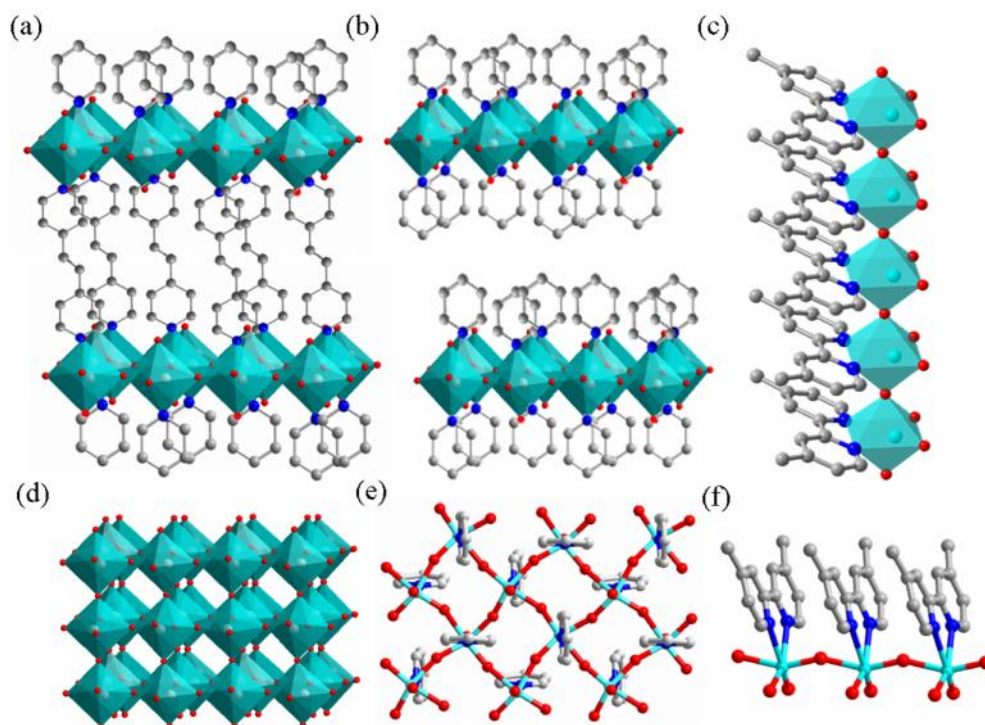
Figure 4: Crystal structures of (a) 3D-WO$_3$(*bpe*)$_{0.5}$, (b) 2D-MoO$_3$(*py*), (c) 1D-WO$_3$ (*4,4′-dimethyl-2,2′bpy*), (d) MoO$_3$ or WO$_3$ perovskite structures. (e) Coordination environment of 2D and 3D hybrid structure viewing from inorganic layer/organic layer stacking axis. (f) Coordination environment of 1D hybrid structure.

Based on above discussion, the perovskite structured WO$_3$ and MoO$_3$ possess a bunch of interesting properties with many potential energy-saving applications. To further increase their properties, we have proposed several solutions.(1) To increase water oxidation efficiency and photoelectric conversion efficiency, we can tune the band gap and femi level by making nanostructures or using organic ligands to confine the electrons transferred in inorganic modules, which will adjust the intensity and range of optical absorption. (2) The applications of MoO$_3$ and WO$_3$ in lithium ion battery and electrochromic window require fast lithium ion intercalation/deintercalation process and the process is strongly dependent on the energy barrier and steric hindrance for Lithium ion transfer. The layered structures with loosely packed atoms and large surface/volume ratio have less energy barrier and steric hindrance, which may show advantage for ion transfer. (3) Composite structure also show promise in reducing thermoconductivity as shown in the case of MoO$_3$/PANI. By increasing the interface induced phonon scattering, the thermoconductivity is apparently reduced and increase figure of merit in thermoelectrics. However, randomly packed MoO$_3$/PANI with no chemical bond

between MoO_3 and polymers suffers from poor conductivity and low thermal stability that prevent it from practical applications.[67] If the MoO_3 and organic molecules can be integrated into single crystal lattice, the ordered structure with continuous inorganic modules may increase the conductivity and thermal stability of hybrid composite while keeping the large interface of MoO_3 for phonon scattering.

Based on facts and considerations stated above, we have designed a novel system of $MO_3(L)$ (L=organic linker) that contain 1D, 2D and 3D periodically ordered nanostructures under mild solvothermal conditions. The results are shown in chapter 2. By inserting different neutral organic linkers inside the parent MO_3 perovskite structure, tunable band structures, chainlike and layered inorganic VI-VI structural motifs, and desired interfaces between inorganic and organic layers can be achieved.

Inspired by the success of II-VI and VI-VI inorganic organic hybrid systems, we have tried further to develop new I-VII inorganic organic hybrid structures and explore their unique properties. The I-VII inorganic structures such as CuI and AgI generally have three different phases: α-phase, β-phase and γ-phase (see Figure 5) and the structural information of I-VII inorganic compounds are listed in Table 1.
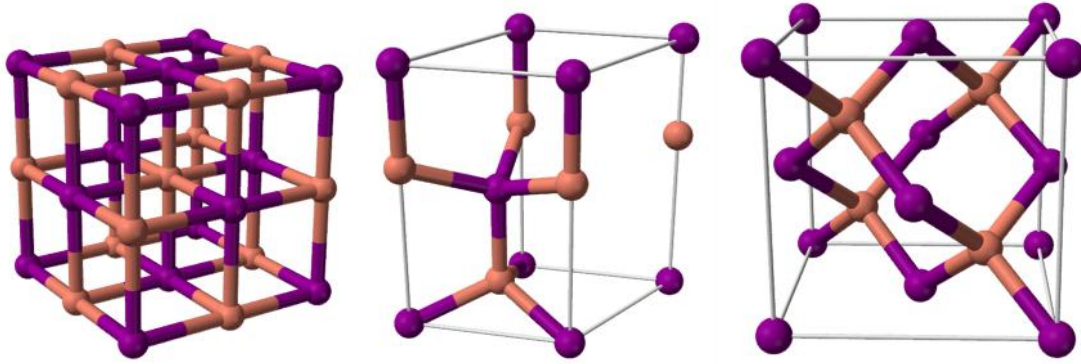
Figure 5: Structures of α-phase (left), β-phase (middle) and γ-phase (right) CuI and AgI.

(Reproduced with permission from wikipedia website.)

Table 1**:** Structural information of I-VII inorganic materials.

Chemicals	Space group	Structure type	Unit cell parameters
α-CuI[1]	Fm-$3m$	RS	a = 6.16866(6) (Å)
β-CuI[2]	P6_3mc	WZ	a = 4.31 (Å) c = 7.09 (Å)
γ-CuI[1]	F-$43m$	ZB	a = 6.05844(3) (Å)
α-CuBr[3]	Fm-$3m$	RS	a = 4.601 (Å)
β-CuBr[2]	P6_3mc	WZ	a = 4.06 (Å) c = 6.66 (Å)
γ-CuBr[5]	F-$43m$	ZB	a = 5.684 (Å)

α-CuCl[6]	Fm-3m	RS	a = 4.9290 (Å)
γ-CuCl[7]	F-$43m$	ZB	a = 5.4202(2) (Å)
α-AgI[8]	Fm-3m	RS	a = 6.495 (Å)
β-AgI[9]	P6$_3mc$	WZ	a = 4.599(3) (Å) c = 7.520(5) (Å)
γ-AgI[4]	F-$43m$	ZB	a = 6.493(5) (Å)
γ-AgBr[10]	F-$43m$	ZB	a = 5.7721(2) (Å)
α-AgCl[10]	Fm-3m	ZB	a = 5.5463(2) (Å)

References for the structural information of these compounds:

1. J. Mater. Chem., 2006, 16, 4393

2. Zeitschrift fuer Naturforschung, Teil A. Physikalische Chemie , 1952, 7, 369

3. Electrochimica Acta, 1977, 22, 701

4. Phase Transition, 1992, 38, 127

5. Comptes Rendus Hebdomadaires des Seances de l'Academie des Sciences, 1955, 241, 69

6. Physical Review, B - Condensed Matter, 1994, 50, 5868

7. Journal of Physics C, 1983, 16, 3673

8. Proceedings of the National Academy of Sciences, U.S.A.1962, 48, 983

9. Solid State Communications, 1977, 24, 411

10. Physical Review, B - Condensed Matter, 1999, 59, 750

The α-phase I-VII compounds have the rock salt structure, in which each ion is surrounded by six ions of the opposite charge as expected on electrostatic grounds. The surrounding ions are located at the vertices of a regular octahedron. The space group is F*m-3m* for α-phase I-VII. The β-phase I-VII compounds crystallize in wurzite structure, which is a member of the hexagonal crystal system and consists of tetrahedrally coordinated cations and anions that are stacked in an ABABAB pattern. The space group of β-phase I-VII compounds is P*6₃mc*. The γ-phase represent zinc blende structure in I-VII compounds which have tetrahedral coordination: each atom's nearest neighbors consist of four atoms of the opposite type, positioned like the four vertices of a regular tetrahedron. It is worth mentioning that the wurzite and zinc blende phases that I-VII compounds have are also observed in II-VI materials such as ZnS, ZnSe and ZnTe, so the basic idea of designing II-VI hybrid structures can be also applied to the design of I-VII hybrid structures. Therefore, the I-VII inorganic organic hybrid structures can be formed when the charge-balanced slices or chains from CuI or AgI are interconnected with neutral organic ligands (e.g. organic diamines). 3D-Cu_3I_3(*1,3,5-triazine*)[68], 2D-AgI(*bpp*)[69], and 1D-Cu_3I_3(*1,3,5-triazine*)[68] compounds represent the 3D, 2D and 1D structures of I-VII hybrid system correspondingly. In addition to wurzite and zinc blende structure, copper iodide can also crystallize in the rock salt structure. It is also possible to select electronically neutral atomic layers or chains from the rock salt CuI structure, while keeping the atomic ratio and bonding type in the selected layers and chains same as its

parent structure.[69-73] When connecting electronically neutral atomic layers and chains with different organic ligands, it is also possible to produce α-CuI based inorganic organic hybrid semiconductors.

(a)　(b)　(c)　(d)

(**f**)
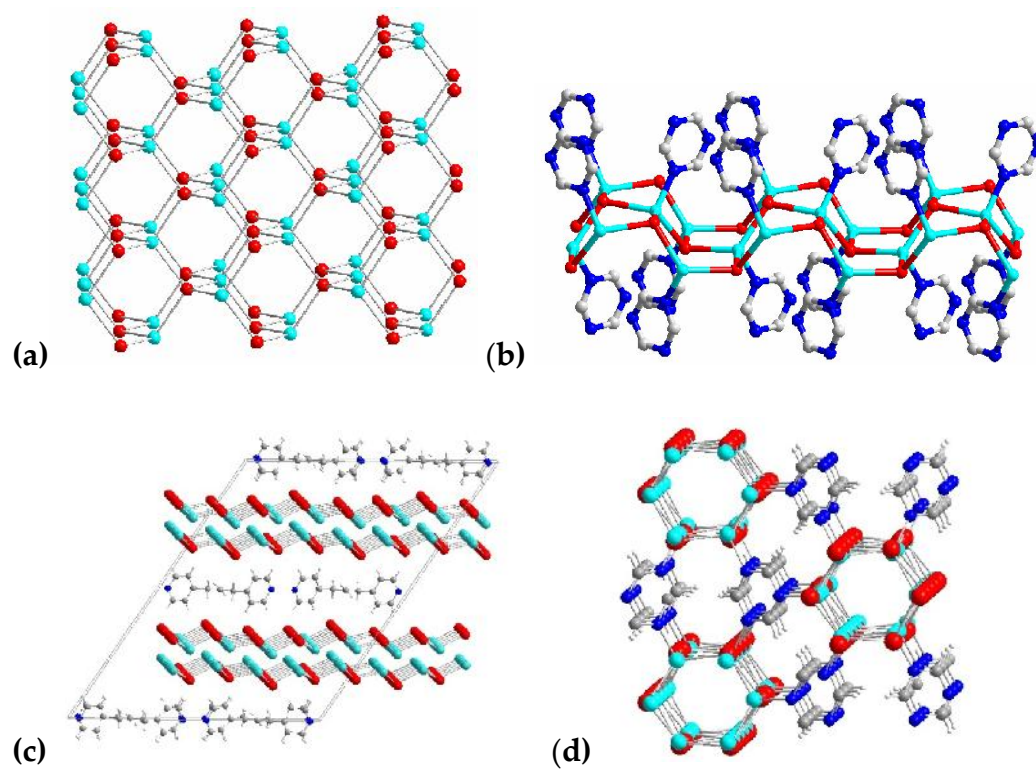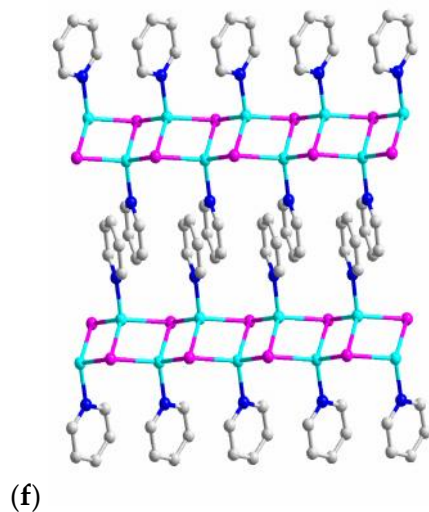
Figure 6: (a) Crystal structure of β-CuI or β-AgI (b) single-layer 3D-[Cu$_2$I$_2$(*1,3,5-triazine*)],

(c) double-layer 2D-[Ag$_6$I$_6$(*bpp*)] and (d) 1D-[Cu$_3$I$_3$(*1,3,5-triazine*)] and (f) 1D-CuI(*pyridine*)

extended network structures of I-VII hybrid materials.

As mentioned earlier in this chapter, the II-VI inorganic organic hybrid structures

generally have strong UV absorption and photoluminescence. Though greatly enhanced,

these properties can be seen as being inherited from their parent ZnS, ZnSe and ZnTe

structures. Therefore, when considering whether I-VII hybrids also have unique optical

properties similar to the II-VI hybrids, it is necessary to figure out how their parent

structures behave optically.

Figure 5 shows the optical absorption properties of I-VII materials. For the

copper halides, the CuI and CuBr display similar band gap value of 2.9 eV and CuI

shows stronger absorption edge. The absorption of CuCl is weak and is difficult to

distinguish the band gap. A similar trend is also observed in silver halides, in which AgI shows much better absorption than AgBr and AgCl. AgI and AgBr have a similar band gap of 2.75 eV. Among all the copper halides and silver halides, only CuI and CuBr exhibit very good photoluminescence between 400nm and 450nm.
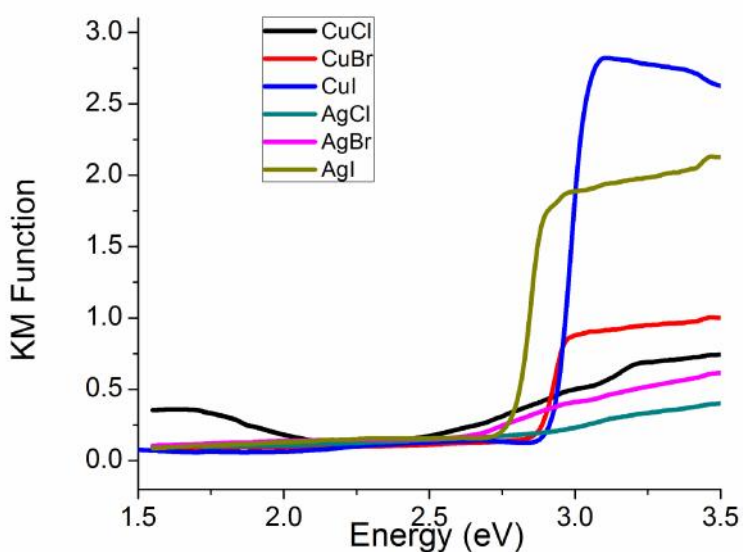
Figure 7: Optical absorption spectrum of I-VII inorganic materials
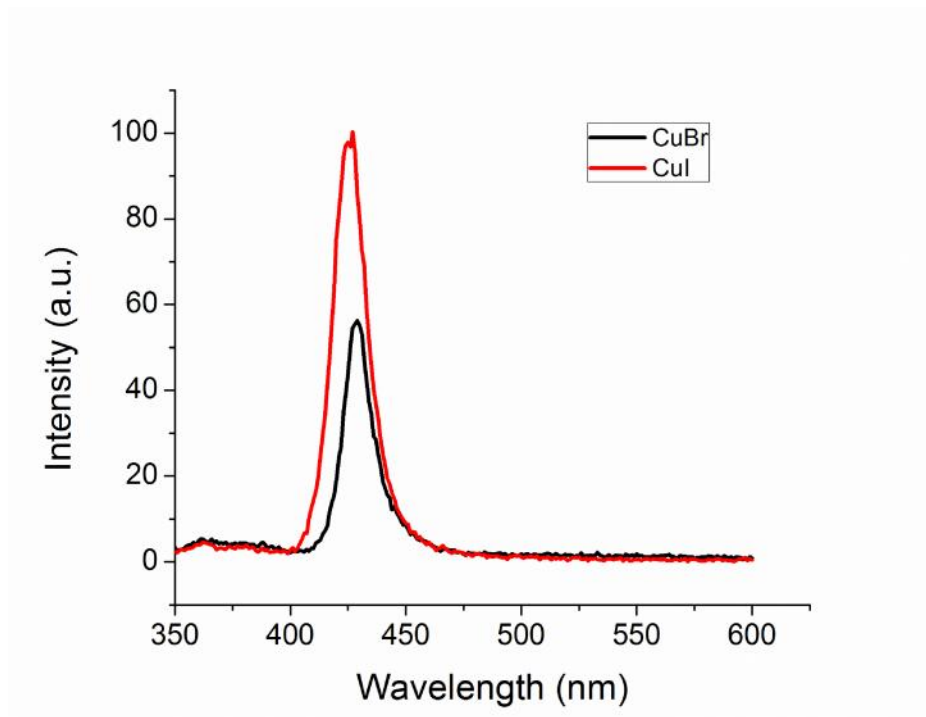
Figure 8: Photoluminescence spectrum of CuI and CuBr.

Based on the comparison of optical behaviors among I-VII parent materials, we have selected CuI as the parent structure to design our inorganic organic hybrid materials on. The strong optical absorption and emission properties of the original parent structure make this an ideal system to modify in the pursuit of interesting optical properties. A series of new CuI(*L*) inorganic organic hybrid structures were prepared with the solution diffusion method. These structures have shown very interesting fluorescence behavior including direct white light emission as did our II-VI hybrid materials. Compared to our II-VI hybrid materials, the fluorescence is even stronger and shows better thermal stability, which gives this material great promise in applications such as light emitting diodes. The results will be summarized in chapter 4.

2. II-VI inorganic organic hybrid semiconductors

2.1 3D-ZnSe(L) (L = alkyl-diamine) structures

2.1.1 3D-ZnSe(*en*)$_{0.5}$ structure

Synthesis of ⌐-[ZnSe(*en*)$_{0.5}$] (1). Pure phase of **1** were obtained by solvothermal

reactions containing 0.273 g of $ZnCl_2$ (2 mmol) and 0.079 g of Se (1 mmol). The starting

materials were mixed and stirred then transferred to a 23 mL acid digestion bomb, and 6

mL of *en* was added. The sample was then heated at 200 °C for 3 days. After being

cooled to room temperature, the mixture was washed with ethanol followed by drying

in anhydrous ethyl ether. The colorless powder of **1** (0.162 g, 90.1% based on Se) was

isolated and kept at room temperature.

The crystal structure of α-[ZnSe(*en*)$_{0.5}$] was solved by powder X-ray diffraction

data at 280K. The 280K PXRD patterns of the powder samples were under helium gas

using an Oxford cryomagnet system at the beamline 11-ID-C, Advanced Photone Source

in Argonne National Laboratory. The ultra-high-energy synchrotron X-rays (with a

wavelength of 0.1077 Å) were used for the PXRD measurements. The refinement began

with fitting background by polynomial interpolation using the same number of points in

each case, followed by refining the zero point of the diffractometer constants. After that,

the unit cell parameters, atomic coordinates of heavy atoms (i.e. Se and Zn), atomic

coordinates of light atoms (e.g., N and C) were refined in sequence. Finally, the Cagliotti

terms of Gaussian width as polynomial in tan θ, (GW, GU, GV) , Lorenzian strain

broadening (LY) and Lorenzian crystallite size (Scherrer) broadening (LX) were added as refinable parameters in sequence and refined with high damping factor to adjust the peak shape. The results of observed and calculated PXRD patterns, as well as difference profile of the *GSAS* Rietveld refinement are shown in Figure 6.
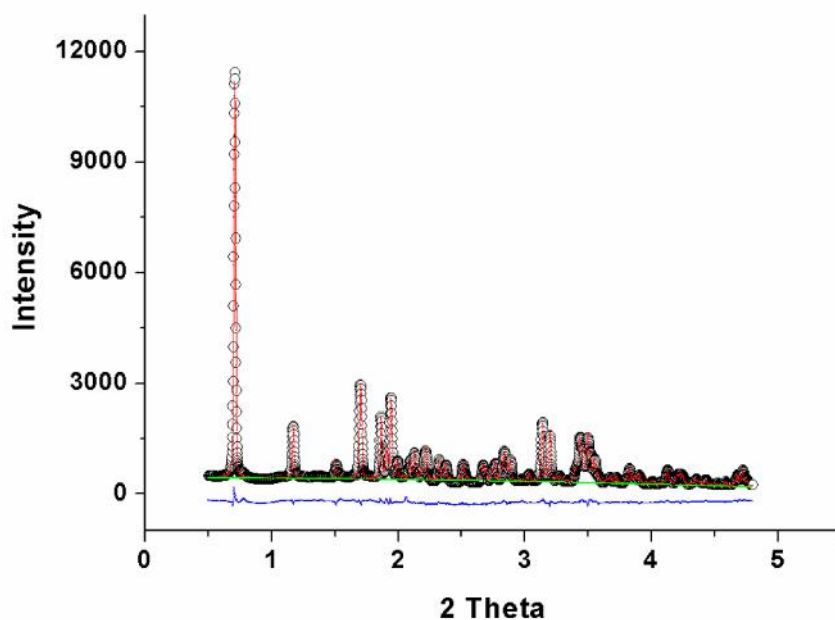
Figure 9: Observed and calculated PXRD patterns, as well as difference profile of the *GSAS* Rietveld refinement of the layered ZnSe(*en*)$_{0.5}$ at 280K. Red line: simulated pattern; Black circles: experimental pattern; Green line: background of simulated pattern; Blue line: difference between the simulated and experimental data. (Reproduced with permission from ref 16. Copyright © 2013 WILEY-VCH Verlag GmbH & Co. KGaA, Weinheim.)

Rietveld analysis based on powder X-ray diffraction data revealed that ZnSe(*en*)$_{0.5}$ compound crystallized in an orthorhombic space group Pbca. There are one zinc atom, one selenium atom and half ethylenediamine molecule in the crystallographic asymmetric unit. Each zinc atom connects to three selenium atoms and a nitrogen atom from ethylenediamine molecule to achieve a stable tetrahedral coordination (Figure 10). The tellurium atoms coordinated to three zinc atoms. The alternating three-coordinated Zn and Se atoms form a puckered 6$_3$ (distorted honeycomb net) [ZnSe] slab along crystallographic ab plane. The slabs are interconnected by ethylenediamine molecules along the c axis through the covalent Zn-N bonds. The Zn-Se bond lengths range from 2.420(4) to 2.460(4) Å (with an average value of 2.443 Å). The Se-Zn-Se bond angles are 115.08/114.22/115.95°, slightly larger than the ideal 109.5° tetrahedral angle.
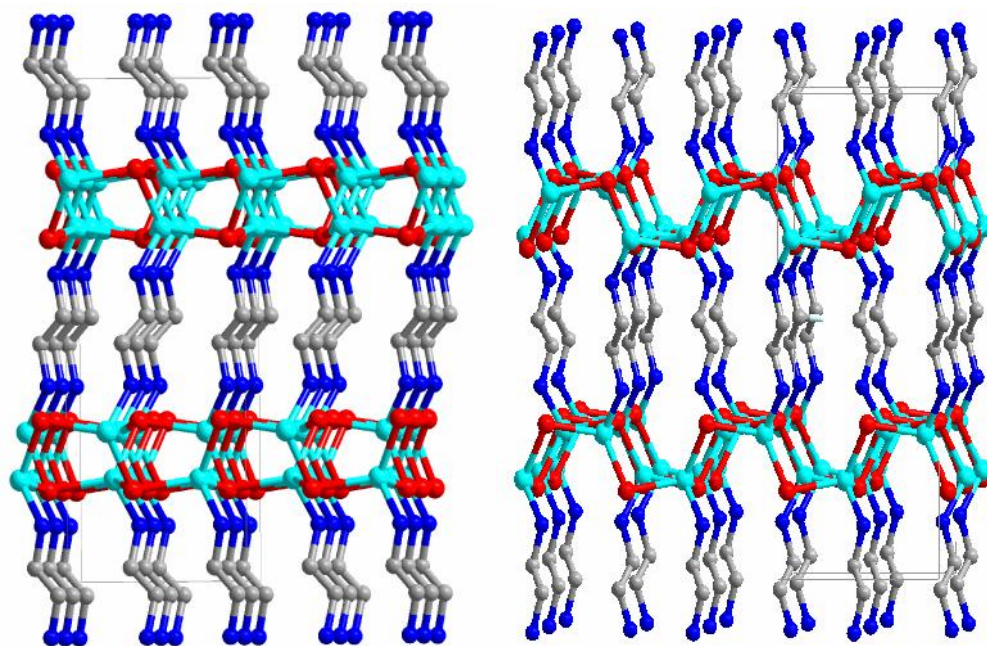
Figure 10: Refined crystal structures of α-[ZnSe(*en*)$_{0.5}$] (**1**) (a) viewing from a-axis and (b) viewing from b-axis The light blue balls are Zn; red balls, Te; blue balls, N; dark grey balls, C; Hydrogen atoms are omitted for clarity.

Optical diffuse reflectance spectra were measured at room temperature using a Shimadzu UV-3101PC double monochromated, double beam spectrophotometer. The absorption edges of ZnSe(*en*)$_{0.5}$ are found to be 4.0 eV, indicating a very large blue shift (1.4-1.6 eV) compared to that of the bulk ZnSe.
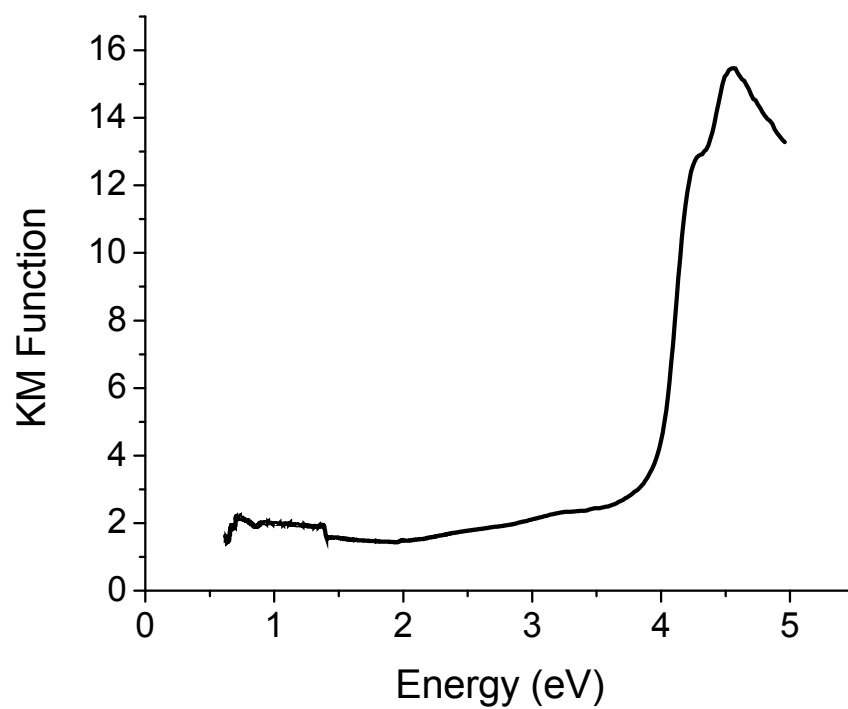
Figure 11: Optical absorption spectra of ZnSe(*en*)$_{0.5}$ inorganic organic hybrid semiconductors.

2.1.2 3D-ZnSe(*pda*)$_{0.5}$ structure

Synthesis of ⌐-[ZnSe(*pda*)$_{0.5}$] (2). Compound **2** was obtained from the reactions of $ZnCl_2$ (0.273 g, 2 mmol), Se (0.079 g, 1 mmol), and *pda* (6 mL) in a molar ratio of 2:1:75 in a 23 mL acid digestion bomb at 200 °C for 3 days. The product was washed by distilled water, ethanol followed by drying in anhydrous ethyl ether. The powders of **2** (0.128 g, 70.0% based on Se) was isolated.

The crystal structure of α-[ZnSe(*pda*)$_{0.5}$] was also solved by powder x-ray diffraction data at 280K. The 280K PXRD data of the powder samples were collected under helium gas using an Oxford cryomagnet system at the beamline 11-ID-C, Advanced Photone Source, Argonne National Laboratory. The high-energy synchrotron X-rays (with a wavelength of 0.1077 Å) were used for the PXRD measurements. The Rietveld method with the same process stated above was also used to refine the crystal structure of ZnSe(*pda*)$_{0.5}$. To make the refinement results comparable with each other, the value of zero point was kept same for each compound and for all temperatures. The Observed and calculated PXRD patterns, as well as difference profile of the *GSAS* Rietveld refinement of ZnSe(*pda*)$_{0.5}$ at 280K was shown below.[74]
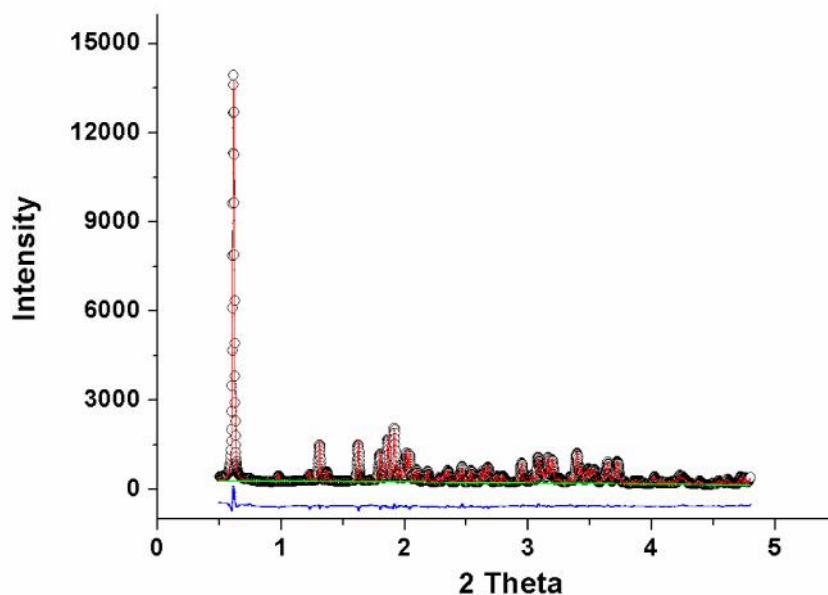
Figure 12: Observed and calculated PXRD patterns, as well as difference profile of the *GSAS* Rietveld refinement of the double layered ZnSe(*pda*)$_{0.5}$ at 280K. Black circles: experimental pattern; Red line: simulated pattern; Green line: background of simulated pattern; Blue line: difference between the experimental and simulated data. (Reproduced with permission from ref 16. Copyright © 2013 WILEY-VCH Verlag GmbH & Co. KGaA, Weinheim.)

Compound 2 crystallized in orthorhombic non-centrosymmetric space group C*mc2*$_1$. There are one zinc atom, one selenium atom and half pda molecule in the crystallographic asymmetric unit. Unlike α-ZnTe(*en*)$_{0.5}$ (**1**), in which an crystallographic inversion center is located in the center of the C-C bond of ethylenediamine molecule, there is a mirror plane passing through the C2 atom of pda in **2**. Consequently, the

adjacent inorganic slabs in **1** are related by an inversion center, while in **2** the adjacent

layers are mirror-symmetric. Although the local coordination of Zn and Te atoms in **2**

and the topology of the slabs are similar to those of **1**, the relative orientation of the slabs

and the connectivity between the slabs and the 1,3-propandiamine molecules are

different. The Zn-Se bond lengths range form 2.383(4) to 2.477(4) Å. The bond angles of

Se-Zn-Se and N-Zn-Se are 112.14/115.48/114.86° and 102.9/97.9/111.5° respectively.
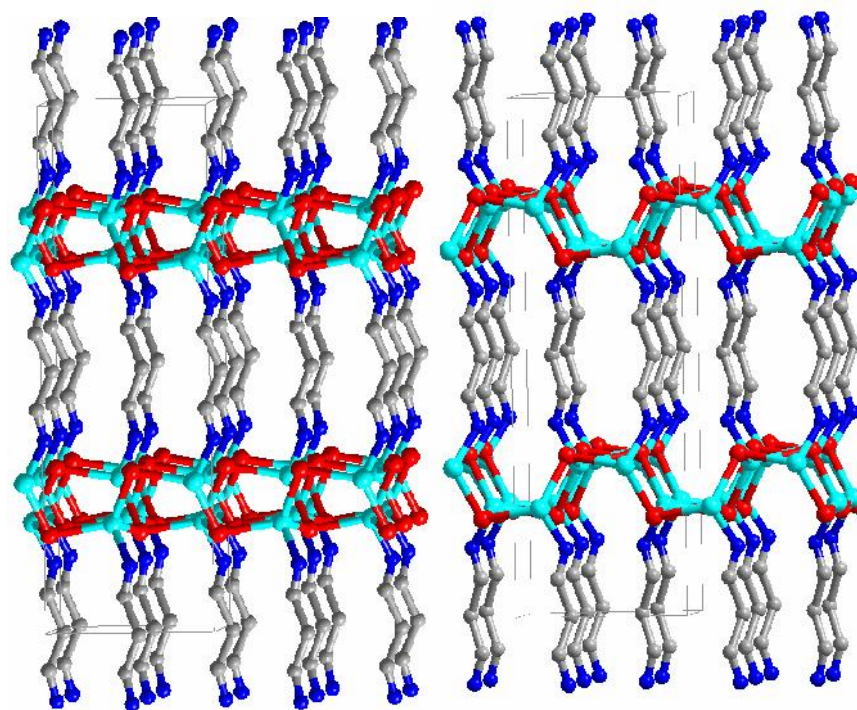
Figure 13: Refined crystal structures of α-[ZnSe(*pda*)$_{0.5}$] (**1**) (a) viewing from b-axis and (b)

viewing from c-axis. The light blue balls are Zn; red balls, Te; blue balls, N; dark grey

balls, C; Hydrogen atoms are omitted for clarity.

Optical diffuse reflectance spectra were measured at room temperature on ZnSe(pda)$_{0.5}$. The absorption edges of ZnSe(pda)$_{0.5}$ are found to be 4.0, similar to ZnSe(en)$_{0.5}$ indicating a very large blue shift (1.4-1.6 eV) compared to that of the bulk ZnSe.
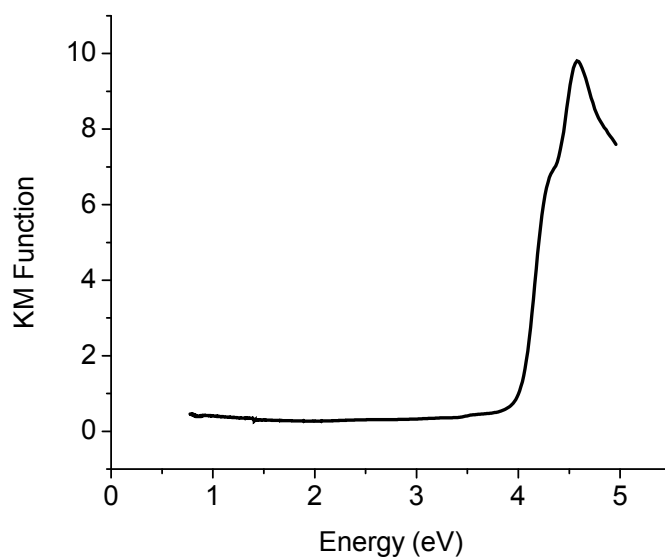
Figure 14: Optical absorption spectra of ZnSe(pda)$_{0.5}$ inorganic organic hybrid semiconductors.

2.1.3 3D-ZnSe(*bda*)$_{0.5}$ structure

Synthesis of ⌐-[ZnSe(*bda*)$_{0.5}$] (3). Compound **3** was prepared from the reactions of Zn(NO$_3$)$_2$ (0.378 g, 2 mmol), Se (0.079 g, 1 mmol), and *bda* (6 mL) in a 23 mL acid digestion bomb. The bomb was sealed and kept at 200 °C for 3 days. The product was washed by water, ethanol and followed by drying in anhydrous ethyl ether. The colorless powder of **3** (0.211 g, 82.7% based on Se) was isolated.

The crystal structure of α-[ZnSe(*bda*)$_{0.5}$] was also solved by powder x-ray diffraction data at 280K that was collected under synchrotron x-ray diffraction in Argonne National Laboratory. The Observed and calculated PXRD patterns, as well as difference profile of the *GSAS* Rietveld refinement of ZnSe(*bda*)$_{0.5}$ at 280K was shown below.
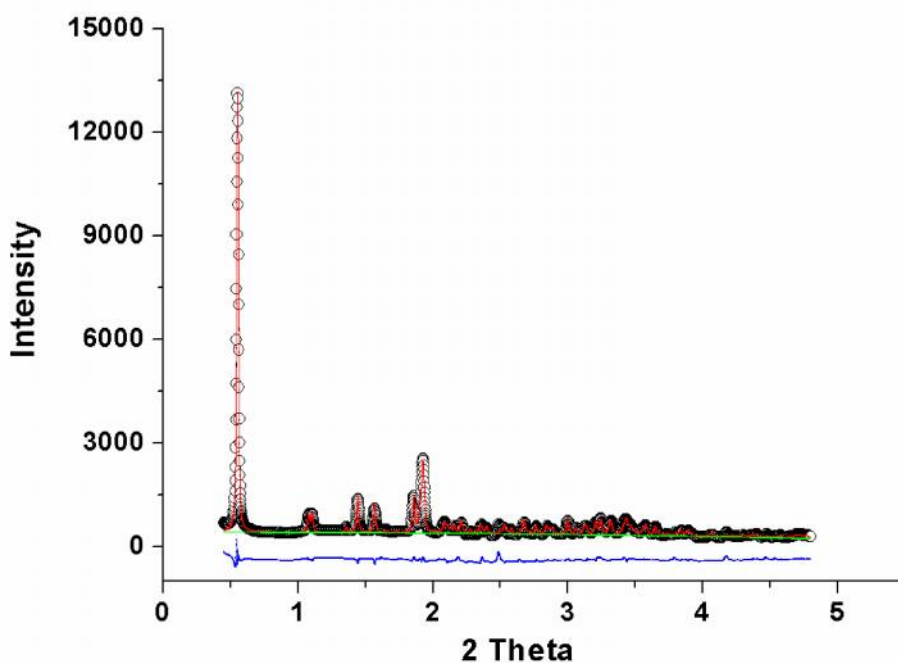
Figure 15: Observed and calculated PXRD patterns, as well as difference profile of the *GSAS* Rietveld refinement of the ZnSe(*bda*)$_{0.5}$ at 280K. Black circles: experimental pattern; Red line: simulated pattern; Green line: background of simulated pattern; Blue line: difference between the experimental and simulated data. (Reproduced with permission from ref 16. Copyright © 2013 WILEY-VCH Verlag GmbH & Co. KGaA, Weinheim.)

Results from Rietveld analysis shows that it crystallizes in an orthorhombic space group P*bca*, same as ZnSe(*bda*)$_{0.5}$ compound. This is reasonable since the relative direction of electron lone pair in nitrogen atoms are same between 1,2-ethylenediamine and 1,4-butanediamine, which results in a similar way of packing of inorganic layers in

the structure. In the crystallographic asymmetric unit, there are also one zinc atom, one selenium atom and half organic molecule. Each zinc atom connects to three selenium atoms and a nitrogen atom from bda molecule to achieve a stable tetrahedral coordination (Figure 16). The slabs are interconnected by bda molecules along the c axis through the covalent (dative) Zn-N bonds. The Zn-Se bond lengths range from 2.402(7) to 2.506(7) Å (with an average value of 2.46 Å). The Se-Zn-Se bond angles are 113.91/115.96/112.00°, slightly larger than the ideal 109.5° tetrahedral angle.
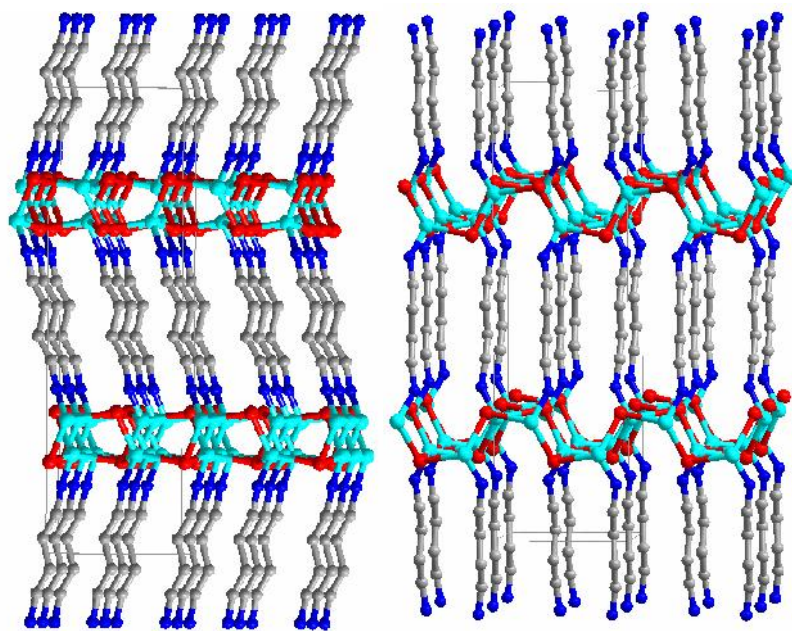
Figure 16: Refined crystal structures of α-[ZnSe(*bda*)$_{0.5}$] (**3**) (a) viewing from a-axis and (b) viewing from b-axis. The light blue balls are Zn; red balls, Te; blue balls, N; dark grey balls, C; Hydrogen atoms are omitted for clarity.

Optical diffuse reflectance spectra were measured at room temperature on ZnSe(*bda*)$_{0.5}$. The absorption edges of ZnSe(*bda*)$_{0.5}$ are found to be 4.0, similar to ZnSe(*en*)$_{0.5}$ and ZnSe(*pda*)$_{0.5}$ indicating a very large blue shift (1.4-1.6 eV) compared to that of the bulk ZnSe.
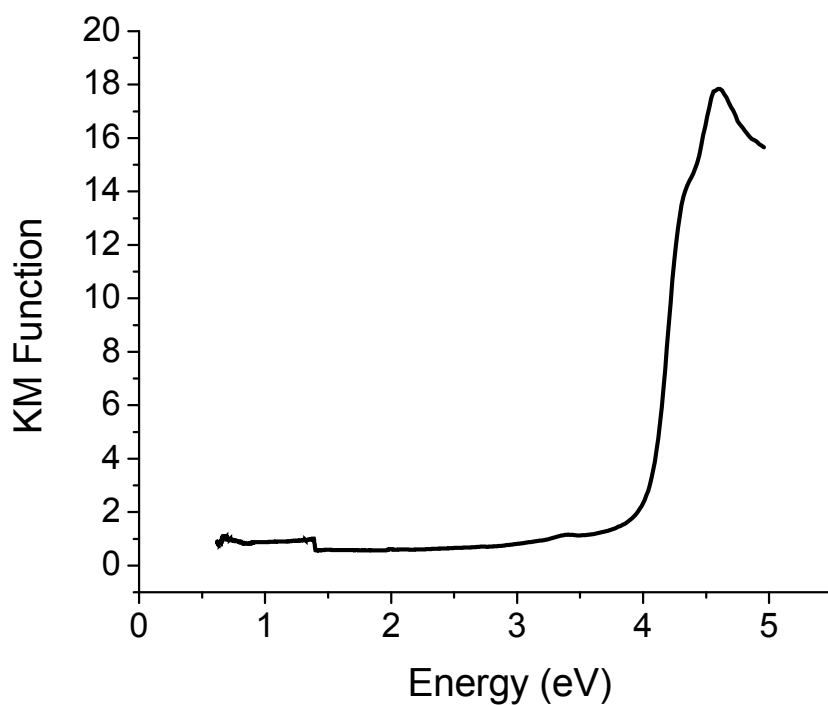
Figure 17: Optical absorption spectra of (a) ZnSe(*bda*)$_{0.5}$ inorganic organic hybrid semiconductors

2.1.4 3D-ZnSe(*ptda*)$_{0.5}$ structure

Synthesis of α-[ZnSe(*ptda*)$_{0.5}$] (4). Reactions of Zn(NO$_3$)$_2$ (0.378 g, 2 mmol), Se (0.079 g, 1 mmol), and *ptda* (6 mL) in a molar ratio of 2:1:75 at 200 °C for 3 days in 23 mL acid digestion bomb afforded light yellow powders of **4** (0.227 g, 84.0% yield based on Se). The same experimental procedure used for the synthesis of **1, 2** and **3** was applied here.

The crystal structure of α-[ZnSe(*ptda*)$_{0.5}$] was also solved by powder x-ray diffraction data at 280K and Rietveld refinement was used to get the unit cell, space group and atomic positions of the compound as for other compounds. The results are shown below.
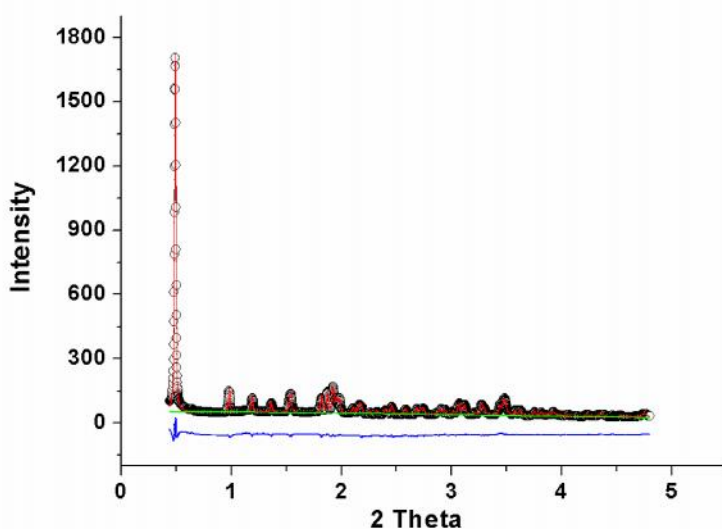
Figure 18: Observed and calculated PXRD patterns, as well as difference profile of the *GSAS* Rietveld refinement of the ZnSe(*ptda*)$_{0.5}$ at 280K. Black circles: experimental

pattern; Red line: simulated pattern; Green line: background of simulated pattern; Blue line: difference between the experimental and simulated data. (Reproduced with permission from ref 16. Copyright © 2013 WILEY-VCH Verlag GmbH & Co. KGaA, Weinheim.)

The results from Rietveld analysis reveals that it crystallizes in an noncentrosymmetric space group $Cmc2_1$, same as ZnSe(pda)$_{0.5}$ compound. This is reasonable because the relative direction of electron lone pair in nitrogen atoms are same between 1,3-propanediamine and 1,5-pentanediamine, which results in a similar way of packing of inorganic layers in the structure. There are one zinc atom, one selenium atom and half ptda molecule in the crystallographic asymmetric unit. The Zn-Se bond lengths range from 2.434(9) to 2.459(8) Å (with an average value of 2.436 Å). The Se-Zn-Se bond angles are 113.62/114.71/113.64^o, slightly larger than the ideal 109.5^o tetrahedral angle, while the N-Zn-N bond angles (101.0/ 100.9/111.3^o) are slightly compressed.
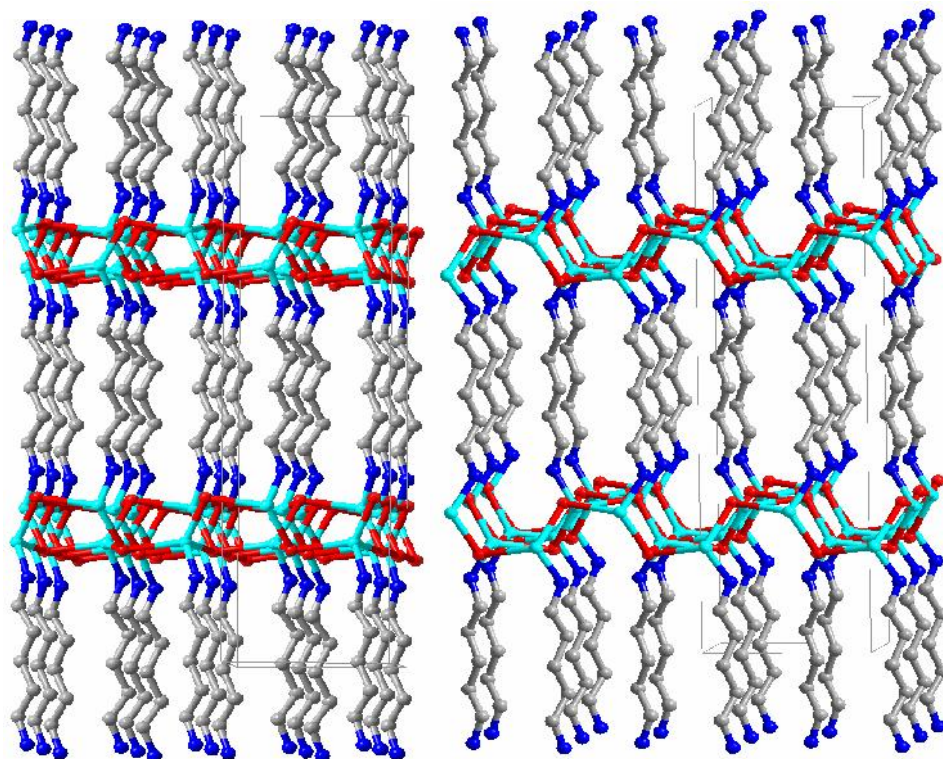
Figure 19: Refined crystal structures of α-[ZnSe(*ptda*)0.5] (**1**) (a) viewing from b-axis and (b) viewing from c-axis. The light blue balls are Zn; red balls, Te; blue balls, N; dark grey balls, C; Hydrogen atoms are omitted for clarity.

Optical diffuse reflectance spectra were measured at room temperature on ZnSe(*ptda*)0.5. The absorption edges of ZnSe(*ptda*)0.5 are found to be 4.0 eV, similar to other three compounds, indicating a very large blue shift (1.4-1.6 eV) compared to that of the bulk ZnSe.
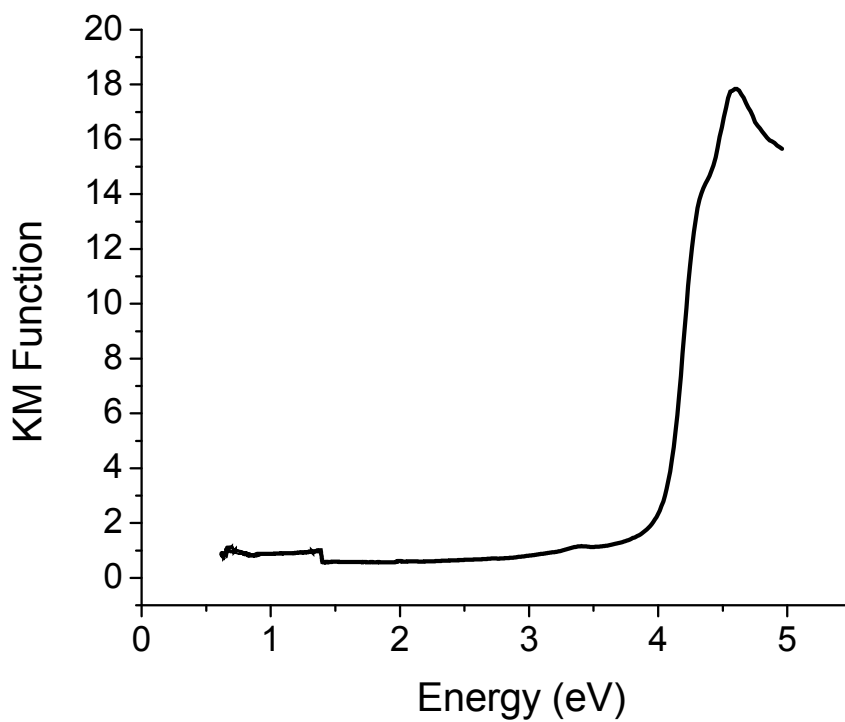
Figure 20: Optical absorption spectra of ZnSe(*ptda*)$_{0.5}$ inorganic organic hybrid semiconductors.

2.1.5 Summary of Γ-ZnSe(*L*)$_{0.5}$ inorganic organic hybrid structures

The Rietveld refinement results show that compounds containing organic diamines with an even number of carbons (*n*), namely **1** (*n* = 2) and **3** (*n* = 4) crystallize in centrosymmetric space group *Pbca* (No. 61), and those with organic diamines of an odd number of carbons, **2** (*n* = 3) and **4** (*n* = 5), crystallize in noncentrosymmetric space group *Cmc2$_1$* (No. 36). The unit cell parameters of all four structures were refined using full X-ray diffraction data sets collected at 280 K (see Table 1). The lattice parameters of the four structures are: α-Zn$_2$Se$_2$(*en*) (**1**), *a* = 6.6382(3)Å, *b* = 6.4702(2) Å, *c* = 17.3822(6) Å; α-

$Zn_2Se_2(pda)$ (**2**), a = 20.0192(7) Å, b = 6.6389(3) Å, c = 6.4531(2) Å; α-$Zn_2Se_2(bda)$ (**3**), a = 6.6388(5) Å, b = 6.4662(5) Å, c = 22.3042(13) Å; α-$Zn_2Se_2(ptda)$ (**4**), a = 25.1159(16) Å, b = 6.6218(6) Å, c = 6.4436(5) Å. As the number of carbon atoms increases, the length of the long axis (L_3) increases by about 2.5 Å per carbon atom, while the length of other two short axes (L_1 and L_2) remains approximately the same.

Table 2: Crystal structure data of α-ZnSe(*en*)$_{0.5}$ (1)，α- ZnSe(*pda*)$_{0.5}$ (2)，α-ZnSe(*bda*)$_{0.5}$ (3)，and α-ZnSe(*ptda*)$_{0.5}$ (4) by Rietveld refinement. (Reproduced with permission from ref 16. Copyright © 2013 WILEY-VCH Verlag GmbH & Co. KGaA, Weinheim.)

Empirical Formula	ZnSe (*en*)$_{0.5}$	ZnSe(*pda*)$_{0.5}$	ZnSe(*bda*)$_{0.5}$	ZnSe(*ptda*)$_{0.5}$
*F*w	348.83	362.83	376.85	390.98
Space Group	*Pbca*	*Cmc2$_1$*	*Pbca*	*Cmc2$_1$*
a (Å)	6.6382(3) (L$_1$)	20.0192(7) (L$_3$)	6.6388(5) (L$_1$)	25.1159(16) (L$_3$)
b (Å)	6.4702(2) (L$_2$)	6.6389(3) (L$_1$)	6.4662(5) (L$_2$)	6.6218(6) (L$_1$)
c (Å)	17.3822(6) (L$_3$)	6.4531(2) (L$_2$)	22.3042(13) (L$_3$)	6.4436(5) (L$_2$)
V (Å^3)	746.58(5)	857.65(6)	957.48(12)	1071.65(14)
Z	8	8	8	8
T (K)	280	280	280	280
λ (Å)	0.107716	0.107716	0.107716	0.107716
ρ (g·cm^{-3})	3.103	2.810	2.61	2.42
2θ range	0.45-4.8	0.45-4.8	0.45-4.8	0.45-4.8

(°)				
Step size (2θ, °)	0.0015	0.0015	0.0015	0.0015
Step scan time (s)	8	8	8	8
Rwp	0.0600	0.0616	0.0684	0.0736
Rp	0.0410	0.0442	0.0503	0.0542

The atomic coordinates and equivalent isotropic temperature factors and structural refinement information of **1**, **2**, **3** and **4** at 280K were shown in the following Table 2 and the selected bond lengths (Å) and angles (deg) of the structures **1**, **2**, **3** and **4** are shown in Table 3, 4, 5 and 6, respectively.

Table 3**:** Atomic Coordinates and Equivalent Isotropic Temperature Factors (Å^2) for **1**, **2**, **3** and **4** at 280K. Hydrogen atoms are omitted. (Reproduced with permission from ref 16. Copyright © 2013 WILEY-VCH Verlag GmbH & Co. KGaA, Weinheim.)

atoms	x	y	z	U_{eq}
	1			
Zn	0.1009(4)	0.1494(5)	0.2976(2)	0.0219(7)
Se	0.4452(4)	0.0212(4)	0.3189(1)	0.0144(5)

N	-0.0373(21)	0.0213(25)	0.3925(7)	0.0290(6)
C1	0.0408(30)	0.0640(30)	0.4691(10)	0.0290(10)

2

Zn1	0.2100(2)	0.1573(4)	0.0525(5)	0.0301(8)
Se	0.1901(1)	0.1904(3)	0.4277(5)	0.0147(5)
N	0.1218(6)	0.2970(23)	-0.0819(30)	0.0151(1)
C1	0.0563(8)	0.2325(29)	-0.0131(1)	0.0131(1)
C2	0.0000(0)	0.3030(4)	-0.1020(1)	0.0201(1)

3

Zn	-0.0915(8)	0.3043(8)	0.28767(23)	0.0450(15)
Se	-0.0583(6)	-0.0616(7)	0.30346(17)	0.0246(9)
N	0.0441(4)	0.4251(5)	0.3613(8)	0.0221(0)
C1	-0.0290(4)	0.3910(7)	0.4211(10)	0.0342(2)
C2	0.0441(6)	0.519(7)	0.4729(12)	0.0401(2)

4

Zn	0.2168(2)	0.1547(9)	0.2309(9)	0.0463(16)
Se	0.2026(5)	0.1909(7)	0.6028(10)	0.0232(10)
N	0.1506(8)	0.297(4)	0.1171(5)	0.0241(2)
C1	0.0996(11)	0.2331(1)	0.1811(7)	0.0412(2)
C2	0.0516(11)	0.3221(1)	0.0821(1)	0.036(18)

Table 4: Structural refinement information of ZnSe(en)$_{0.5}$ (**1**) (Reproduced with permission from ref 16. Copyright © 2013 WILEY-VCH Verlag GmbH & Co. KGaA, Weinheim.)

Selected bond lengths (Å) and angles (deg) with esd. in parentheses for compound **1**.

Bond				lengths
Zn1-Se1	2.460(4)		Zn1-N1	2.062(13)
Zn1-Se2	2.453(4)	N1-C1	1.456(22)	
Zn1-Se3	2.420(4)	C1-C1	1.463(4)	
Bond angles				
Se1-Zn1-Se2	115.08(1)		Zn1-Se3-Zn2	98.91(1)
Se2-Zn1-Se3	114.08(1)		Zn1-Se3-Zn3	105.22(0)
Se3-Zn1-Se1	114.19(0)		Zn2-Se3-Zn3	101.07(8)
Se1-Zn1-N1	102.53(0)		Zn-N1-C1	119.92(1)
Se2-Zn1-N1	99.05(1)		N1-C1-C1	115.71(2)
Se3-Zn1-N1	119.97(0)			

Table 5: Structural refinement information of ZnSe(pda)$_{0.5}$ (**2**) (Reproduced with permission from ref 16. Copyright © 2013 WILEY-VCH Verlag GmbH & Co. KGaA, Weinheim.)

Selected bond lengths(Å) and angles (deg) with esd. in parentheses for compound **2**:

Bond				lengths
	Zn1-Se3	2.463(5)	Zn1-N1	2.174(14)
Zn1-Se1	2.477(4)	N1-C1	1.451(22)	
Zn1-Se2	2.383(4)	C1-C2	1.348(25)	
Bond angles				
Se1-Zn1-Se3	112.14(15)	Zn1-Se3-Zn2	102.17(13)	
Se2-Zn1-Se3	115.48(15)	Zn1-Se3-Zn3	103.57(13)	
Se1-Zn1-Se2	114.86(16)	Zn2-Se3-Zn3	98.67(13)	
Se3-Zn1-N1	102.90(5)	Zn1-N1-C1	119.02(2)	
Se1-Zn1-N1	97.91(4)	N1-C1-C2	121.51(3)	
Se2-Zn1-N1	111.50(4)	C1-C2-C1	113.32(4)	

Table 6: Structural refinement information of ZnSe(*bda*)$_{0.5}$ (**3**) (Reproduced with permission from ref 16. Copyright © 2013 WILEY-VCH Verlag GmbH & Co. KGaA, Weinheim.)

Selected bond lengths (Å) and angles (deg) with esd. in parentheses for compound **3**:

Bond lengths			
Zn1-Se3	2.402(7)	Zn1-N1	2.029(22)
Zn1-Se1	2.506(7)	N1-C1	1.437(31)

Zn1-Se2	2.423(7)			C1-C2	1.503(5)

C2-C2   1.371(6)

Bond angles

Se1-Zn1-Se3	113.91(25)		Zn1-Se3-Zn2	103.59(21)
Se2-Zn1-Se3	115.96(25)		Zn1-Se3-Zn3	105.50(1)
Se1-Zn1-Se2	112.00(25)		Zn2-Se3-Zn3	98.00(1)
Se3-Zn1-N1	102.62(8)		Zn1-N1-C1	122.91(21)
Se1-Zn1-N1	99.61(7)		N1-C1-C2	121.41(31)
Se2-Zn1-N1	110.94(9)		C1-C2-C2	116.00(20)

Table 7: Structural refinement information of ZnSe(*ptda*)$_{0.5}$ (**4**) (Reproduced with permission from ref 16. Copyright © 2013 WILEY-VCH Verlag GmbH & Co. KGaA, Weinheim.)

Selected bond lengths(Å) and angles (deg) with esd. in parentheses for compound **4**:

Bond					lengths
	Zn1Se3	2.434(9)		N1-C1	1.412(4)
Zn1-Se1	2.459(8)		C1-C2	1.481(5)	
Zn1-Se2	2.415(8)		C2-C3	1.502(4)	
Zn1-N1	2.054(25)				

Bond angles

Se2-Zn1-Se3	113.62(29)	Zn1-Se3-Zn2	102.57(25)
Se2-Zn1-Se3	114.71(29)	Zn1-Se3-Zn3	104.78(24)
Se1-Zn1-Se2	113.67(30)	Zn2-Se3-Zn3	99.06(24)
Se3-Zn1-N1	100.91(10)	Zn1-N1-C1	119.61(25)
Se1-Zn1-N1	101.02(9)	N1-C1-C2	119.62(35)
Se2-Zn1-N1	111.31(8)	C1-C2-C3	114.02(4)
C2-C3-C2	119.02(30)		

2.2 Thermal expansion behavior of ZnSe(L) hybrid structures

2.2.1 Significance of thermal expansion behavior study

Most materials in nature expand on heating, a phenomenon referred to as positive thermal expansion (PTE). The opposite behavior occurs less commonly, when materials shrink upon heating, and is called negative thermal expansion (NTE).[75,76] Several possible mechanisms may be associated with the negative thermal expansion found in oxide phases. First of all, the metal oxygen polyhedron becomes less distorted with increasing temperature and the higher regularity can lead to shorter bond length and lead to negative thermal expansion. For example, the distorted TiO_6 octahedron in $BaTiO_3$[77] and $PbTiO_3$[78] become more regular upon heating which leads to NTE in a certain temperature range. Secondly, the distribution of interstitial cations in some open structures such as β-eucryptite[79], named after a mineral $LiAlSiO_4$, may vary over available sites with changing temperature. In such a case, the increase in the Li-O bond length drives the thermal expansion in two dimensions while the rigidity of the Al-O and Si-O bonds forces the contraction in the third dimension. Thirdly, rotation of a metal oxygen polyhedra can also trigger anisotropic NTE. This mechanism was first found in cordierite $Mg_2Al_2Si_5O_{18}$[13], where the increase of the Mg-O bond length within the two dimensional slab causes the expansion of the slab as temperature rises. However, the lengths of the Si-O or Al-O bonds between the slabs are not affected, and the changes in the bond angles of the SiO_4 or AlO_4 tetrahedron rotate the polyhedron in such a way that

pulls the slabs closer together, resulting in negative thermal expansion in the direction perpendicular to the slabs. In addition to the NTE mechanisms mentioned above, the transverse thermal motion (TTM) is also a well-accepted and common mechanism for NTE[80,81]. In such a case, NTE originates from the transverse thermal vibration of bridging cyanide or oxide ions which draw their connected metal centers closer together (i.e. AM_2O_8[82,83], AM_2O_7[84], $A_2M_3O_{12}$[85], zeolite[86], $M(CN)_2$[87], ReO_3[88,89] families and Prussian blue analogues[90-92]), resulting in the observed contraction of the lattice parameter as a function of increasing temperature.

One of the important applications of NTE compounds is their use in fabrication of composite materials having an overall zero thermal expansion (ZTE). With a constant volume, the ZTE composite neither expand nor contract as temperature changes. These materials are highly desirable because they are free of thermal shock on rapid temperature change, and can prevent structural instability and mechanical degradation caused by the fragility of ceramics towards sizable and volumetric changes as temperature varies[93,94]. A common approach to achieve an overall zero thermal expansion is to blend a PTE and a NTE material. However, this method remains to be a major technical challenge due to the incompatibility of the two very different phases.[95] Furthermore, in such ZTE composites, the PTE ingredient often shows quite different thermal behavior from that of the NTE ingredient as temperature varies. Hence, the stress induced at interfaces may give rise to microcracks, which degrade the mechanical

performance and sometimes physical properties.[96] Such a microcracking problem may be avoided if zero thermal expansion can be achieved in a single crystalline material. The structures with such properties are also rare. Most of them reported till present are insulating oxides which have found use in heat-engine components, optics and kitchenwares, but are not suitable for applications in optoelectronics and electronics. Very few known examples of non-oxide ZTE materials that exhibit semiconductive or conductive properties include metallic Invar Fe-Ni alloys ($Fe_{36}Ni$)[95], $Mn_3Cu_{1-x}Si_xGe_xN$[96] and $YbGaGe$[97].

Crystalline inorganic organic hybrid semiconductors are a new type of functional materials that incorporate semiconductor modules in nanoscale and organic molecules in a single crystal lattice.[15,98-105] Study on a prototype β-3D-ZnTe(en)$_{0.5}$ structure revealed that both ZnTe and ethylenediamine molecule show typical PTE, however their hybrid structure exhibits nearly zero thermal expansion along the layer stacking axis.[104] Specifically, the inorganic component (ZnTe slab) remains to be PTE but the organic diamine shows strong NTE in the hybrid structure. This study suggests that hybrid structures may have the following advantages as possible candidates for ZTE materials: (a) ZTE may be achieved by the two opposing effect (NTE and PTE) within a single crystal lattice to avoid grain boundary associated cracks, and (b) Both PTE and NTE can be systematically and independently tuned by varying the inorganic layers and organic molecules.

Based on these considerations, we have carried out a systematic study of the thermal expansion behavior on a series of 3D-α-ZnSe(*L*)$_{0.5}$ type compounds, an analogue of the 3D-β-ZnTe(*en*)$_{0.5}$ and 3D-α-ZnTe(*L*)$_{0.5}$ hybrid structures.[15] We report the synthesis and structure refinement of α-[ZnSe(*en*)$_{0.5}$] (**1**), α-[ZnSe(*pda*)$_{0.5}$] (**2**), α-[ZnSe(*bda*)$_{0.5}$] (**3**), and α-[ZnSe(*ptda*)$_{0.5}$] (**4**) (where α- and β-phase have very similar structures, with only small differences in the bond distances and angles in the inorganic layer).

2.2.2 Thermal expansion results and analysis.

In order to study the thermal expansion behavior of α-ZnSe(*L*)$_{0.5}$, the PXRD patterns of the powder samples were collected between 5K and 300K at an interval of 10 K under helium gas using an Oxford cryomagnet system at the beamline 11-ID-C, Advanced Photone Source, Argonne National Laboratory. The high-energy synchrotron X-rays (with a wavelength of 0.1077 Å) were used for the PXRD measurements. The

structure was acquired at each temperature by Rietveld refinements. Since the α-ZnSe(*L*)0.5 inorganic organic compounds are isostructural to the α-ZnTe(*L*)0.5 structures, the input cell parameters and atomic coordinates of α-ZnSe(*L*)0.5 were taken from those of α-ZnTe(*L*)0.5 and thermal parameters were assumed to be isotropic. The refinement procedure is the same as in previous discussion.
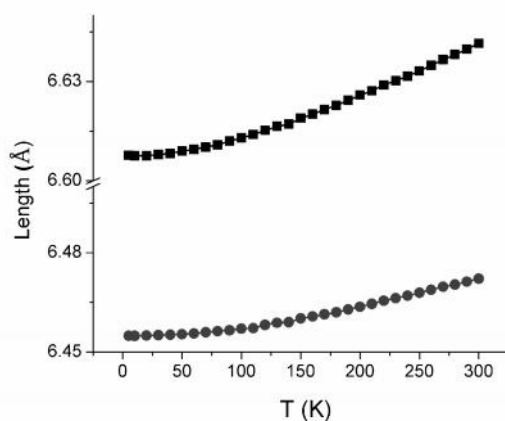
Figure 21: The temperature dependent lattice constants in L₁ (■) and L₂ (●) for ZnSe(*en*)0.5 (**1**). (Reproduced with permission from ref 16. Copyright © 2013 WILEY-VCH Verlag GmbH & Co. KGaA, Weinheim.)
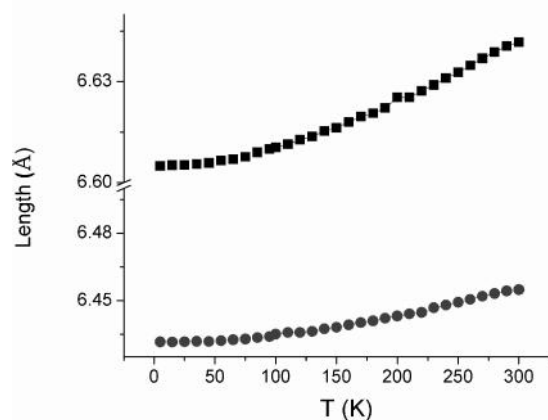
Figure 22: The temperature dependent lattice constants in L₁ (■) and L₂ (●) for ZnSe(*pda*)₀.₅ (**2**). (Reproduced with permission from ref 16. Copyright © 2013 WILEY-VCH Verlag GmbH & Co. KGaA, Weinheim.)
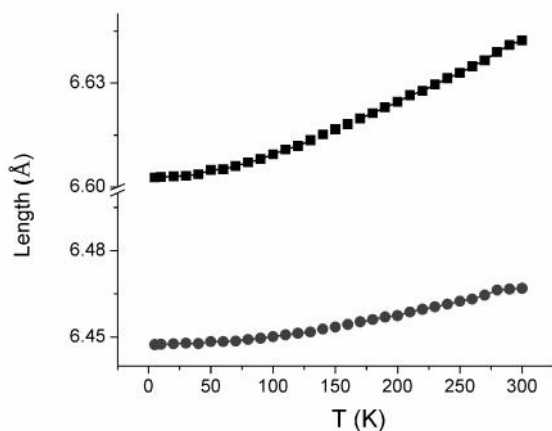
Figure 23: The temperature dependent lattice constants in L₁ (■) and L₂ (●) for ZnSe(*bda*)₀.₅. (Reproduced with permission from ref 16. Copyright © 2013 WILEY-VCH Verlag GmbH & Co. KGaA, Weinheim.)
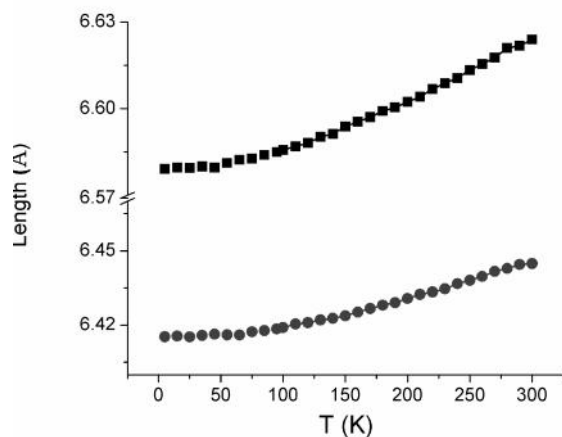
Figure 24: The temperature dependent lattice constants in L_1 (■) and L_2 (●) for ZnSe($ptda$)$_{0.5}$ (**4**). (Reproduced with permission from ref 16. Copyright © 2013 WILEY-VCH Verlag GmbH & Co. KGaA, Weinheim.)

Plotted in Figure 14 to Figure 17 are the lattice constants of the ZnSe(L)$_{0.5}$ compounds as a function of temperature. For those belonging to the space group *Pbca* (No. 61), **1** and **3**, the extent of thermal expansion (TE) is in the order of $a > b > c$. For compounds **2** and **4** which crystallize in space group *Cmc2$_1$* (No. 36), the order is $b > c > a$. The other two axes are characteristic of PTE, with the longer axis (L_1) demonstrating higher TE coefficient than the shorter axis (L_2). Therefore, For all ZnSe(L)$_{0.5}$ compounds, the extent of TE is in the order of $L_3 < L_2 < L_1$.
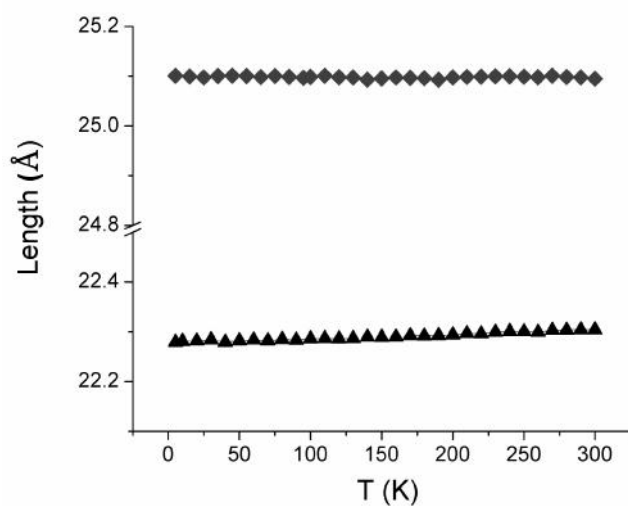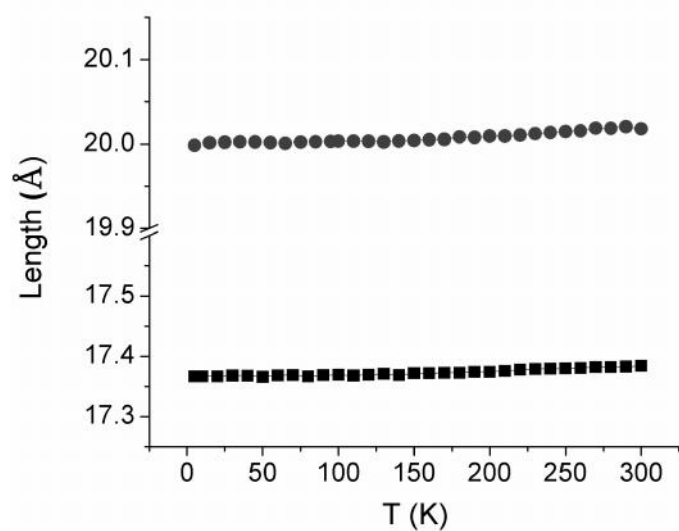
Figure 25: The temperature dependent lattice constants in L$_3$ for (up) ZnSe(*en*)$_{0.5}$ (**1**) (■) and ZnSe(*pda*)$_{0.5}$ (**2**) (●); (down) ZnSe(*bda*)$_{0.5}$ (**3**) (▲) and ZnSe(*ptda*)$_{0.5}$ (**4**) (◆).(Reproduced with permission from ref 16. Copyright © 2013 WILEY-VCH Verlag GmbH & Co. KGaA, Weinheim.)

Using lattice parameters obtained at different temperatures, the linear thermal expansion coefficients (α_L or simply α) can be calculated with formula :

$$\alpha_L = \frac{1}{L}\frac{dL}{dT}$$

where L is the lattice constant and dL/dT is the rate of change of lattice constant per unit change in temperature. The calculated thermal expansion coefficients for all four compounds are included in Table 8.

Table 8: Linear thermal expansion coefficients (α) of **1** - **4**. (Reproduced with permission from ref 16. Copyright © 2013 WILEY-VCH Verlag GmbH & Co. KGaA, Weinheim.)

Compound	$\alpha \times 10^6/K^{-1}$ (L_3)	$\alpha \times 10^6/K^{-1}$ (L_1)	$\alpha \times 10^6/K^{-1}$ (L_2)
ZnSe(en)$_{0.5}$ (**1**)	3.39	17.4	9.04
ZnSe(bda)$_{0.5}$ (**3**)	3.56	20.5	10.1
ZnSe(pda)$_{0.5}$ (**2**)	3.32	18.9	12.2
ZnSe($ptda$)$_{0.5}$ (**4**)	-0.78	23.1	15.6

To compare the relative expansion behaviors of different axis over the whole temperature range, the normalized lattice constants, a, b and c are calculated by dividing the change in length during the thermal expansion by the length at 5K ($\delta L/L_0$) for the four compounds and the results are plotted in Figure 26 to Figure 29. For all four

compounds, the long axis (L$_3$) displays the least thermal expansion with their TE

coefficients less than 5×10^{-6}/K (See Table 8), indicating nearly ZTE in this direction.
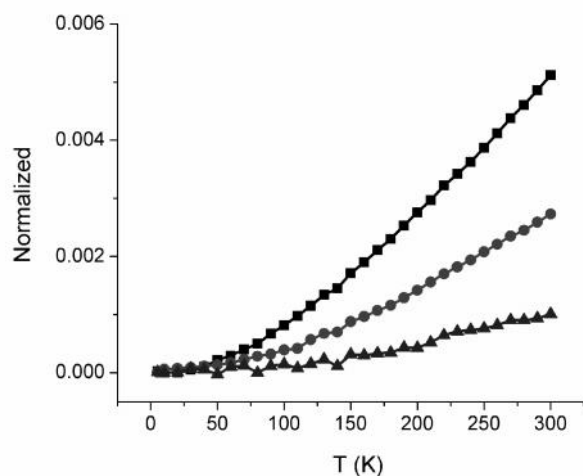
Figure 26: The normallized lattice constants L$_1$ (■), L$_2$ (●) and L$_3$ (▲) for α-ZnSe(*en*)$_{0.5}$ (**1**)

at different temperatures. (Reproduced with permission from ref 16. Copyright © 2013

WILEY-VCH Verlag GmbH & Co. KGaA, Weinheim.)
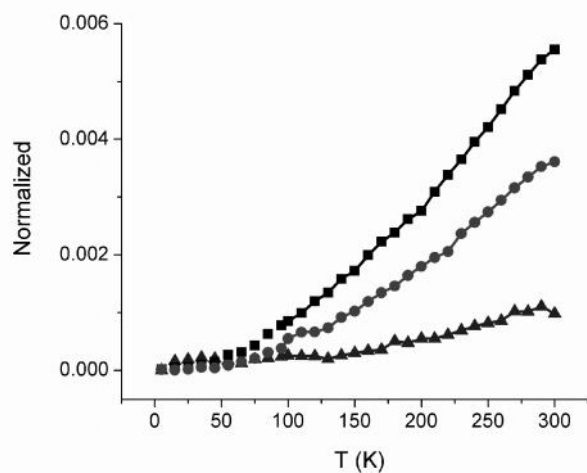
Figure 27: The normallized lattice constants L₁(■), L₂(●) and L₃(▲) for α-ZnSe(*pda*)₀.₅

(**2**), at different temperatures. (Reproduced with permission from ref 16. Copyright ©

2013 WILEY-VCH Verlag GmbH & Co. KGaA, Weinheim.)
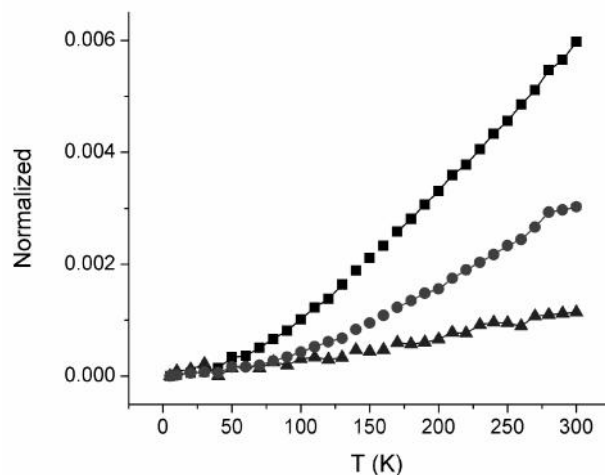
Figure 28: The normallized lattice constants L₁(■), L₂(●) and L₃(▲) for α-ZnSe(*bda*)₀.₅

(**3**) at different temperatures. (Reproduced with permission from ref 16. Copyright ©

2013 WILEY-VCH Verlag GmbH & Co. KGaA, Weinheim.)
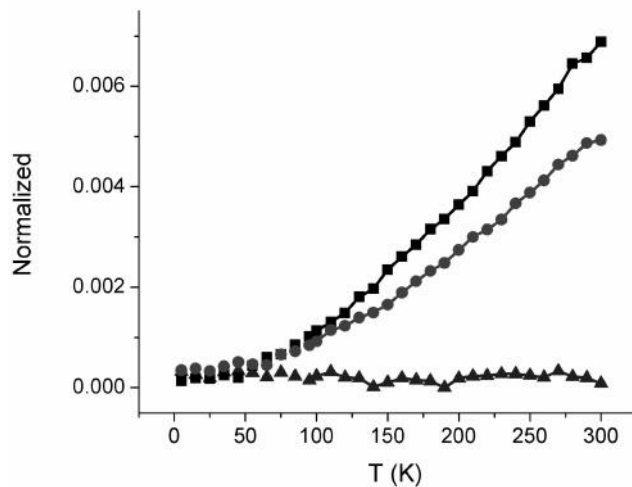
Figure 29: The normallized lattice constants L$_1$(■), L$_2$(●) and L$_3$(▲) α-ZnSe(*ptda*)$_{0.5}$ (**4**) at different temperatures. (Reproduced with permission from ref 16. Copyright © 2013 WILEY-VCH Verlag GmbH & Co. KGaA, Weinheim.)

A closer look at the differences in the three axes of α-ZnSe(*en*)$_{0.5}$ suggests that the increase in |δL$_3$/L$_3$| over the temperature range 5-300K is less than 3.56×10^{-6}/K, which is nearly an order of magnitude smaller than |δL$_1$/L$_1$| (1.74×10^{-5}/K) and |δL$_2$/L$_2$| (9.04×10^{-6}/K). Since the thermal expansion along the L$_1$ and L$_2$ axis is dominated by the inorganic ZnSe layers, the observed thermal behavior along these axes reflects primarily the in-plane expansion of inorganic layers. Figure 30 shows the comparison of the (110) plane of the würtzite ZnSe structure (left) and inorganic layer of the ZnSe(*en*)$_{0.5}$ structure (right) at 280K.
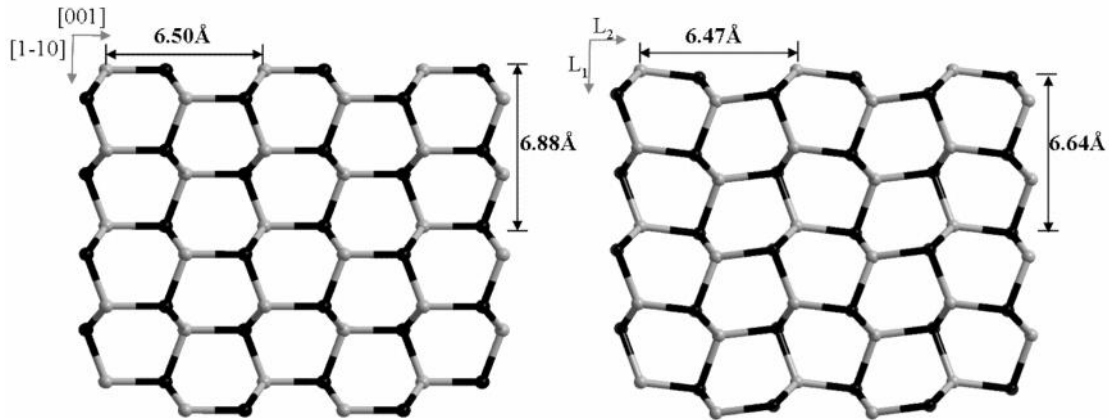
Figure 30: Comparison of a single (110) plane of the würtzite ZnSe (left) and a single inorganic slab of ZnSe(*en*)$_{0.5}$ (right). The L$_1$ and L$_2$ axes of the ZnSe(*en*)$_{0.5}$ structure are *a* and *b*, respectively. Zn: grey balls; Te: black balls. (Reproduced with permission from ref 16. Copyright © 2013 WILEY-VCH Verlag GmbH & Co. KGaA, Weinheim.)

As shown in the figure 30, the L$_2$ axis in the ZnSe(*en*)$_{0.5}$, with the cell parameter L$_2$ = *b* = 6.47 Å, can be related to the [001] (or *c*) axis of the hexagonal ZnSe structure, with the value of *c* = 6.50 Å at room temperature. Thus, the ZnSe(*en*)$_{0.5}$ hybrid structure shows about 0.5% compression compared to the parent ZnSe structure along this direction. Its L$_1$ (or *a*) axis can be related to the [1-10] direction in ZnSe parent structure (6.88 Å). With a length of 6.64 Å, L$_1$ exhibits a compression of ~4% along this direction, significantly higher than that along L$_2$. The stronger distortion in the L$_1$ axis is apparent as shown in Figure 27. It appears that the more compressed L$_1$ axis is more likely to expand to release the strain and thus a higher thermal expansion coefficient of $|\delta L_1/L_1| = 1.74 \times 10^{-5}$/K. While for the less compressed L$_2$ axis, a lower thermal expansion coefficient $|\delta L_2/L_2| =$

9.04×10^{-6}/K, close to the thermal expansion coefficient of 8.47×10^{-6}/K of the ZnSe würtzite structure in the same temperature range, is obtained.

A comparison of the thermal expansion behavior of short axes (L_1 and L_2) among all four compounds reveals some interesting findings. In general, as the number of carbon atoms increases from **1** to **4**, the thermal expansion coefficient of L_1 axis increase sequentially: **1** (17.4×10^{-6}) < **2** (18.9×10^{-6}) < **3** (20.5×10^{-6}) < **4** (23.1×10^{-6}) (see Table 8). Similar trend is also observed in the L_2 axis. The TE coefficient increases are in the order of: **1** (9.04×10^{-6}) < **3** (10.1×10^{-6}) and **2** (12.2×10^{-6}) < **4** (15.6×10^{-6}). Note the extent of increase is different for compounds with even and odd number of carbons. The thermal expansion behaviors of the title compounds α-ZnSe(L)$_{0.5}$ are also compared with their ZnTe analogues α-ZnTe(L)$_{0.5}$.[28] For the ZnTe(L)$_{0.5}$ structures the extent of thermal expansion (measured on single crystals) is in the order of L_1, L_2, and L_3, in agreement with the thermal expansion trend of α-ZnSe(L)$_{0.5}$ powders. The two short axes that are parallel to the inorganic layers respond positively to the increase of temperature and their thermal expansion coefficients varying between $(1.4-2.9) \times 10^{-5}$ K^{-1} and $(0.9-1.5) \times 10^{-5}$ K^{-1} for L_1 and L_2, respectively, in the temperature range of 95-295K. These values are comparable to those of the corresponding ZnSe(L)$_{0.5}$ phases, $(1.74-2.31) \times 10^{-5}$ K^{-1} and $(0.90-1.56) \times 10^{-5}$ K^{-1} for L_1 and L_2 (5-300K). For L_3, the ranges for four different compounds are $(-0.78-3.56) \times 10^{-6}$ K^{-1}. Therefore, both α-ZnTe(L)$_{0.5}$ and α-ZnSe(L)$_{0.5}$ materials show anisotropic thermal expansion behavior with the same trends of $L_1 > L_2 > L_3$. Compared to the short

axes L_1 and L_2 that reflect the TE behavior of the inorganic layers only, the thermal expansion behavior of L_3 axis, which is perpendicular to the ZnSe layers, is a combined effect of both the organic and inorganic component. For compounds **1** and **3** with centrosymmetic space group *Pbca*, the thermal expansion coefficients of the *c*-axis (L_3) are similar (3.39×10^{-6} and 3.56×10^{-6} K^{-1} for **1** and **3**, respectively, indicating the nearly zero thermal expansion along this axis. For compounds **2** and **4** crystallized in noncentrosymmetric space group *Cmc2$_1$*, the thermal expansion coefficients of the *a*-axis (L_3) are very different, with a PTE for **2 (**3.32×10^{-6}/K**)** and a NTE for **4** (-7.8×10^{-7}/K). The latter value is among the smallest values reported to date, for instance -5×10^{-7} for $Mn_3(Ga_{0.5}Ge_{0.4}Mn_{0.1})(N_{1-x}C_x)$[20] and 5.6×10^{-7} for $(1-x)PbTiO_3-xBi(Mg,Ti)_{1/2}O_3$[34]. The observed trend along the L_3 axis is similar to that of the α-ZnTe(*L*)$_{0.5}$ (*L* = *hz*, *en*, *pda*, *bda* and *ptda*) compounds, which also display a conversion from small PTE to NTE as the number of carbon atoms in the diamine molecules reaches to a certain level ($n = 2$).

To better understand the negative thermal expansion effect in the organic diamine molecules, we examined the structures of ZnSe(*ptda*)$_{0.5}$ at 5K and 280K closely and compared the related bond lengths and angles in detail (see Figure 31). Clearly, all individual bond lengths in the organic amine (*ptda*) show normal PTE effect, and thus, they are not the reason for the observed NTE effect. The shortest H⋯H distances (the distance between the two H atoms in the two nearest neighboring *ptda* molecules) are similar in both structures at 5 and 280K, with values of 3.456 Å and 3.468 Å at 5 and

280K, respectively. If the length of *ptda* is kept unchanged going from 280 to 5K, the above H⋯H distance would become significantly shorter than those in the structures at 5 and 280K. To avoid the crowded packing, the molecule stretches out along its chain axis, which is accompanied by an increase in all C-C-N and C-C-C angles. This in turn results in a negative thermal expansion effect on organic diamine.
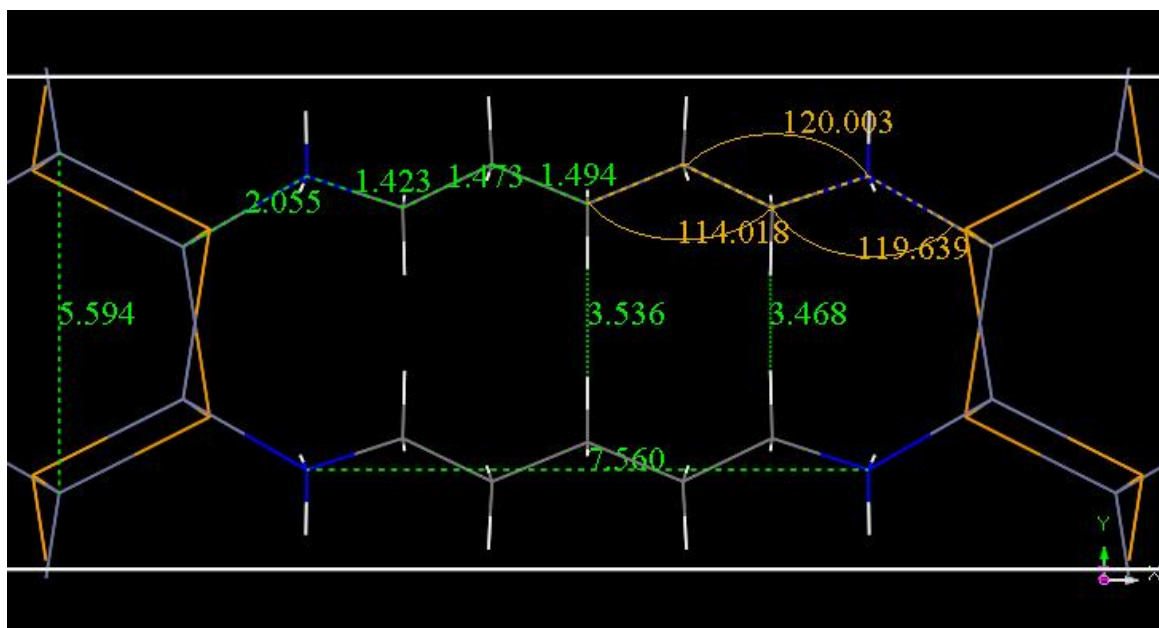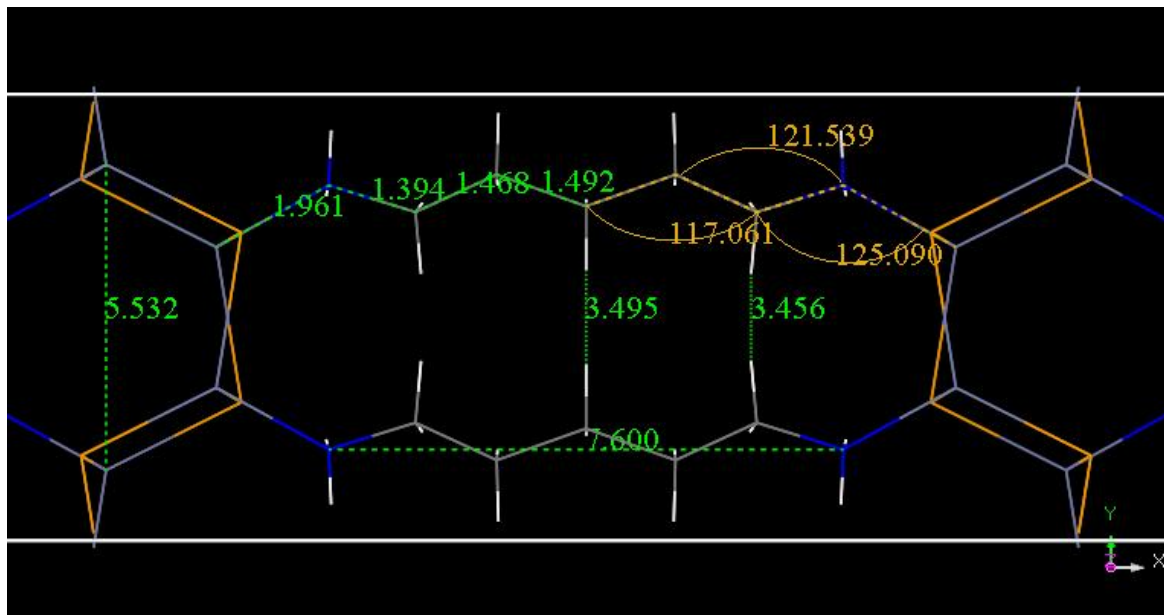
Figure 31: Bond distances and angles of *ptda* in the ZnSe(*ptda*)$_{0.5}$ structure at 280K (top)

and 5K (bottom). The closest distances between the two H atoms of the neighboring *ptda*

are 3.468 and 3.456Å at 280 and 5K, respectively. View is along L$_2$ or *c*-axis. (Reproduced

with permission from ref 16. Copyright © 2013 WILEY-VCH Verlag GmbH & Co. KGaA,

Weinheim.)

2.3 Summary

In summary, we have prepared and structurally characterized a group of inorganic-organic hybrid semiconducting materials with general formula $ZnSe(L)_{0.5}$. The thermal expansion coefficients along the layer stacking (L_3) axis are between -1×10^{-6} and 4×10^{-6} K^{-1} in the temperature range between 5K and 300K for all four structures, indicating a nearly-zero linear thermal expansion in the direction. A very small negative thermal expansion coefficient of -7.8×10^{-7} K^{-1} is achieved for $ZnSe(ptda)_{0.5}$ along the L_3 axis, which is among the smallest values reported to date (5.6×10^{-7} for $(1-x)PbTiO_3–xBi(Mg,Ti)_{1/2}O_3$ and -5×10^{-7} for $Mn_3(Ga_{0.5}Ge_{0.4}Mn_{0.1})(N_{1-x}C_x)$). The NTE effect observed in the organic diamines is a structural response to maintain a stable geometry as the PTE changes take place in the inorganic layers. Since the length of both the organic and inorganic layers can be independently varied, these hybrid structures have the capability to systematically tune the thermal expansion properties at a large scale.

3. VI-VI inorganic organic hybrid semiconductors

3.1 $MO_3(L)$ (L= organic ligand) structures

Inspired by the success with the II-VI chalcogenide derived hybrid semiconductors, we looked further into important oxide semiconductors as parent structures for new hybrid systems. The WO_3 and MoO_3 semiconductors and their derivatives have been extensively studied owing to their unusual electric, optic and thermal properties with many potential applications.[17,18] For example, WO_3 have widely been studied in photochemical water oxidation and dye-sensitized solar cell due to its desired band structure, to further increase water oxidation efficiency and photoelectric conversion efficiency, people have made great efforts in adjusting the band gap and femi level by making nanostructures or doping in WO_3.[33-35] In addition, scientists dealing with energy issue have considered MoO_3 and WO_3 as good candidates for lithium ion battery and electrochromic window due to their high lithium ion capacity and outstanding coloration efficiency.[57,106] Both of the applications require fast lithium ion intercalation/deintercalation process and layered structures with large surface/volume ratio are always desired. Furthermore, MoO_3 were also combined with polymers to make composite thermoelectric source.[67] By increasing the interface induced phonon scattering, the thermoconductivity is apparently reduced, which is the most important approach to increase figure of merit in thermoelectrics. Based on facts and considerations stated above, we have designed a novel system of $MO_3(L)$ (L=organic

linker) that contain 1D, 2D and 3D periodically ordered nanostructures under mild solvothermal conditions. By inserting different neutral organic linkers inside the parent MO_3 perovskite structure, the tunable band structures, the chainlike and layered inorganic VI-VI structural motifs and the desired interfaces between inorganic and organic layers can be achieved.

3.1.1 3D-MO₃(*L*)(*L*= organic ligand) structures

3.1.1.1 3D-MoO₃(*pyz*)₀.₅ (*pyz = pyrazine*)

3D-MoO₃(*pyz*)₀.₅ (*pyz = pyrazine*)] (**1**) was prepared from the reactions of MoO_3 (0.16 g), $CuCl_2 \cdot 2H_2O$ (0.10 g), pyrazine (0.22g) and 10 ml H_2O in a 23 mL acid digestion bomb at 160 °C for 5d. The dark blue powders were washed with water and 95% ethanol and then heated in the air at 150° C for 12h. The orange powder of **1** was collected in 50% yield based on MoO_3.[107]

3D-MoO₃(*pyz*)₀.₅ crystallizes in a non-centrosymmetric space group I222. The structure of **1** consists of layers of corner-sharing [108] octahedra parallel to the ab plane linked through pyrazine molecules into a 3D molybdenum oxide/pyz chiral framework. The 3D architecture of **1** can be described as an interwoven net of inorganic metal oxide layers linked by organic tethers. The molybdenum oxide layers are stacked along the c axis alternatively in an ABAB…sequence. One-dimensional rectangular channels along the *b* axis circumscribed by six [108] octahedra and two pyz molecules are as a result of the connectivity between the molybdenum oxide layers and pyrazine molecules.

Molybdenum atoms coordinate with one terminal oxo group, four bridging oxo groups and one pyz nitrogen donor with Mo–O bond lengths of 1.681(3), 2×1.923(3), 2×1.929(3) Å and the Mo–N length of 2.483(3) Å. This geometry is different from the common 'two short–two intermediate–two long' bond length pattern of molybdenum oxides. The significant lengthening in the Mo–N distance is caused by the strong trans effects of the terminal oxo group. The carbon atom of organic linker is distorted, and the fourfold crystal symmetry of **1** is prevented.

(a)   (b)
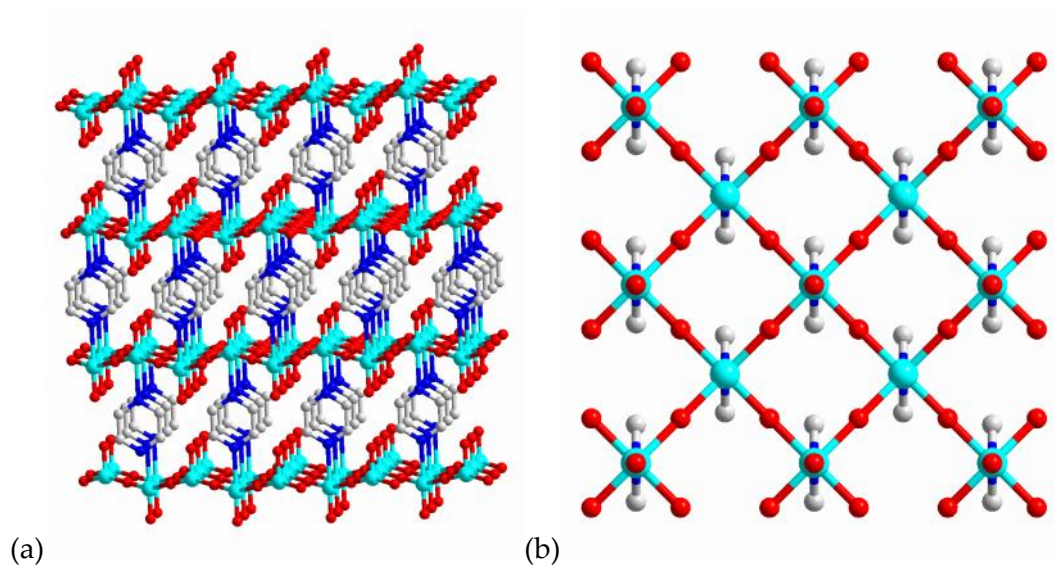
Figure 32: A view of the structure of 3D-MoO$_3$(*pyz*)$_{0.5}$ through (a) a-axis and (b) c-axis.

3.1.1.2 3D-WO$_3$(*pyz*)$_{0.5}$ (*pyz = pyrazine*)

3D-WO$_3$(*pyz*)$_{0.5}$ (*pyz = pyrazine*)] (**2**) was prepared from the reactions of W(0.072g), 3Na$_2$WO$_4$·9WO$_3$·H$_2$O (0.36 g), pyrazine (0.072 g) and 8 ml H$_2$O in a 23 mL acid digestion bomb at 150 °C for 7 days. After systematic cooling with the speed of 0.1 °C /min to room temperature, dark blue black crystals of **2** were collected by vacuum filtration and dried (yield ca. 50% based on 3Na$_2$WO$_4$·9WO$_3$·H$_2$O).[109]

The structure of WO$_3$(pyz)$_{0.5}$ crystallizes in tetrahedral lattice with the space group of *I*4/*mmm*. Though the symmetry of compound **2** is different from **1**, the structures of compounds are still very similar. WO$_3$(*pyz*)$_{0.5}$ **2** also consists of layers of corner sharing {WO5N} octahedra parallel to the ab-plane linked through pyrazine molecules into a 3D tungsten oxide/pyz framework. The tungsten oxide layers are stacked along the *c* axis alternatively in an ABAB… sequence. One-dimensional rectangular channels along the *b* axis circumscribed by six {WO5N}octahedra and two pyz molecules are as a result of the connectivity between the tungsten oxide layers and pyrazine molecules. The size of the channels is about 7.7 × 5.2 Å. Tungsten atoms coordinate with one terminal oxo group, four bridging oxo groups and one pyz nitrogen donor with W–O bond lengths of 1.680(2), 4 × 1.8741(3) Å and W–N bond length of 2.440(3) Å.

The experimental XRD pattern of the as-prepared WO$_3$(*pyz*)$_{0.5}$ matches pretty well with its simulated pattern, indicating the pure phase of the resulted compound.

Figure 33: Experimental (black) and simulated (red) XRD patterns of 3D-WO$_3$(*pyz*)$_{0.5}$.

3.1.1.3 3D-MoO$_3$(*4,4'-bpy*)$_{0.5}$ (*4,4'-bpy = 4,4'-bipyridine*)

3D-MoO$_3$(*4,4'-bpy*)$_{0.5}$ (*4,4'-bpy = 4,4'-bipyridine*)] (**3**) was obtained from reactions of MoO$_3$ (0.152 g), 4,4'-bipyridine (0.144 g), and H$_2$O (6 mL) in a 23 mL acid digestion bomb at 150 °C for 5 d. The product was washed by water, ethanol followed by drying in anhydrous ethyl ether. The orange crystals of **3** (70% highest yield based on MoO$_3$) were isolated.[108]

The structure of MoO$_3$(*4,4'-bpy*)$_{0.5}$ consists of layers of corner-sharing MoO5 square pyramids linked through 4,4'-bipyridyl groups into a 3D covalently bonded metal oxide-organic ligand framework. The overall structure of MoO$_3$(*4,4'-bpy*)$_{0.5}$ may be described in terms of alternating inorganic metal oxide layers and organic layers. The

distorted MoO5N coordination geometry at each Mo site is defined by a terminal oxo group, four asymmetrically bridging oxo groups, and a pyridyl nitrogen group and has the typical "two short, two intermediate, and two long" bond length geometry which is common to MoO_3. The long Mo-N distances, 2.412(6) Å, reflect the strong trans influence of the terminal oxo group. This phenomenon has also been observed in structure **1** and **2**. The terminal Mo-O bond distances is 1.698(5) Å, and the bridging Mo-O bond distances, range from 1.763(5) to 2.120(5) Å. These numbers are within the range expected for molybdenum oxides.

(a)   (b)

(c)
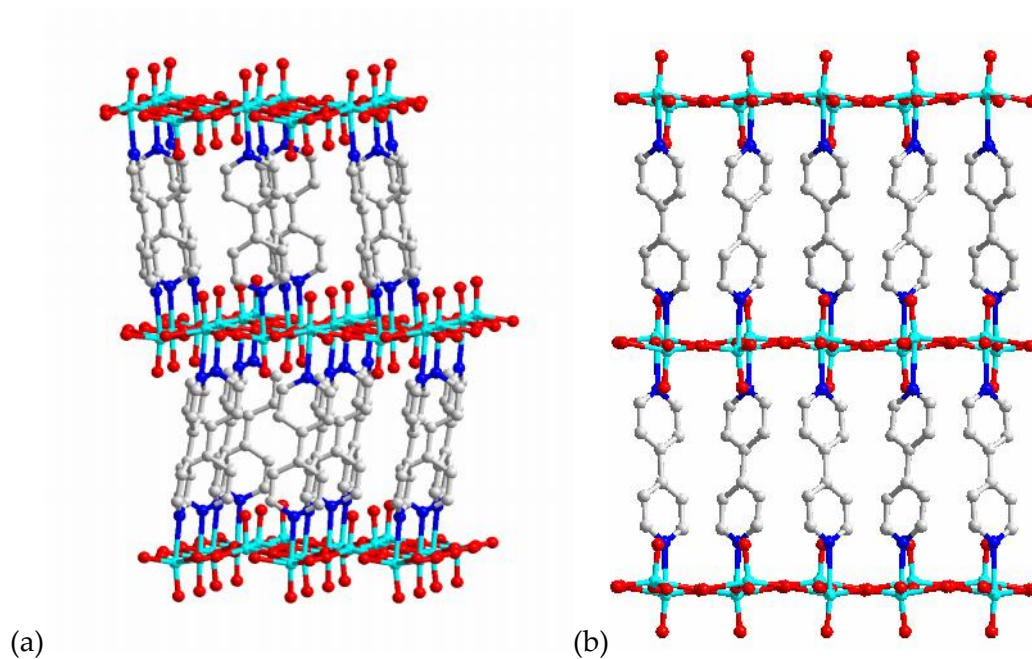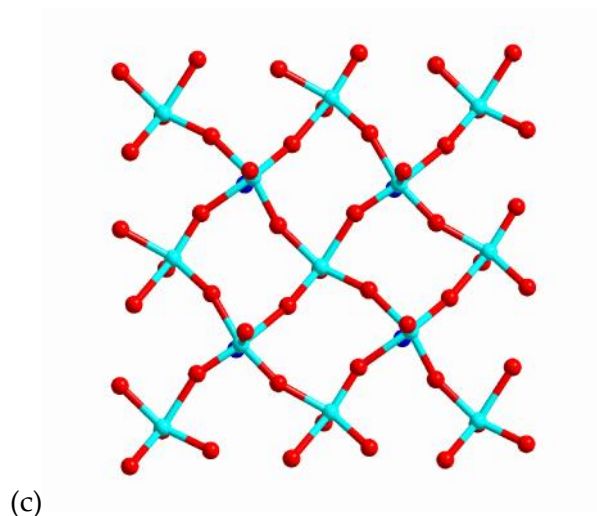
Figure 34: A view of the structure of 3D-MoO$_3$($4,4'$-bpy)$_{0.5}$ through (a) a-axis, (b) b-axis and (c) c-axis.

The experimental XRD pattern of the as-prepared MoO$_3$($4,4'$-bpy)$_{0.5}$ matched pretty well with its simulated pattern, indicating the pure phase of the resulted compound.

[Simu_MoO3(44bpy)0.5(2D).raw]
[MoO3(bpy)0.5_Exp.mdi]

Figure 35: Experimental (black) and simulated (red) XRD patterns of 3D-MoO$_3$($4,4'$-*bpy*)$_{0.5}$.

3.1.1.4 3D-WO$_3$($4,4'$-*bpy*)$_{0.5}$ ($4,4'$-*bpy* = $4,4'$-*bipyridine*)

Synthesis of 3D-WO$_3$($4,4'$-*bpy*)$_{0.5}$ ($4,4'$-*bpy* = $4,4'$-*bipyridine*): A mixture of $4,4'$-bipyridine (0.144 g), 3Na$_2$WO$_4$·9WO$_3$·H$_2$O (0.45 g), and H$_2$O (8 mL) were placed in a 23 mL acid digestion bomb and the Teflon-lined Parr acid digestion bomb was heated for 7 d at 150 °C under autogenous pressure. After allowing the reaction mixture to cool to room temperature, yellow crystal plates of 3D-WO$_3$($4,4'$-*bpy*)$_{0.5}$ ($4,4'$-*bpy* = $4,4'$-*bipyridine*) (4) were collected by filtration and dried at room temperature (yield ca. 70% based on tungsten oxide).[109]

The crystal lattice of compound **4** is orthorhombic and the space group is *Cmca.*

The topology of the structure is similar to compound **3**. The structure of **4** consists of W/O/N layers, parallel to the *ab*-plane, of corner sharing {WO5N} octahedra bridged through bipyridine ligands into a 3D covalent/coordination hybrid framework. The connectivity between the WO_3 layers and bpy molecules results in one-dimensional rectangular channels along the [110] direction circumscribed by six {WO5N} octahedra and two bpy molecules. The dimensions of the 1D rectangular channels are about 11.9 × 5.2 Å. The outer shell orbitals of tungsten site receive contributions from four bridging oxo groups, one terminal oxo group and one nitrogen donor with W–O bond lengths of 1.678(11), 2 ×1.8936(4), 1.851(13) and 1.897(12) Å, and W–N bond length of 2.409(14) Å.

The experimental XRD pattern of the as-prepared $WO_3(4,4'\text{-bpy})_{0.5}$ matched well with its simulated pattern, indicating the pure phase of the resulted compound.
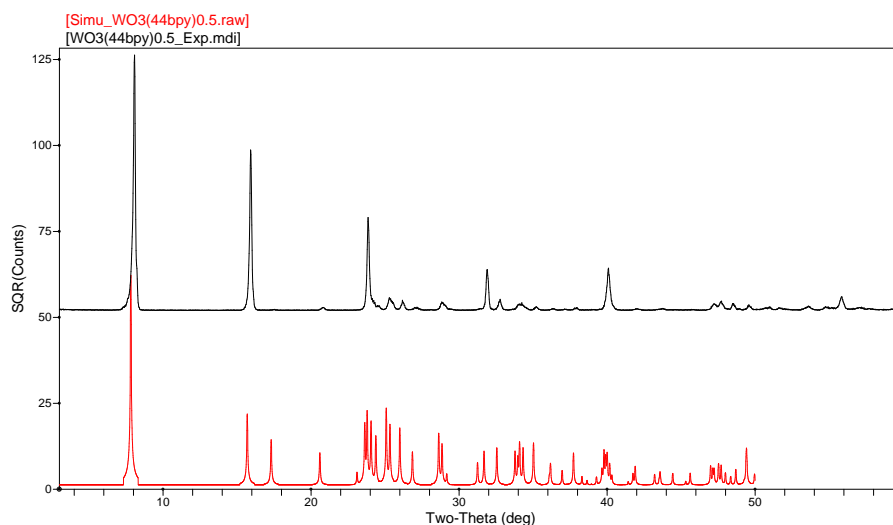
Figure 36: Experimental (black) and simulated (red) XRD patterns of 3D-WO$_3$(4,4′-bpy)$_{0.5}$.

3.1.1.5 3D-WO$_3$ (*bpe*)$_{0.5}$ (*bpe = 1,2-Di-(4-bypiridyl)ethane*)

3D-WO$_3$ (*bpe*)$_{0.5}$ (*bpe = 1,2-Di-(4-bypiridyl)ethane*)] (5) was prepared from the reactions of W (0.072g), 3Na$_2$WO$_4$·9WO$_3$·H$_2$O (0.36g), 1,2-Di-(4-bypiridyl)ethane (0.072g) and H$_2$0 (8ml) in a 23 mL acid digestion bomb at 150 °C for 7d. The dark blue crystals were washed with water and 95% ethanol and then heated in the air at 150 °C for 12h. The yellow crystals of **5** were collected in 40% yield based on tungsten.

Crystallographic data for 3D-WO$_3$ (*bpe*)$_{0.5}$ were collected with a Siemens P4 diffractometer equipped with the SMART CCD system and using Mo Kα radiation (λ = 0.71073 Å). The data were collected at 100 K and corrected for Lorentz and polarization effects. Absorption corrections were made by SADABS. The structure solution and refinement were carried out using the SHELXL97 software package. The structures were solved by direct methods, and all of the non-hydrogen atoms were located from the initial solution.

3D-WO$_3$ (*bpe*)$_{0.5}$ crystallizes in orthorhombic lattice with the space group of I-*42m*, and its unit cell parameters are a = 5.2546(3) Å, b = 5.2546(3) Å, c = 26.987(3) Å. The inorganic layers of compounds **5** are analogous to that of three-dimensional ReO$_3$-type WO$_3$ (r-WO$_3$). However, the inorganic layers in r-WO$_3$ are connected through shared corners forming a three-dimensional structure whereas the tungsten oxide layers in

compounds **5** are cross-linked by 1,2-Di-(4-bypiridyl)ethane through covalent/coordination bonds giving their 3D organic/inorganic hybrid structures.

(a)   (b)
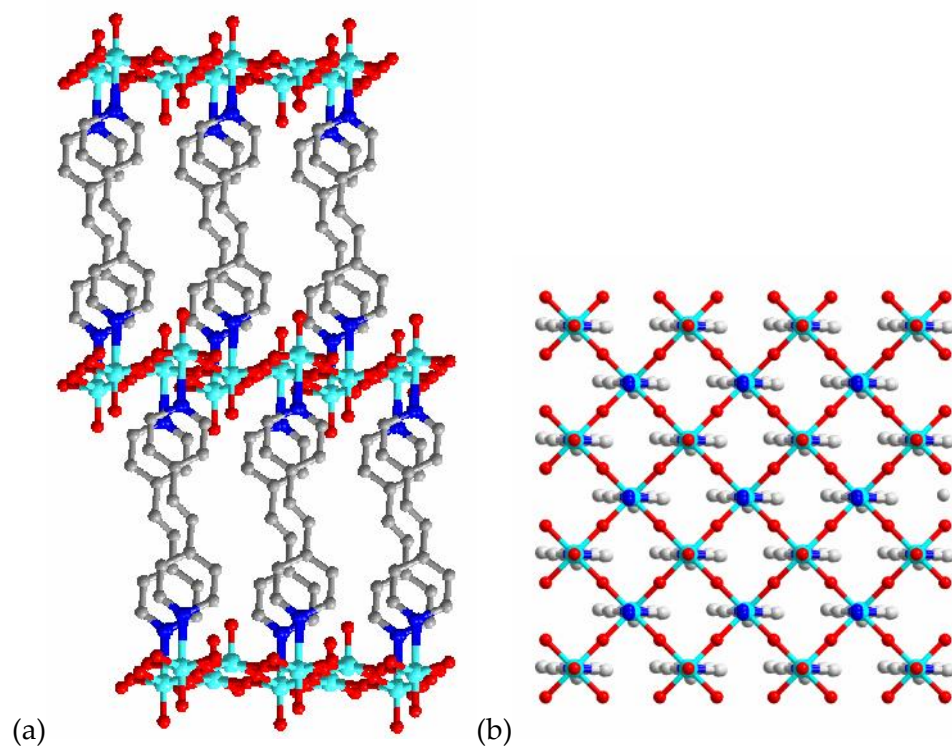
Figure 37: A view of the structure of 3D-WO$_3$(*bpe*)$_{0.5}$ through (a) a-axis and (b) c-axis.

The experimental XRD pattern of the as-prepared WO$_3$(*bpe*)$_{0.5}$ matched well with its simulated pattern, indicating the pure phase of the resulted compound.
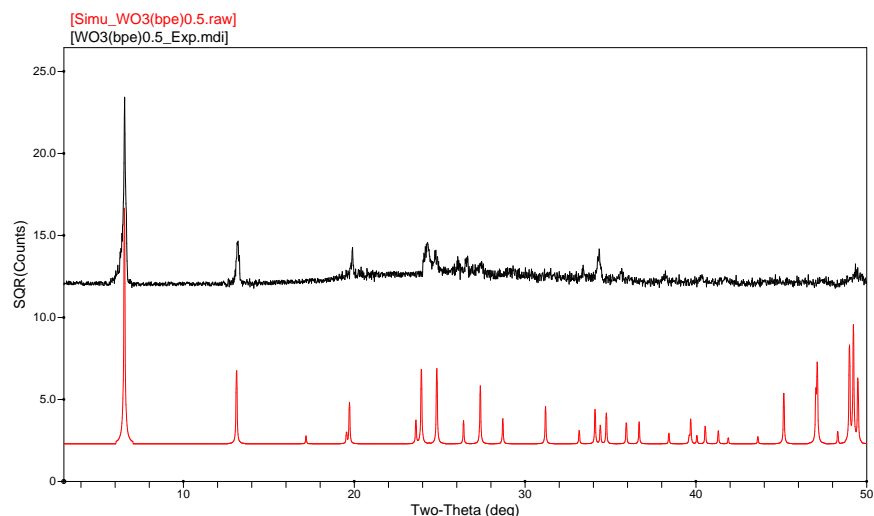
Figure 38: Experimental (black) and simulated (red) XRD patterns of 3D-WO₃(*bpe*)₀.₅.

3.1.2 2D-MO₃(L)(L= organic ligand) structures

3.1.2.1 2D-MoO₃(*py*) (*py = pyridine*)

Reactions of MoO₃ (0.15g, 0.25 mmol) and pyridine (0.5ml) at 150 °C for 20 days in thick-wall Pyrex tubes afforded yellow plate-like crystals of 2D-MoO₃(*py*) (*py = pyridine*) (6) (0.031g, 71.6% yield based on Se). The product was washed by ethanol, water and anhydrous ethyl ether in sequence. (yield ca. 80% based on MoO₃)

2D-MoO₃(*py*) crystallizes in the space group *Pbca*, with the unit cell parameter of a = 7.5228(4) Å, b = 7.3890(4) Å, c = 22.6080(13) Å. Similar to 3D-MoO₃(4,4′-*bpy*), the structure of 2D-MoO₃(*py*) consists of layers of corner-sharing MoO5 square pyramids. However, unlike the case of 3D-MoO₃(4,4′-*bpy*), in which the layers of MoO5 square

pyramids are linked through 4,4′-bipyridyl groups into a three-dimensional framework, the Mo atoms in 2D-MoO$_3$(*py*) only bond with one nitrogen donor of pyridine ligands, leading to a two dimemsional structure. The overall structure of 2D-MoO$_3$(*py*) can be described in terms of alternating MoO$_3$(*py*) layers that are packed in a way ABAB.... The long Mo-N distances, 2.395 Å on average, reflect the strong trans influence of the terminal oxo group. The terminal Mo-O bond distances of 1.693 Å, on average, and the bridging Mo-O bond distances, which range from 1.765 Å to 2.120 Å, strongly shows the asymmetric effect as its parent structure.

(a)　　　　　　　　　　(b)
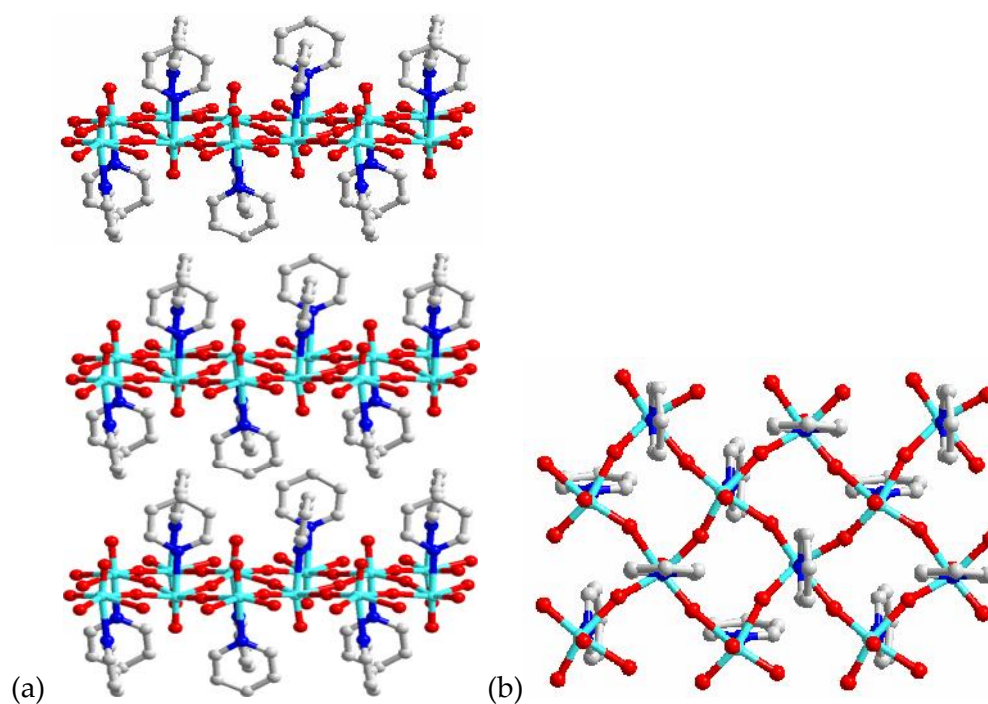
Figure 39: A view of the structure of 2D-MoO$_3$(*py*) through (a) a-axis and (b) c-axis.

The experimental XRD pattern of the as-prepared 2D-MoO$_3$(*py*) matched pretty well with its simulated pattern, indicating the pure phase of the resulted compound.
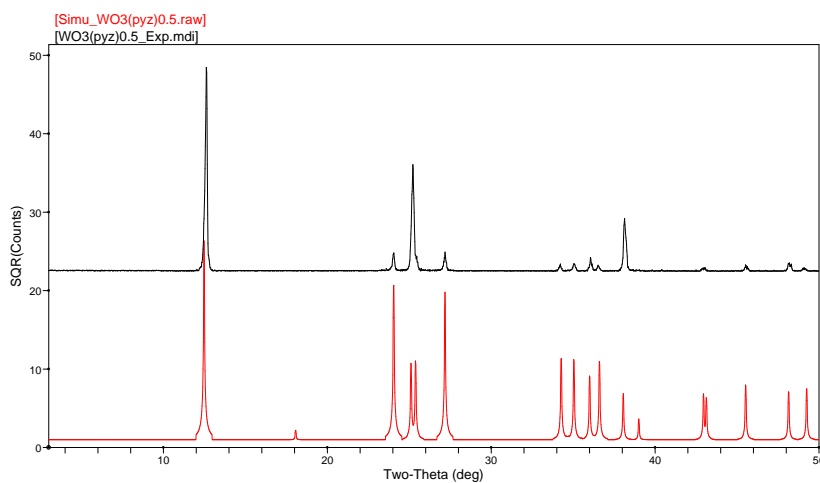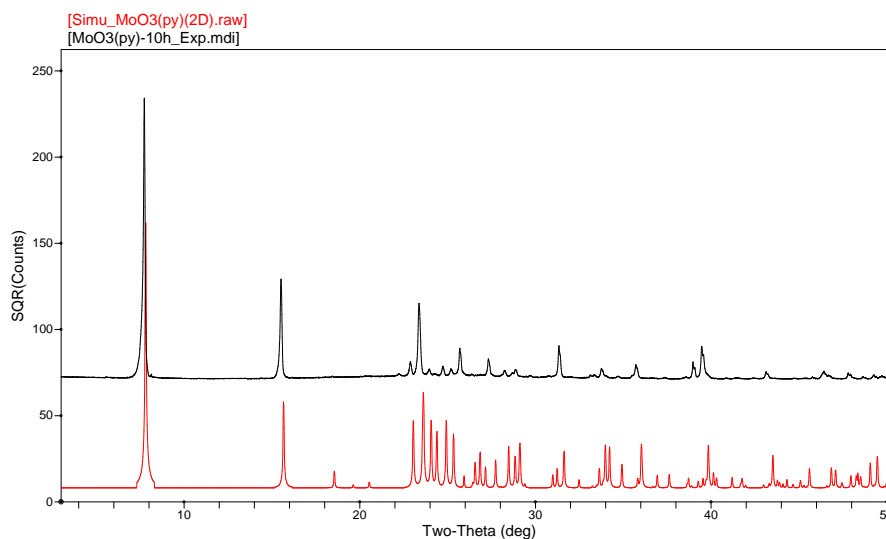
Figure 40: Experimental (black) and simulated (red) XRD patterns of 2D-MoO₃(*py*).

3.1.2.1 2D-WO₃(*py*) (*py* = *pyridine*)

A stoichiometric mixture of Bi_2O_3 and WO_3 was calcined at 800 C for 48 h to synthesize $Bi_2W_2O_9$. The products have been stirred in 1M hydrochloric acid for 5 days to afford the pure $H_2W_2O_7 \cdot xH_2O$. The formed $H_2W_2O_7 \cdot xH_2O$ (0.1 g) was then reacted with pyridine (0.5ml) at 150 °C for 10 days in thick-wall Pyrex tubes and give rise to yellow powders of 2D-WO₃(*py*) (*py* = *pyridine*) (**7**). The product was washed by ethanol, water and anhydrous ethyl ether in sequence. (yield ca. 70% based on tungsten)

Powder X-ray diffraction (PXRD) of 2D-WO₃(*py*) sample was performed on a Rigaku D/M-2200T automated diffraction system (Ultima IV). The structural analyses

were performed using JADE, PowderX and GSAS software packages. Due to the similarity of XRD patterns between 2D-WO$_3$(py) and 2D-MoO$_3$(py), we assumed the space group of 2D-WO$_3$(py) is same as that of 2D-MoO$_3$(py). And we also used other structural information of 2D-MoO$_3$(py) (e.g. lattice parameters and atomic positions) as reference to build 2D-WO$_3$(py) structural models for Rietveld refinement. The Rietvelt refinement results are shown below. The experimental (black dots) and simulated (red lines) XRD patterns matched pretty well, suggesting the proposed structure reflect real crystal structure to a large extent. The structure of 2D-WO$_3$(py) also crystallizes in monoclinic lattice with the space group of Pbca, the lattice parameters of which are: a=7.5024(0), b=7.4283(1), c=22.9359(2).
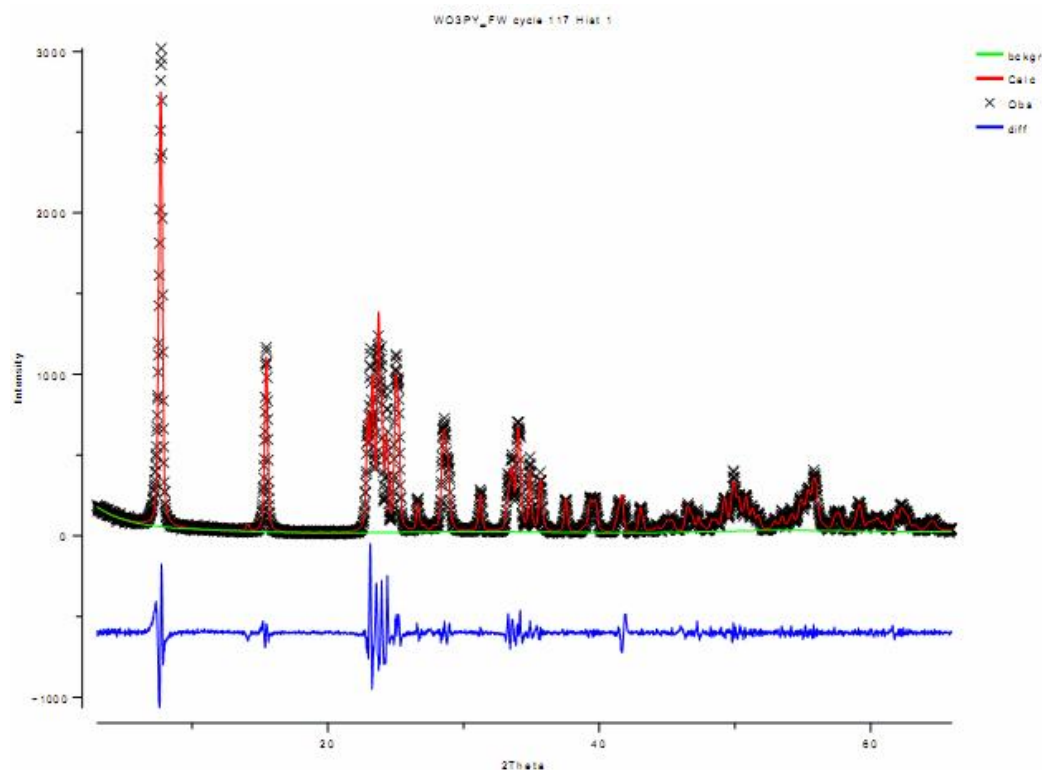
Figure 41: Experimental (black dots), simulated (red lines) XRD patterns of 2D-WO₃(*py*) and differences between them (blue line).

3.1.3 1D-MO$_3$(*L*)(*L* = organic ligand) structures

3.1.3.1 1D-MoO₃ (*4,4′-dm-2,2′-bpy*) (*4,4′-dm-2,2′-bpy = 4,4′-dimethyl-2,2′-bipyridine*)

1D-MoO₃ (*4,4′-dm-2,2-bpy*) (*4,4′-dm-2,2′-bpy = 4,4′-dimethyl-2,2′-bipyridine*) **(8)** was acquired by reacting MoO₃ (0.36 g) with 4,4′-dimethyl-2,2′-bipyridine (0.080 g) in the water solution at 150 °C for 5 days. Colorless crystals of **8** were collected after filtration.

1D-MoO$_3$ (*4,4'-dm-2,2-bpy*) (**8**) crystallizes in monoclinic lattice with the space group of P2$_1$/c, which has the lattice parameters of a = 3.7772(7) Å, b = 15.242(3) Å, c = 20.400(4) Å, β = 95.296(4). The structure of 1D-MoO$_3$ (*4,4'-dm-2,2-bpy*) (1) consists of one-dimensional chains of corner-sharing {MoO$_4$N$_2$} octahedra. The coordination geometry of each molybdenum is defined by two bridging oxo groups, two terminal oxo groups, and the two pyridyl nitrogen donors of the *4,4'-dimethyl-2,2'-bipyridine* chelate. The molybdenum site exhibits the two short-two intermediate-two long bond length pattern common to the molybdenum oxides. The Mo-bridging oxo group distances are unsymmetrical, giving rise to an infinite {…O=Mo…O=Mo} chain, with alternating short-long Mo-O distances of 1.792 and 2.074 Å, respectively.
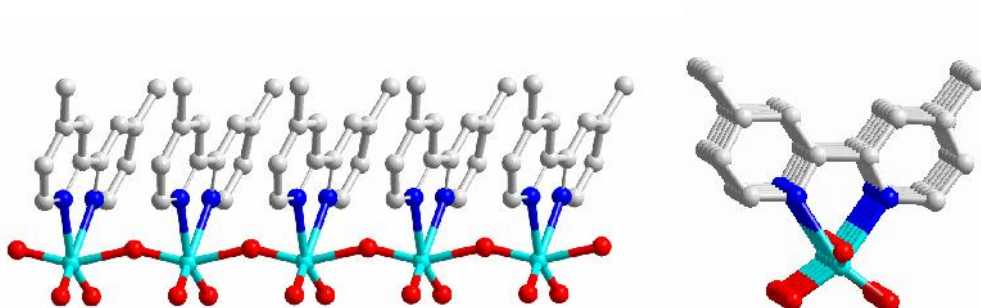
Figure 42: A view of the structure of 1D-MoO$_3$ (*4,4'-dm-2,2'-bpy*) through (left) a-axis and (right) c-axis.

The experimental XRD pattern of the as-prepared 1D-MoO$_3$ (*4,4'-dm-2,2'-bpy*) matched pretty well with its simulated pattern, indicating the pure phase of the resulted compound.
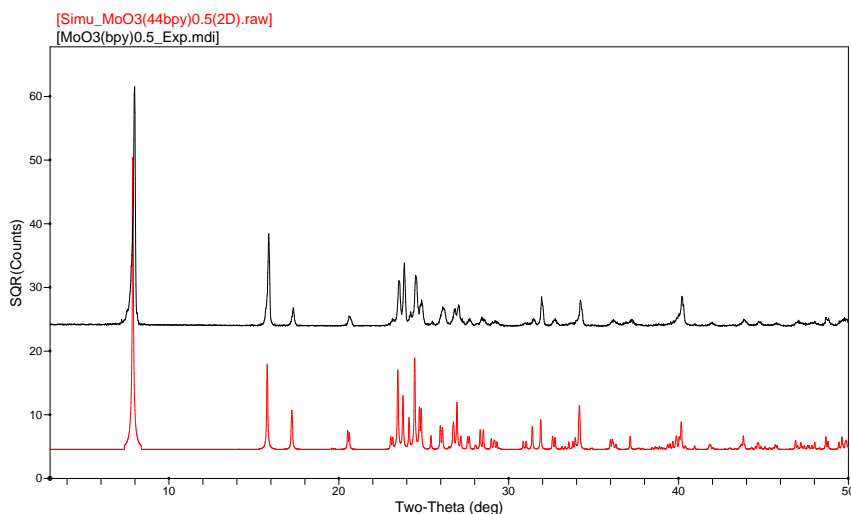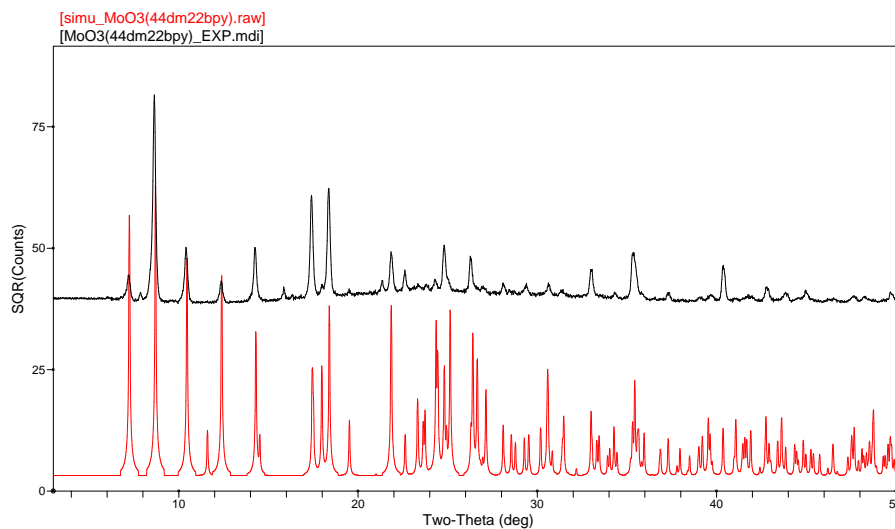
Figure 43: Experimental (black) and simulated (red) XRD patterns of 1D-MoO₃ (*4,4′-dm-2,2′-bpy*).

3.1.3.2   1D-WO₃   (4,4′-dm-2,2′-bpy)   (*4,4′-dm-2,2′-bpy   =   4,4′-dimethyl-2,2′-bipyridine*)

1D-WO₃ (*4,4′-dm-2,2′-bpy*) (*4,4′-dm-2,2′-bpy = 4,4′-dimethyl-2,2′-bipyridine*) (**9**) was acquired by reacting 3Na₂WO₄·9WO₃·H₂O (0.36 g) with 4,4′-dimethyl-2,2′-bipyridine (0.080 g) in the water solution at 150 °C for 5 days. White powders of **9** were collected after filtration.

Powder X-ray diffraction (PXRD) of 1D-WO₃ (*4,4′-dm-2,2′-bpy*) sample was performed on a Rigaku D/M-2200T automated diffraction system (Ultima IV). The structure analyses were carried out using JADE (Windows), PowderX and GSAS software packages. Due to the similarity of XRD patterns between 1D-WO₃ (*4,4′-dm-2,2′-*

bpy) and 1D-MoO$_3$ (*4,4′-dm-2,2′-bpy*), we assume the space group of 1D-WO$_3$ (*4,4′-dm-2,2′-bpy*) is same as that of 1D-MoO$_3$ (*4,4′-dm-2,2′-bpy*). And we also use other structural information of 1D-MoO$_3$ (*4,4′-dm-2,2′-bpy*) (e.g. lattice parameters and atomic positions) as reference to build 1D-WO$_3$ (*4,4′-dm-2,2′-bpy*) structural models for Rietveld refinement. The Rietvelt refinement results are shown below. The experimental (black dots) and simulated (red lines) XRD patterns matched pretty well, suggesting the proposed structure reflect real crystal structure to a large extent.

The structure of 1D-WO$_3$ (*4,4′-dm-2,2′-bpy*) (**9**) also crystallizes in monoclinic lattice with the space group of P2$_1$/c and the lattice parameters of the compound are a = 3.7218(2)Å, b = 15.3615(11) Å, c = 20.3618(15) Å and β=94.81(1)°.
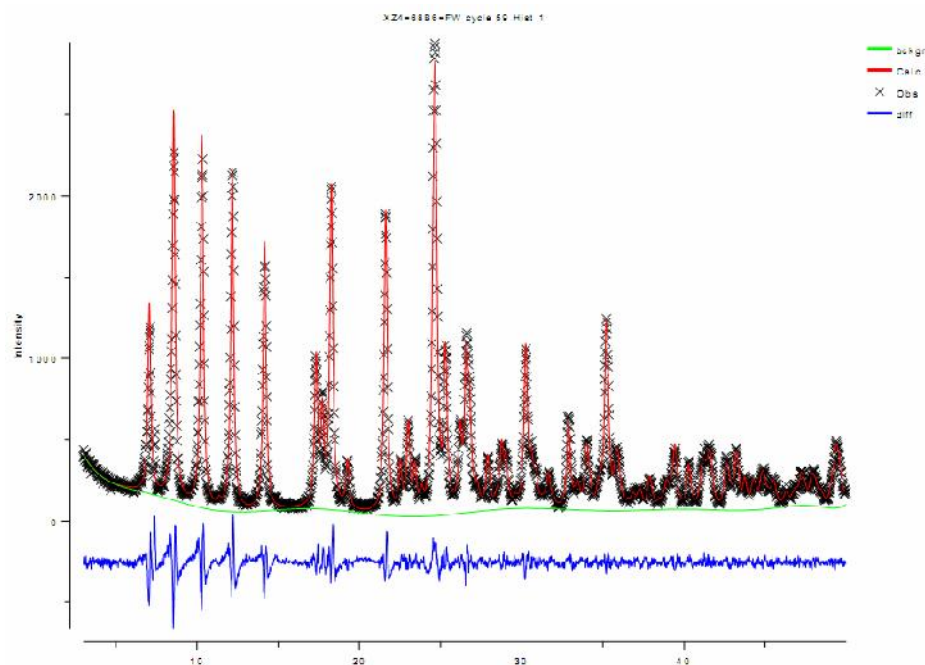
Figure 44: Experimental (black dots), simulated (red lines) XRD patterns of 1D-MoO₃
(*4,4'-dm-2,2'-bpy*) and differences between them (blue line).

3.1.4 Summary of MO₃(*L*)(*L*= organic ligand) structures

Based on the above discussion, we have developed a new class of inorganic
organic hybrid semiconductors based on VI-VI metal oxides such as MoO_3 or WO_3.

Three novel structures, [3D-WO₃ (*bpe*)₀.₅ (*bpe = 1,2-di-(4-bypiridyl)ethane*)](**5**), 2D-
MoO₃(*py*) (*py = pyridine*) (**6**), and [1D-MoO₃ (*4,4'-dm-2,2'-bpy*) (*4,4'-dm-2,2'-bpy = 4,4'-
dimethyl - 2,2'-bipyridine*)](**9**), represent the examples of MO₃(*L*) hybrid materials (see
Figure 42) of which uniform structures are formed via direct, covalent bonds between
the inorganic host (the VI-VI semiconductor) and the organic spacers. For 3D and 2D

hybrid structures, they consist of inorganic layers of corner-sharing {WO$_5$N} or octahedra linked with organic molecules to form 3D or 2D framework. This can be described as a single "slice" which is cut from the parent structure and one oxygen in MO$_6$ octahedra of WO$_3$ or MoO$_3$ perovskite phase is substituted by the nitrogen atom in the pyridine ring of organic molecules. While for 1D structure, each tungsten atom is octahedrally coordinated to four oxygen atoms and two nitrogen atoms from a chelating 4,4′-dimethyl-2,2′-bipyridine molecule. {WO$_4$N$_2$} octahedra are interconnected with oxygen atom, forming an infinite WO$_2$N chain. This can be described as a single "chain" cut from the parent WO$_3$ perovskite phase with two oxygen in WO$_6$ octahedra substituted by the two nitrogen atoms in the 4,4′-dimethyl-2,2′-bipyridine.

(a)   (b)
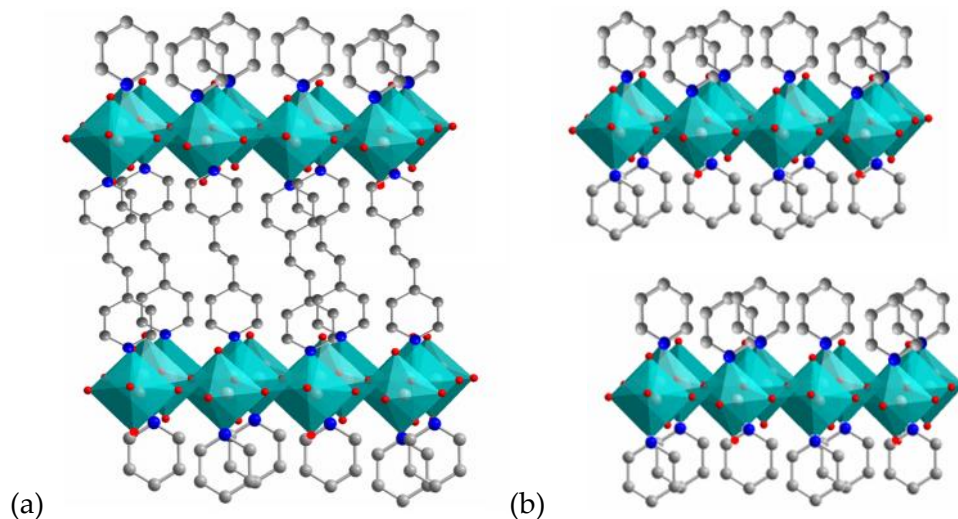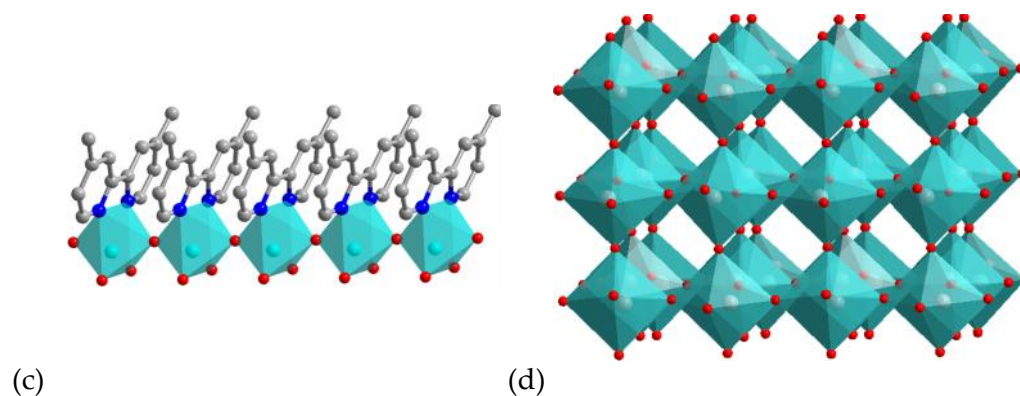
Figure 45: Crystal structures of (a) 3D-WO$_3$(*bpe*)$_{0.5}$ (**5**), (b) 2D-MoO$_3$(*py*) (**6**), (c) 1D-WO$_3$ (*4,4'-dm-2,2'-bpy*) (**9**), (d) MoO$_3$ or WO$_3$ perovskite structures.

The structural information of all the listed compounds including their unit cell parameters and space groups are shown below.

Table 9: List of compounds[107-109] with their unit cell parameters, space groups, and band gaps.

Compounds	Unit cell Parameters (Å)	SG[a]
3D-MoO$_3$ (*pyz*)$_{0.5}$ (**1**)	a=5.2702(15) b=5.2674(7) c=14.2310(11)	I222
3D-WO$_3$ (*pyz*)$_{0.5}$ (**2**)	a=5.2288(7) b=5.2288(7) c=14.175(3)	I4/mmm
3D-MoO$_3$(*4,4'-bpy*)$_{0.5}$ (**3**)	a= 7.5727(6) b=7.3675(7) c= 22.433(3) β=90.396(8)	P2$_1$/c

3D-WO$_3$(*4,4'-bpy*)$_{0.5}$ (**4**)	a=7.4733(15) b=7.3927(15) c= 22.570(4)	Cmca
3D-WO$_3$(*bpe*)$_{0.5}$ (**5**)	a=5.2546(3) b=5.2546(3) c= 26.987(3)	I-42m
2D-MoO$_3$(*py*) (**6**)	a=7.5228(4) b=7.3890(4) c=22.6080(13)	Pbca
2D-WO$_3$(*py*) (**7**)	a=7.5024(0) b=7.4283(1) c=22.9359(2)	Pbca
1D-MoO$_3$(4,4'-dm-2,2'-bpy) (**8**)	a=3.7772(7) b=15.242(3) c=20.400(4) β=95.296(4)	P2$_1$/c
1D-WO$_3$(4,4'-dm-2,2'-bpy) (**9**)	a=3.7218(2) b=15.3615(11)c=20.3618(15) β=94.81(1)	P2$_1$/c

3.2 Optical absorption properties of MO$_3$(L)

The optical absorption spectra of 3D-MoO$_3$ (*pyz*)$_{0.5}$ (**1**), 3D-MoO$_3$(*4,4′-bpy*)$_{0.5}$ (**3**), 2D-MoO$_3$(*py*) (**6**) and 1D-MoO$_3$(*4,4′-dm-2,2′-bpy*) (**8**) and MoO$_3$ parent structure were measured by diffuse reflectance experiments at room temperature with a Shimadzu UV-3101PC double beam, double monochromator spectrophotometer. Data were collected in the wavelength range of 300-800 nm and converted using the Kubelka-Munk function.. BaSO$_4$ powder was used as a standard (100% reflectance). The scattering coefficient (S) was treated as a constant since the average particle size of the samples used in the measurements was greatly larger than 5 nm, and the results are plotted in Figure 46, along with that of perovskite MoO$_3$. The absorption edges for **1**, **3** and **6** are found to be of 2.2, 2.3, and 2.4 eV, respectively. Compared to the measured value of 2.9 eV for perovskite type MoO$_3$, it clearly indicates a very significant red shift (0.7, 0.6 and 0.5 eV, respectively).
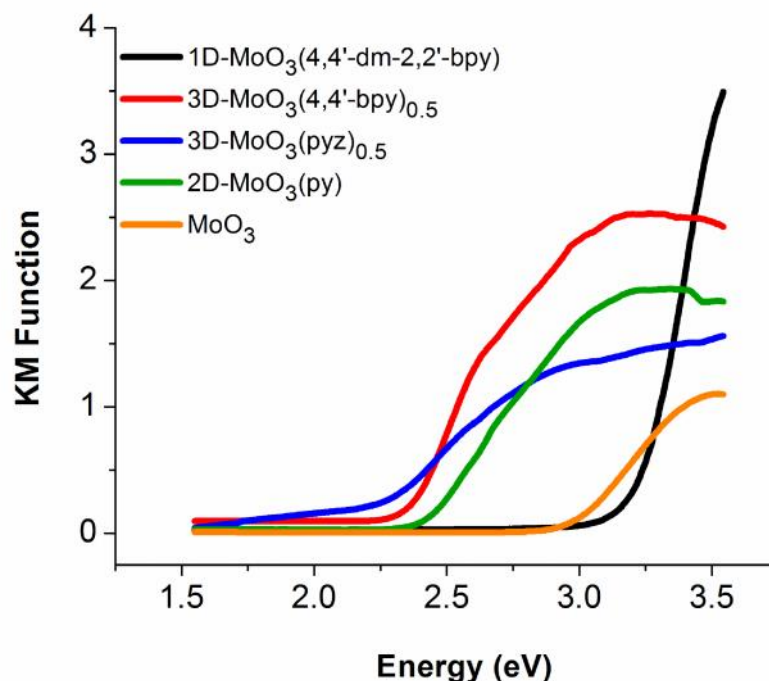
Figure 46: Optical absorption spectra of MoO₃(*L*) inorganic organic hybrid semiconductors and the MoO₃.

It is also interesting to note the extent of band edge shifts among these compounds. The band edge adsorption of three dimensional compounds 3D-MoO₃(*pyz*)₀.₅ (**1**), and 3D-MoO₃(*4,4'-bpy*)₀.₅ (**3**) are lower compared to 2D-MoO₃(*py*) (**6**) and even lower than 1D-MoO₃(*4,4'-dm-2,2'-bpy*) (**8**). And the band gap of 3D-MoO₃(*pyz*)₀.₅ (**1**) with organic linker of pyrazine shows 0.1 eV lower than 3D-MoO₃(*4,4'-bpy*)₀.₅ (**2**) with longer organic linker of 4,4'- bipyridine.

Density functional theory (DFT) calculation was applied to the chosen compounds **3**, **9** and MoO₃ parent structure to explain the band gap shift (see Figure 47).

Compared to 0.53 eV, the band gap of MoO_3, **3** and **9** show larger values of 1.685 eV and 2.715 eV respectively. This trend is corresponding to what we observed in II-VI hybrid materials, when the dimension of inorganic structures is reduced from 3D to 1D, strong quantum confinement effect results in larger fundamental band gap[6,110,111]. In addition, the calculation results reveal the indirect band gap of MoO_3 but direct band gap of both **3** and **9**, the latter one is always desired for semiconductors with different kind of applications.
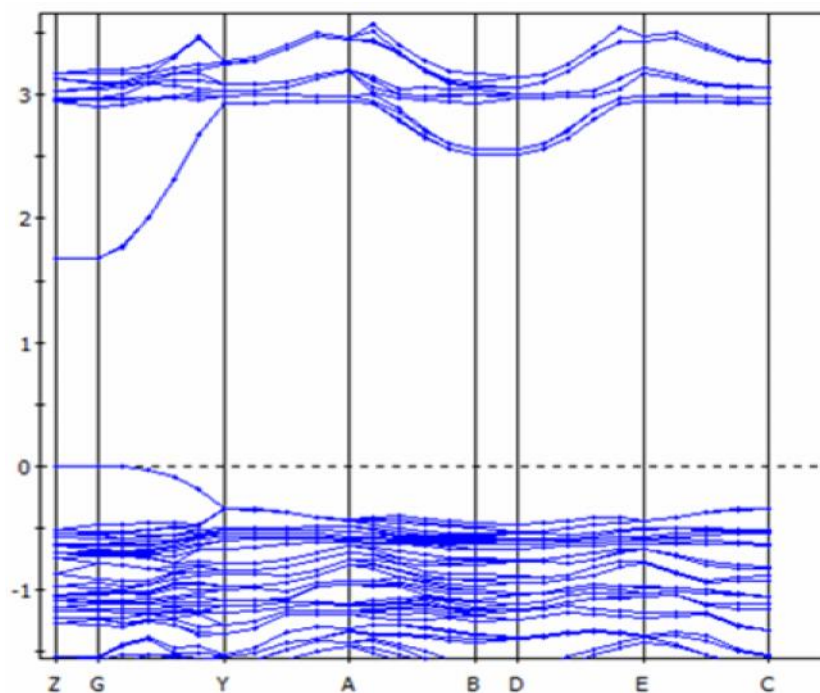
Figure 47: Band structure of 3D-MoO_3(*4,4'-bpy*)$_{0.5}$ with direct band gap of 1.685 eV.
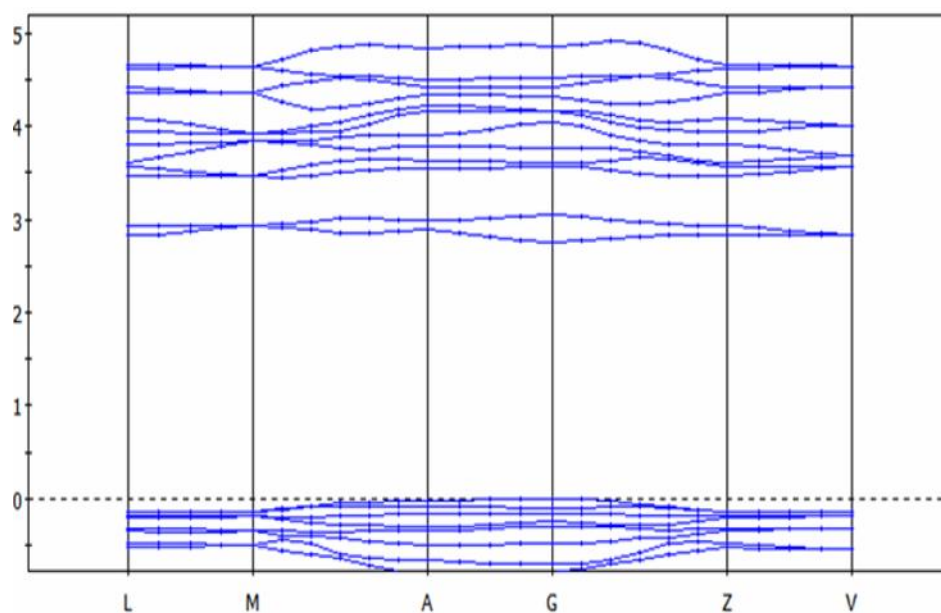
Figure 48: Band structure of 1D-MoO$_3$ (*4,4'-dm-2,2'-bpy*) with direct band gap of 2.715eV.
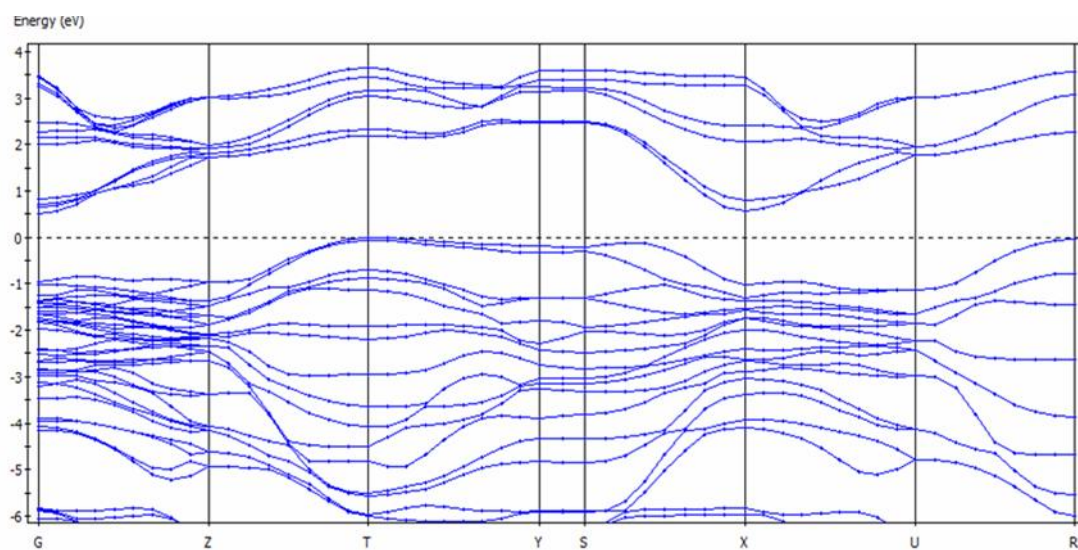
Figure 49: Band structure of MoO$_3$ with indirect band gap of 0.513eV.

The atomic contribution to valence band and conduction band can be studied by looking into the density of state results plotted in both inorganic part and organic part of 3D-MoO$_3$(*4,4'-bpy*)$_{0.5}$ and 1D-MoO$_3$ (*4,4'-dm-2,2'-bpy*) hybrid structures.

Figure 49 reveals that the 2p-obitals of oxygen atoms in 3D-MoO$_3$(*4,4'-bpy*)$_{0.5}$ inorganic layer contribute significantly more to the valence band, compared to 2p-obitals of nitrogen atoms and 2p-obitals of carbon atoms, which also contribute a lot to the valence band. While to the conduction band, the contribution is made by different orbitals such as 4d orbitals of molybdenum atoms, 2p-obitals of oxygen atoms, 2p-obitals of carbon atoms, and 2p-obitals of nitrogen atoms, respectively. When adding up the contribution from different atoms, we found that the atomic orbitals in MoO$_5$N octahedra dominate the conduction band and valence band.
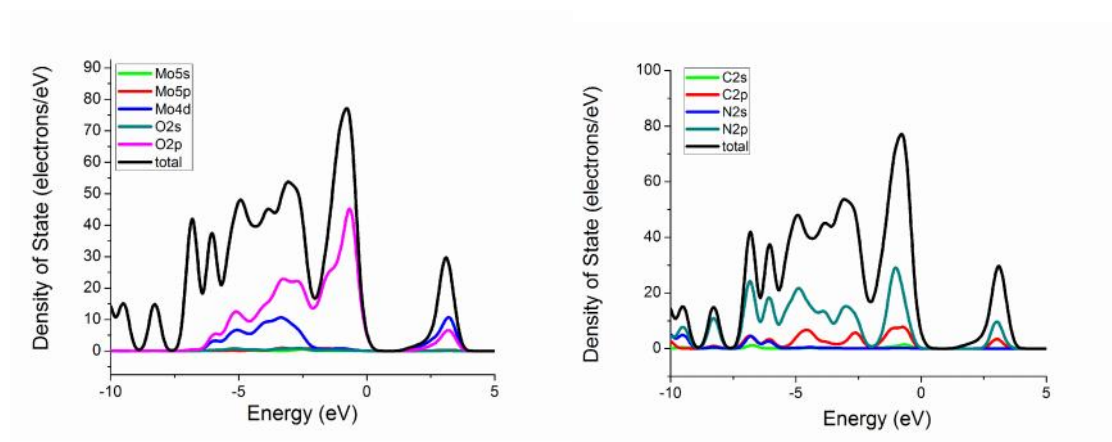
Figure 50: Density of states of inorganic part (left) and organic part (right) of 3D-MoO$_3$(*4,4'-bpy*)$_{0.5}$.

We also examined the density of states of 1D-MoO$_3$ (*4,4′-dm-2,2′-bpy*). Figure 50 shows the 2p-obitals of oxygen atoms in the inorganic layer contribute significantly more to the valence band compared to 2s-obitals and 2p-obitals of nitrogen atoms, which also contribute a certain ratio to the valence band. The conduction band are contributed by different orbitals such as 4d orbitals of molybdenum atoms, 2p-obitals of oxygen atoms, 2p-obitals of carbon atoms, and 2p-obitals of nitrogen atoms, respectively. When comparing the contribution ratios between different atoms, we found that the position of the conduction band is mainly determined by 2p-orbitals of carbon atoms, which may imply that the band gap value is determined by the inorganic chain and the organic ligands.
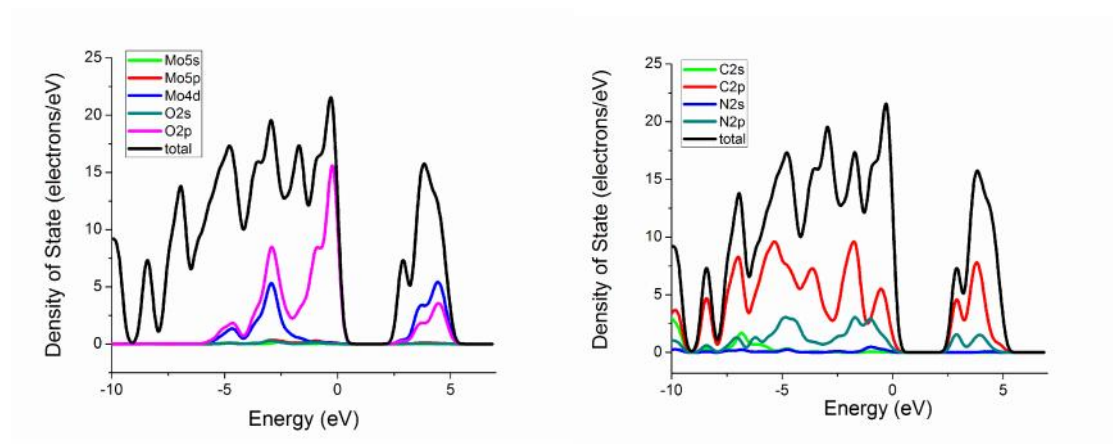
Figure 51: Density of states of inorganic part (left) and organic part (right) of 1D-MoO$_3$(*4,4′-dm-2,2′-bpy*)

Interesting optical absorption results are also found in $WO_3(L)$ organic- inorganic hybrid materials and shown in Figure 52. Compared to 2.6 eV of the band gap of WO_3, compounds **2**, **4**, **5**, **7** and **9** display band gap absorption in lower energy area from 2.2 eV of 3D-$WO_3(pyz)_{0.5}$, 2.25 eV of 3D-$WO_3(4,4'-bpy)_{0.5}$ to 2.3 eV of 3D-$WO_3 (bpe)_{0.5}$, which are 0.4 eV, 0.35eV and 0.3 eV less than 2.6 eV of WO_3 band gap. As the length of organic linkers increases, the band absorption edges of the three dimensional $WO_3(L)$ compounds slightly shifts to a higher energy. 2D-$WO_3(py)$ show absorption edge around 2.2 eV, yet the intensity is not as strong as its 3D and 1D brothers. 1D-$WO_3(2,2'-bpy)$, which starts to absorb light above 3.2 eV, not only displays a large blue shift of 0.6 eV, but also shows strong optical absorption ability as well.
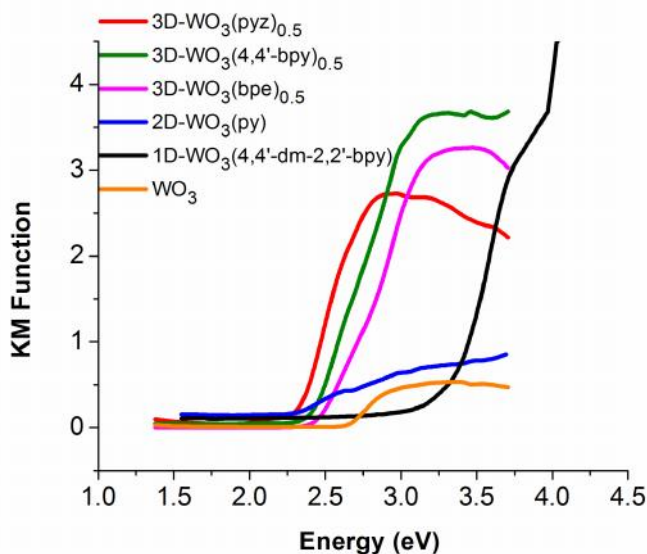
Figure 52: Optical absorption spectra of $WO_3(L)$ inorganic organic hybrid semiconductors and their parent WO_3.

3.3 Thermal stability of MO$_3$(L)

The thermogravimetric (TG) analyses of polycrystalline samples of both MoO$_3$(L) and WO$_3$(L) inorganic organic hybrid structures were performed on a computer-controlled TA Instrument TG Q50 analyzer. Single-phased powder samples were loaded into platinum pans and heated with a ramp rate of 5 °C/min from room temperature to 600 °C, and the results are summarized in Table 10. Figure 53 shows the good thermal stabilities for all the compounds and also single-step weight losses observed for 3D-MoO$_3$(*pyz*)$_{0.5}$ (**1**), 3D-MoO$_3$(*4,4′-bpy*)$_{0.5}$ (**3**), 2D-MoO$_3$(*py*) (**6**), 1D-MoO$_3$(*2,2′-dm-4,4′-bpy*) (**8**). As shown in the TG curves, all four compounds exhibit good thermal stability. The three dimensional compounds 3D-MoO$_3$(*pyz*)$_{0.5}$ (**1**) and 3D-MoO$_3$(*4,4′-bpy*)$_{0.5}$ (**3**) are most thermally stable since the decomposition of organic ligands in both materials start after 300°C, which is higher than 250 °C for 2D-MoO$_3$(*py*) (**6**) and 160°C for 1D-MoO$_3$(*2,2′-bpy*) (**8**) respectively. The measured weight losses of the organic species are 22% for pyrazine in **1**, 35% for 4,4′-bipyridine in **3**, 32% for pyridine in **6** and 52% for 2,2′-bipyridine in **8**, in reasonable agreement with the calculated values of 22% for pyrazine, 35% for 4,4′-bipyridine, 32% for pyridine, and 53% for 2,2′-bipyridine, respectively. Powder X-ray diffraction patterns shows the residues of all samples are nanoparticles of MoO$_3$ perovskite structures.
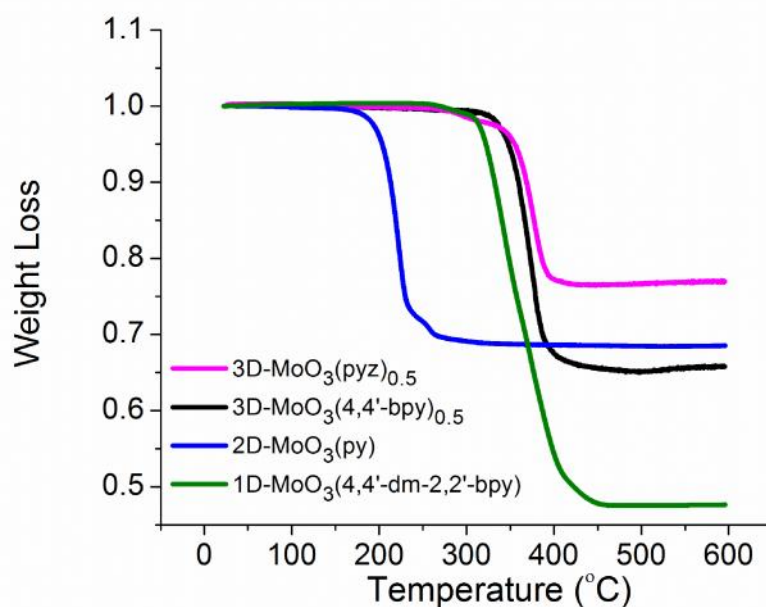
Figure 53: TGA profile of (a) MoO$_3$(L) inorganic organic hybrid materials.

Table 10: The calculated and experimental TGA weight loss of MoO$_3$ based inorganic organic hybrid structures.

Compound	WL % (calcd)	WL % (exptl)	T$_d$ (°C)	Residue
3D-MoO$_3$(pyz)$_{0.5}$ (**1**)	22	22	300	MoO$_3$ (p)
3D-MoO$_3$($4,4'$-bpy)$_{0.5}$ (**3**)	35	35	310	MoO$_3$(p)
2D-MoO$_3$(py) (**6**)	35	32	160	MoO$_3$(p)
1D-MoO$_3$($4,4'$-dm-$2,2'$-bpy) (**8**)	52	53	270	MoO$_3$(p)

Td: Temperature of decomposition.

Similar behavior was also observed in $WO_3(L)$ inorganic organic hybrid semiconductors, for compounds underwent one-step weight losses from room temperature to 650 °C (see Figure 54). As what we observed in $MoO_3(L)$ hybrid materials, $WO_3(L)$ also showed the thermal stability are dependent on the structures with a trend of three dimensional structures > one dimensional structures > two dimensional structures. To be specific, 3D structures 3D-$WO_3(pyz)_{0.5}$ (2), 3D-$WO_3(4,4'-bpy)_{0.5}$ (4) and 3D-WO_3 $(bpe)_{0.5}$ (5) showed the best thermal stability with onset temperature of 400°C. Particularly, $WO_3(pyz)_{0.5}$ did not decompose 520 °C as stable as many inorganic materials. 1D-$WO_3(2,2'-bpy)$ and 2D-$WO_3(py)$ were less thermally stable and decomposed at 320°C and 180°C, respectively. The TG weight loss for each compound matched with the mass ratio of its organic ligand. The experimental weight losses of the organic species are 15% for pyrazine in **2**, 24% for 4,4'-bipyridine in **4**, 27% for 1,2-Di-(4-bypiridyl)ethane in **5**, 24% for pyridine in **7** and 40% for 2,2'-bipyridine in **9**, respectively, in reasonable agreement with the calculated values of 14% for pyrazine, 25% for 4,4'-bipyridine, 28% for 1,2-Di-(4-bypiridyl)ethane, 20% for pyridine, and 41% for 2,2'-bipyridine respectively. The post-TGA residuals were found to be perovskite WO_3. Based on the TG results of both $MoO_3(L)$ and $WO_3(L)$ inorganic organic hybrid structures, we can confirm that all the reported reaction conditions can give pure phase hybrid materials with good thermal stability. The high thermal stability allow the $MoO_3(L)$ and $WO_3(L)$ hybrid structures to be annealed to make pallets and films for future research and application.
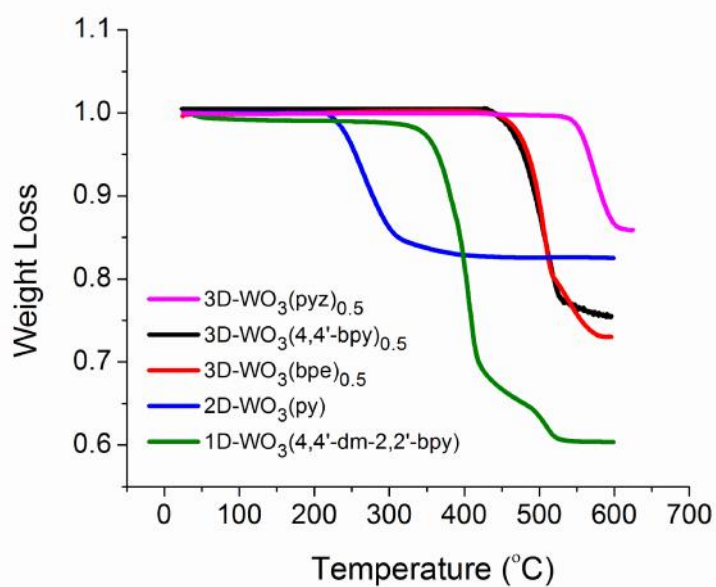
Figure 54: TGA profile of WO$_3$(*L*) inorganic organic hybrid materials.

Table 11: The calculated and experimental TGA weight loss of WO$_3$ based inorganic organic hybrid structures.

Compound	WL % (calcd)	WL % (exptl)	T$_d$ (°C)	Residue
3D-WO$_3$(*pyz*)$_{0.5}$ (**2**)	15	14	520	WO$_3$(p)
WO$_3$(*4,4′-bpy*)$_{0.5}$ (**4**)	24	25	400	WO$_3$(p)
3D-WO$_3$(*bpe*)$_{0.5}$·0.14 H$_2$O (**5**)	27	28	400	WO$_3$(p)
2D-WO$_3$(*py*) (**7**)	24	20	180	WO$_3$(p)
1D-WO$_3$(4,4′-dm-*2,2′-bpy)* (**9**)	40	41	320	WO$_3$(p)

Td: Temperature of decomposition.

3.4 Dielectric properties of MO$_3$(L)

One of the advantages of inorganic organic hybrid semiconductors is to introduce a number of interfaces between adjacent layers and the interfaces sometimes lead to unique properties. To explore the interface between inorganic and organic layers, we were trying to measure free dielectric constant and dielectric loss on selected inorganic organic hybrid materials. The as synthesized MoO$_3$(*4,4'-bpy*)$_{0.5}$, MoO$_3$(*py*), MoO$_3$ samples were grinded into fine powders and then compressed into pallets and further annealed at 275 ⁰C, 175 ⁰C and 600 ⁰C for dielectric measurements. The pallets were covered with silver paint and dried at room temperature. The free dielectric constant and dielectric loss were measured at 1 kHz by an impedance analyzer HP4194A. The results are shown in Figure 55. In the frequency range from 10KHz to 1MHz, both the MoO$_3$(*4,4'-bpy*)$_{0.5}$ and MoO$_3$(*py*) show higher dielectric constants than their parent structure MoO$_3$. Hybrid structures start with very high dielectric constants (1400 for MoO$_3$(*4,4'-bpy*)$_{0.5}$ and 350 for MoO$_3$(*py*)) and decrease dramatically before 100KHz, which is the evidence of space charge polarization in the hybrid structures, since the space charges vibrate most strongly when applied with low frequency alternating current (AC) electric field.[112] The space charge assumption is further proved by comparing their dielectric losses in Figure 55. At low frequency range, hybrid structures show higher dielectric loss and is negatively correlated with frequency, which is as result of the charge leakage when plenty of space charges accumulate on the structural boundaries.

The most important cause of space charge is the interfaces between electrically conducting grains and insulating grains. The MoO_3 (*L*) hybrid structures contain alternative electrically conducting MoO_3 inorganic layers and insulating organic layers, and the interfaces between them may cause the space charge polarization and then high dielectric constants and is of importance in semiconductor field-effect devices.
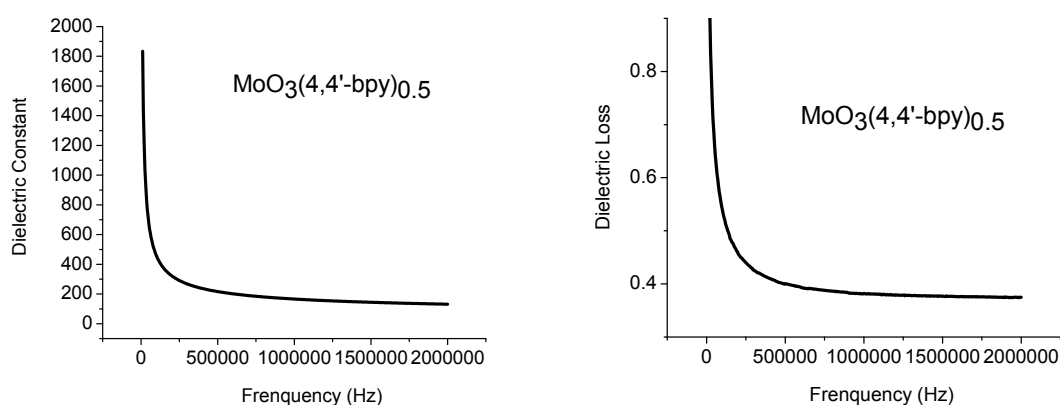
Figure 55: (left) Dielectric constants and (right) dielectric loss of 3D-MoO_3(*4,4′-bpy*)$_{0.5}$ at different frequencies.
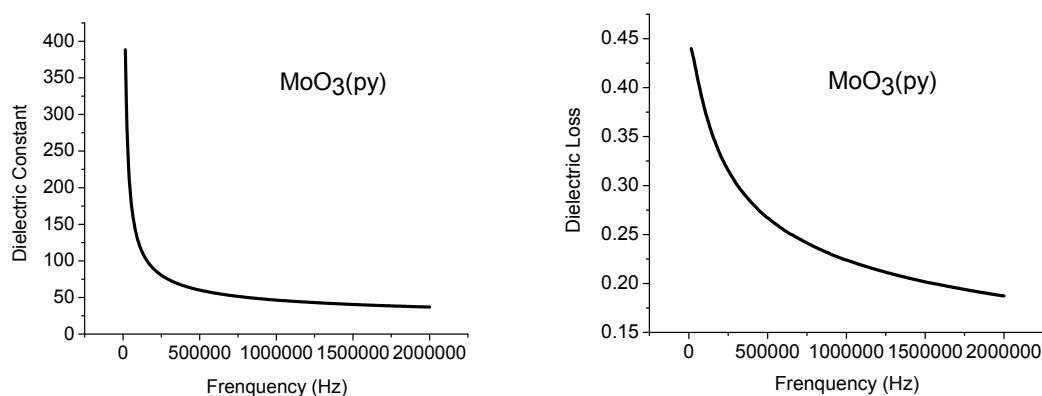
Figure 56: (left) Dielectric constants and (right) dielectric loss of 2D-MoO$_3$(*py*) at different frequencies.
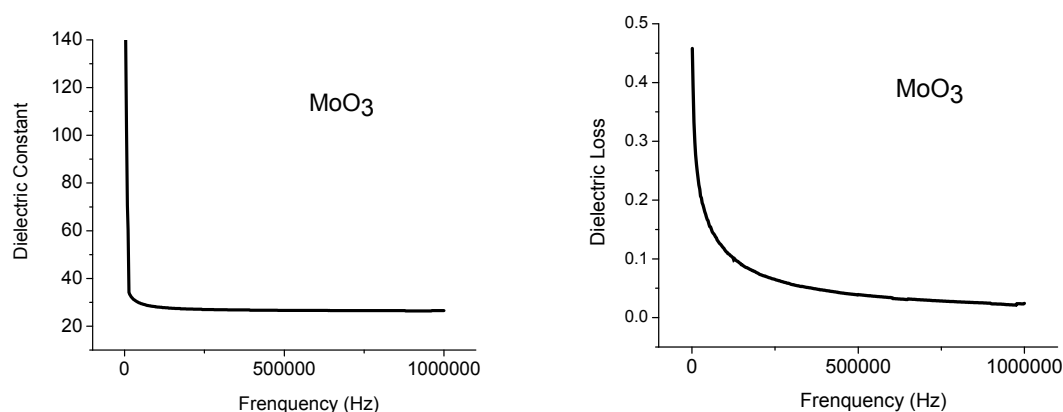
Figure 57: (left) Dielectric constants and (right) dielectric loss of MoO$_3$ at different frequencies.

To further study the relationship between free charges in the crystal structure and its dielectric properties, we prepared the MoO$_{2.5}$(OH)$_{0.5}$(*4,4′-bpy*)$_{0.5}$ with the reaction of Mo (0.03 g), MoO$_3$ (0.152 g), 4,4′-bipyridine (0.144 g), and H$_2$O (6 mL) in a 23 mL acid digestion bomb at 150 °C for 5 d. The product was washed by 30% ethanol and water followed by drying in anhydrous ethyl ether. The black crystals of **3** (70% highest yield based on MoO$_3$) were isolated.

Then samples were grinded into fine powders and then compressed into pallets and further annealed at 200 °C before the dielectric measurements. The dielectric

measurements were carried out in the same condition as of $MoO_3(4,4'-bpy)_{0.5}$ and the results show that the dielectric constants of $MoO_{2.5}(OH)_{0.5}(4,4'-bpy)_{0.5}$ can be as high as 1000, almost ten times higher than its similar structure, $MoO_3(4,4'-bpy)_{0.5}$. This difference is mainly caused by the free charge in $MoO_{2.5}(OH)_{0.5}(4,4'-bpy)_{0.5}$. The valence state of Mo is +5, with one electron in its d-orbital, while the Mo in $MoO_3(4,4'-bpy)_{0.5}$ is +6, with no electron staying in its d-orbital. The free charges in the crystal structure will largely flow under the external electric field until the later one is balanced by the self-generated internal electric field to obtain electrostatic equilibrium, which causes the extremely high dielectric constant. This can be further confirmed by the high dielectric loss of $MoO_{2.5}(OH)_{0.5}(4,4'-bpy)_{0.5}$ compound. The free-moving electrons will accumulate on the sample surface and cause the leakage under the external electric field, leading to the high dielectric loss as shown in the Figure 58.
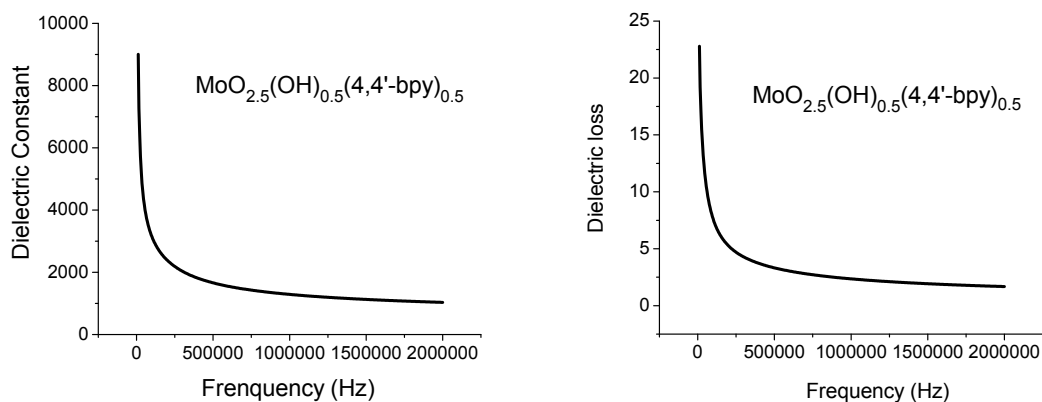
Figure 58: (left) Dielectric constants and (right) dielectric loss of $MoO_{2.5}(OH)_{0.5}(4,4'-bpy)_{0.5}$ at different frequencies.

3.5 Thermoelectric properties of MO$_3$(L)

The thermal conductivity (TC) of selected MoO$_3$(*4,4′-bpy*)$_{0.5}$ and WO$_3$(*4,4′-bpy*)$_{0.5}$ samples on behalf of MoO$_3$(*L*) and WO$_3$(*L*) series were determined by the density, specific heat capacity, and thermal diffusivity.

The thermal conductivity can be calculated by the following equation: k(T) = a(T) · Cp(T) · d(T)

k is the thermal conductivity of the sample, in [W·m^{-1}·K^{-1}],

a is the thermal diffusivity of the sample, in [m^2 ·s^{-1}],

Cp is the specific heat of the sample, in [J·kg^{-1}·K^{-1}]

d is the density of the sample, in [kg·m^{-3}].

The results of the thermal conductivity measurements are shown in Figure 59. Both the MoO$_3$(*4,4′-bpy*)$_{0.5}$ and WO$_3$(*4,4′-bpy*)$_{0.5}$ samples have thermal conductivity ~ 0.3 W*m/K at 101°C, about 80% less than ~1.5 W*m/K for both MoO$_3$ and WO$_3$ samples prepared by cold-pressing process. Over a temperature range from 25°C to 101°C, the thermal conductivity of MoO$_3$ and WO$_3$ decrease all the way as the temperature increase. Unlike the trend observed in inorganic oxides, MoO$_3$(*4,4′-bpy*)$_{0.5}$ and WO$_3$(*4,4′-bpy*)$_{0.5}$ keep the TC almost unchanged. The thermal conductivity of MoO$_3$(*4,4′-bpy*)$_{0.5}$ is a little higher than WO$_3$(*4,4′-bpy*)$_{0.5}$, which is similar to their parent structure, for the TC of MoO$_3$ is also a little higher than WO$_3$.
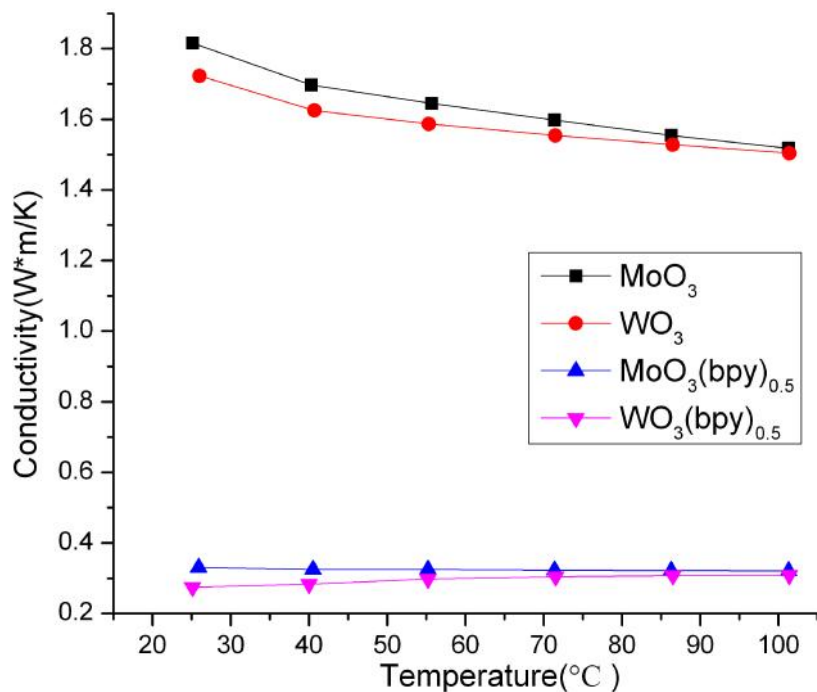
Figure 59: Thermal conductivities of compounds MoO$_3$ (■), WO$_3$ (●), MoO$_3$(4,4′-bpy)$_{0.5}$ (▲) and WO$_3$(4,4′-bpy)$_{0.5}$ (▼).

The cause of low thermal conductivity of hybrid structures can be understood by a closer look at the three parameters that determine thermal conductivity. Thermal diffusivity of the selected hybrid materials and their parent structures are plotted in Figure 60. When the inorganic layers are separately by organic molecules, the resulted interfaces at atomic scale can increase phonon scattering. As the phonon scattering enhanced, a large amount of the heat (phonons) dissipate during the movement and cause thermal diffusivity to be reduced. This mechanism results in the difference as shown in Figure 60. Over a temperature range from 25 °C to 101 °C, the thermal diffusivity of MoO$_3$(4,4′-bpy)$_{0.5}$ and WO$_3$(4,4′-bpy)$_{0.5}$ stays lower than one fourth

compared to their parent structures, mainly contributing to the low thermal conductivity of hybrid materials.
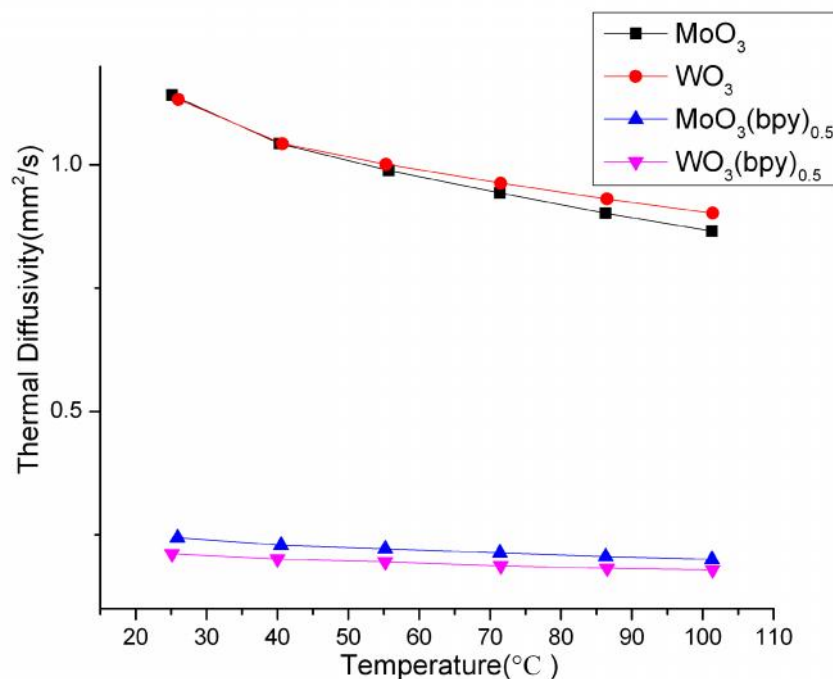
Figure 60: thermal diffusivities of compounds MoO_3 (■), WO_3 (●), $MoO_3(4,4'$-$bpy)_{0.5}$ (▲), $WO_3(4,4'$-$bpy)_{0.5}$ (▼).

Heat capacity (HC) of the selected $MO_3(L)$ structures is slightly higher than their parent structure, for the HC of $MoO_3(4,4'$-$bpy)_{0.5}$ (~ 0.75 $J \cdot kg^{-1} \cdot K^{-1}$) and $WO_3(4,4'$-$bpy)_{0.5}$ (~ 0.60 $J \cdot kg^{-1} \cdot K^{-1}$) are about 1.3 and 1.8 times of the HC of WO_3 (0.53 $J \cdot kg^{-1} \cdot K^{-1}$) and MoO_3 (0.33 $J \cdot kg^{-1} \cdot K^{-1}$). In all four compounds, the heat capacity is positively correlated with the temperature. The increase in heat capacity is offset by the lower density of inorganic organic hybrid structures.
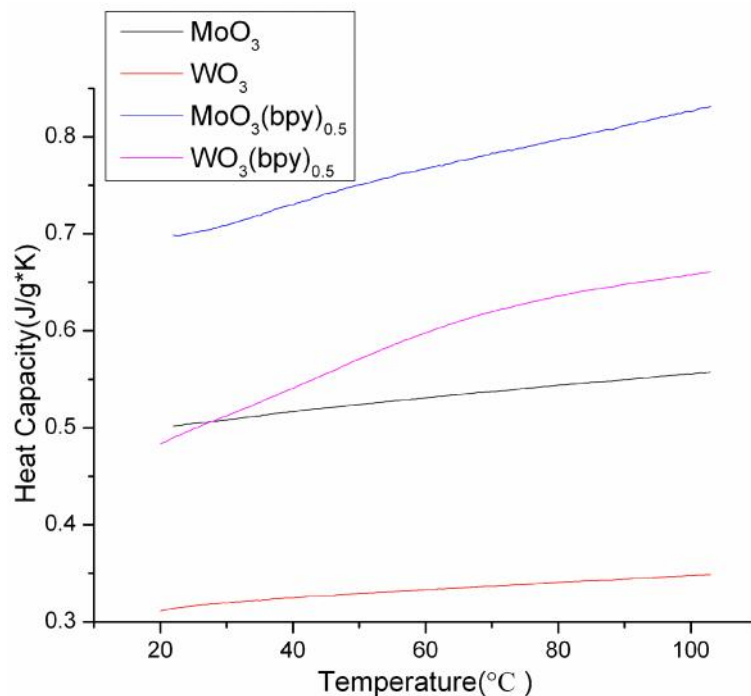
Figure 61: Heat capacities of compounds MoO₃ (black), WO₃ (red), MoO₃(4,4'-bpy)₀.₅ (blue) and WO₃(4,4'-bpy)₀.₅ (purple).

The density of the pallet-form samples are measured by dividing the masses by the volumes and the results are comparable with the unit cell density presented in Table 12. All four cases show that the experimental densities are lower than unit cell densities due to the space between packing particles, but the trend of experimental density data, (4.79 g/cm³ for WO₃ > 3.15 g/cm³ for MoO₃ > 2.61 g/cm³ for WO₃(4,4'-bpy)₀.₅ > 1.94 g/cm³) for MoO₃(4,4'-bpy)₀.₅ is consistent to the trend of unit cell density data (7.16 g/cm³ for WO₃ > 4.69 g/cm³ for MoO₃ > 3.30 g/cm³ for WO₃(4,4'-bpy)₀.₅ > 2.26 g/cm³ for MoO₃(4,4'-bpy)₀.₅) and the experimental densities of MoO₃(4,4'-bpy)₀.₅ and WO₃(4,4'-bpy)₀.₅ show

~30% and ~40% less than the densities of inorganic oxides which is another reason for low thermal conductivity of the hybrid materials.

Table 12: The experimental density and unit cell density of selected $MO_3(L)$ hybrid structures and their parent structures.

Compounds	Experimental density g/cm³	Calculated density g/cm³
MoO_3	3.15	4.69
WO_3	4.79	7.16
$MoO_3(4,4\text{-bpy})_{0.5}$	1.94	2.36
$WO_3(4,4\text{-bpy})_{0.5}$	2.61	3.30

In summary, the apparent decreases in thermal conductivity and density, together with a tender increase in heat capacity result in the low thermal conductivity of $MoO_3(4,4'\text{-bpy})_{0.5}$ and $WO_3(4,4'\text{-bpy})_{0.5}$ inorganic organic hybrid materials with almost one order less TC coefficient than their parent MoO_3 and WO_3 structure.

3.6 Thermal expansion properties of MO₃(L)

3.6.1 MoO₃(4,4′-bpy)₀.₅

Negative thermal expansion (NTE) and nearly zero thermal expansion (ZTE) behaviors were found in our II-VI inorganic organic hybrid structures as discussed in chapter 1. To explore whether the VI-VI hybrid system also show similar thermal expansion behavior, we collected X-ray diffraction patterns of MoO₃(4,4′-bpy)₀.₅ at a number of temperatures between 28 °C and 265 °C.

The unit cell parameters of MoO₃(4,4′-bpy)₀.₅ at each temperature was well defined based on Pawley refinement. Figure 62 shows the simulated MoO₃(4,4′-bpy)₀.₅ pattern at 28 °C matched pretty well with the experimental data, and the Goof value and Rwp vale are ~ 1.45 and 0.0146 respectively, indicating the good refinement results and reliability of the refined unit cell parameters.
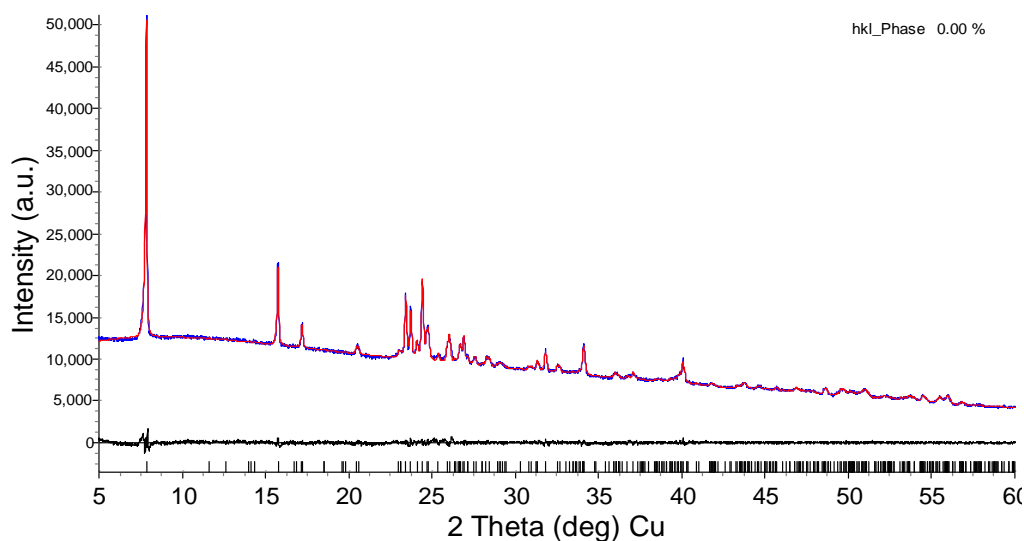
Figure 62: The experimental and simulated $MoO_3(4,4'\text{-}bpy)_{0.5}$ patterns at 28°C, and the differences between two patterns.

The temperature dependent lattice parameters a, b, c and β are plotted in Figure 63. According to the results, the b-axis shows very interesting negative thermal expansion behavior in the whole temperature range and the thermal expansion (TE) coefficient can be as large as $-1.5 \times 10^{-5}\,K^{-1}$, among the largest NTE values reported to date.
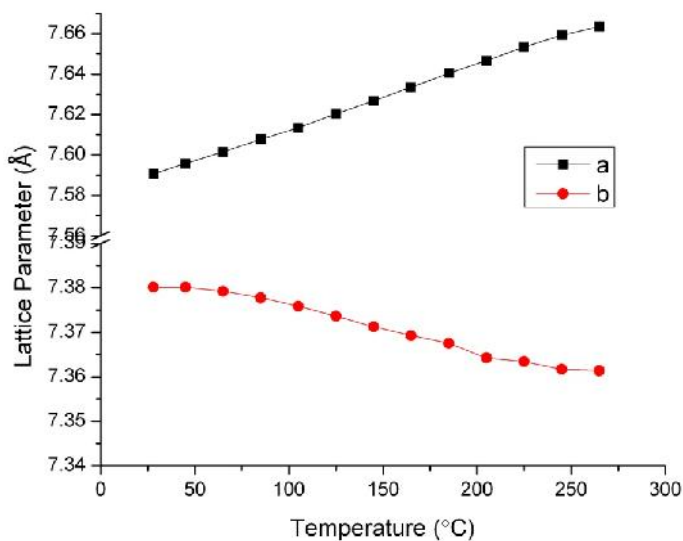
Figure 63: Temperature dependent lattice parameters of $MoO_3(4,4'\text{-}bpy)_{0.5}$ in a-axis and b-axis.
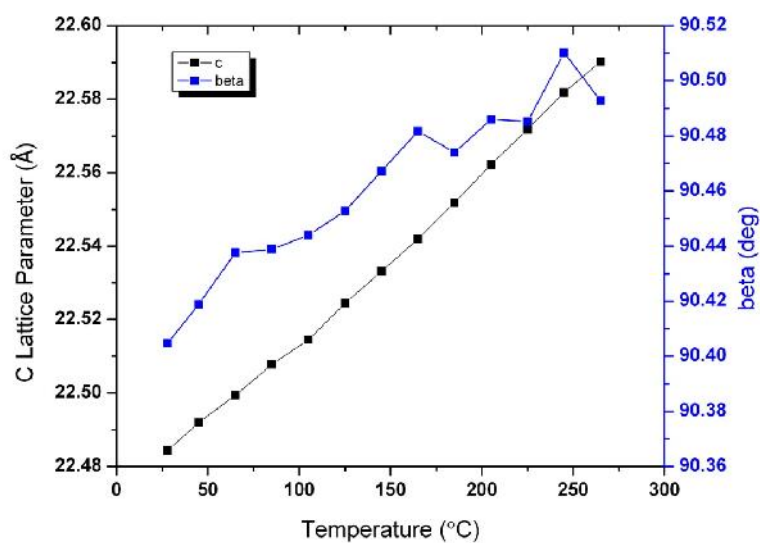
Figure 64: Temperature dependent lattice parameters of MoO₃($4,4'$-bpy)₀.₅ in a-axis and β-

angle.
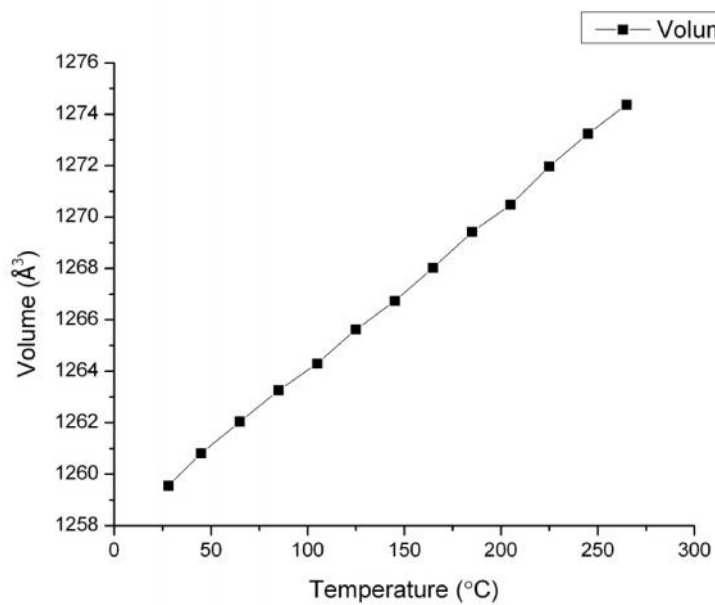
Figure 65: Temperature dependent volume of MoO₃($4,4'$-bpy)₀.₅.

Unlike the NTE behavior observed in the c-axis (long axis) in II-VI hybrid structures where the inorganic layers and organic layers packed, the b-axis (short axis) show NTE in $MoO_3(4,4'-bpy)_{0.5}$ structure. This is interesting because similar anisotropic NTE behavior was also observed in the b-axis of 2D-MoO_3 layered structure, and the later one has -0.3×10^{-5} K^{-1} of its TE coefficient. By comparing the structures between inorganic layer of $MoO_3(4,4'-bpy)_{0.5}$ and the layer of α-MoO_3 structure, we found many similarities between their bond distances, angles and symmetries. (see Figure 66). These similarities may help to explain their similar negative thermal expansion behavior due to the possibly similar phase transition or thermal motion of atoms.
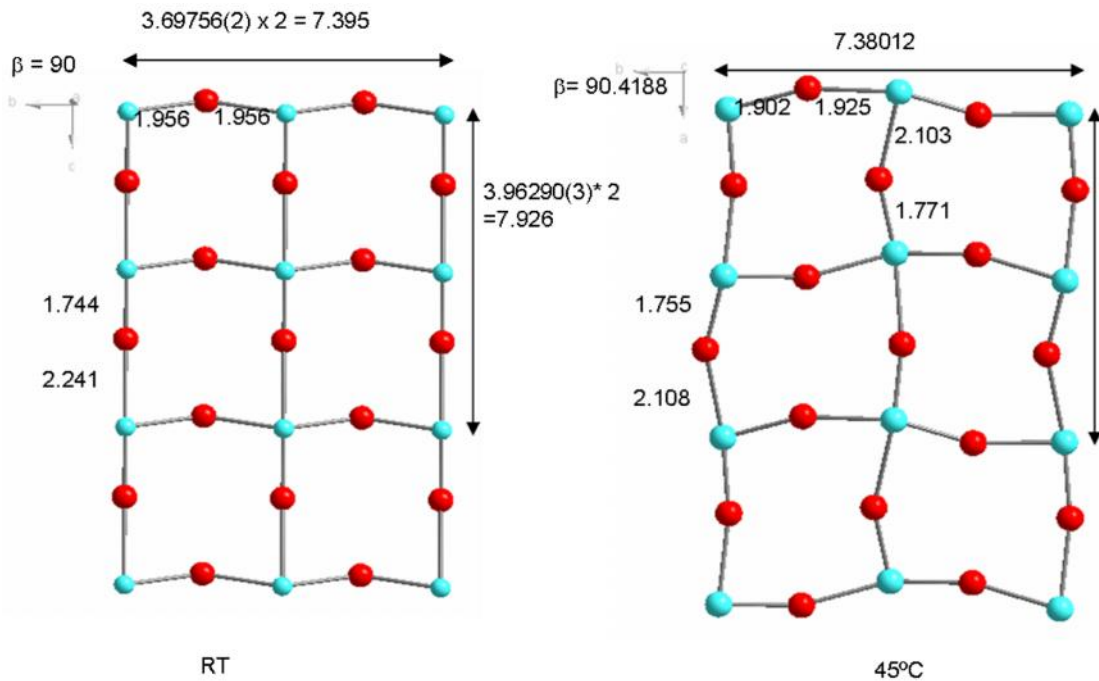
Figure 66: Structural comparison between 2D-MoO$_3$ (left) and MoO$_3$($4,4'$-bpy)$_{0.5}$(right).

3.6.2 WO$_3$(*4,4'-bpy*)$_{0.5}$

Negative thermal expansion (NTE) behavior was also found in WO$_3$($4,4'$-bpy)$_{0.5}$. We collected x-ray diffraction patterns of WO$_3$($4,4'$-bpy)$_{0.5}$ at a number of temperatures between -200 °C and 225 °C. The unit cell parameters of WO$_3$($4,4'$-bpy)$_{0.5}$ at different temperatures were also determined by Pawley refinement. The temperature dependent lattice parameters a, b, c and V are plotted in Figure 67. According to the results, the a-axis (short axis) shows interesting negative thermal expansion behavior in the temperature range between -150 °C and 225 °C and the thermal expansion (TE) coefficient can be as large as -1.7 ×10^{-5} K^{-1}.
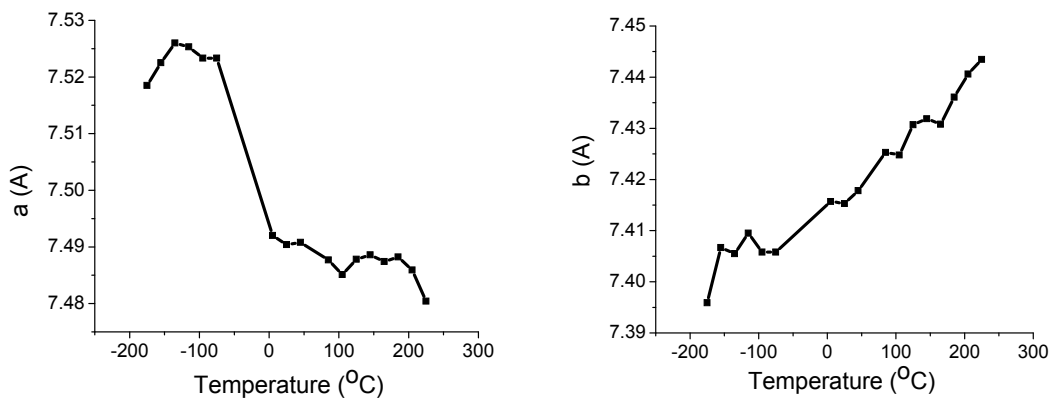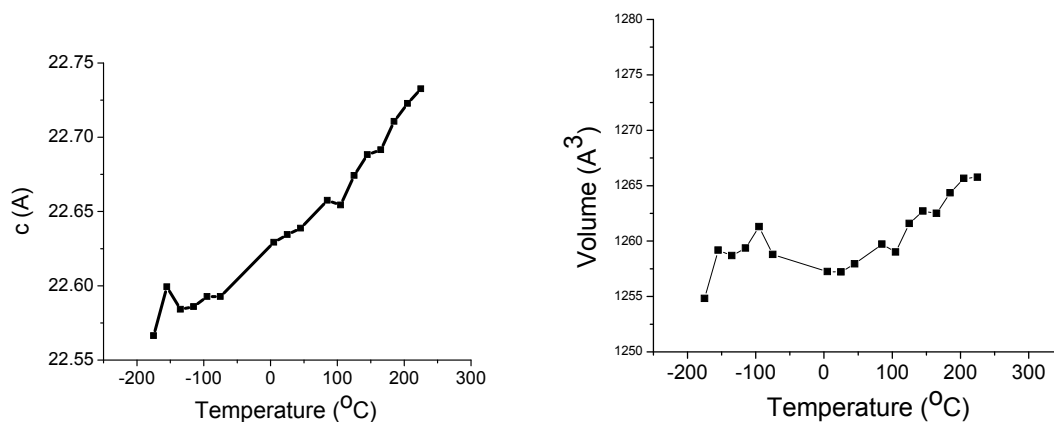
Figure 67: Temperature dependent lattice parameters of a, b, c and volume of MoO$_3$(*4,4'-bpy*)$_{0.5}$.

3.6.3 WO$_3$(*pyz*)$_{0.5}$

We also collected X-ray diffraction patterns and solve the structures of WO$_3$(*pyz*)$_{0.5}$ at a number of temperatures between -43 °C and 275 °C. The temperature dependent lattice parameters a, c and V are plotted in Figure 68 and Figure 69. According to the results, the compound WO$_3$(*pyz*)$_{0.5}$ exhibits the positive thermal expansion over the whole temperature range.
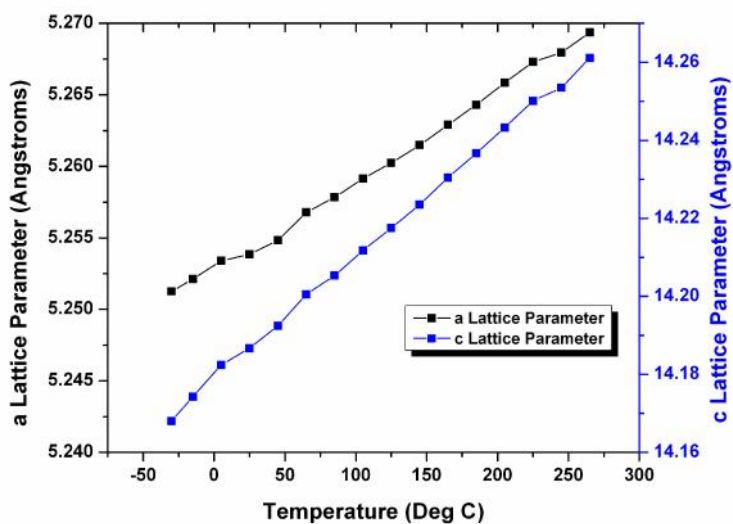
Figure 68: Temperature dependent lattice parameters of a, c and volume of WO$_3$(pyz)$_{0.5}$.
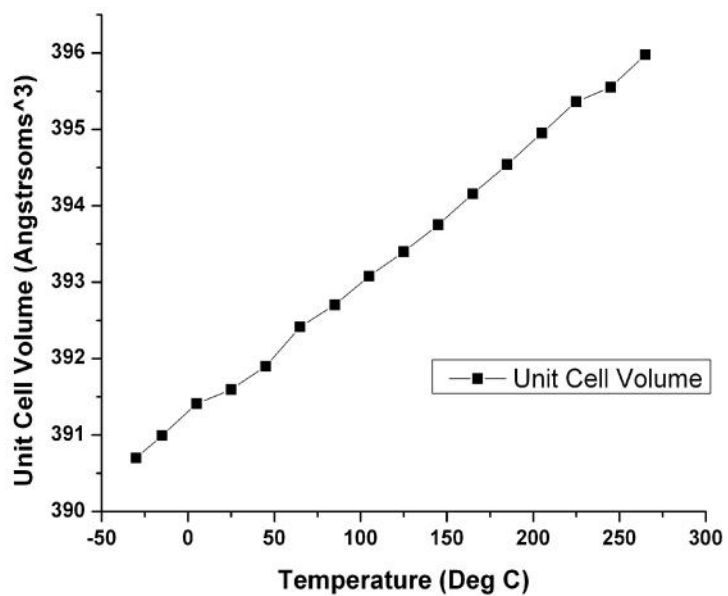
Figure 69: Temperature dependent volume of WO$_3$(pyz)$_{0.5}$.

A closer look at details of the powder x-ray diffraction shows the interesting phase transition between -175 °C to -30 °C. As shown in the Figure 70 and Figure 71. As the temperature decreases from -30 °C to -175 °C, both the single peaks at 23.8° corresponding to (110) plane and the single peak at 26.9° corresponding to (112) plane are separated into two peaks. This phenomenon is probably caused by the structural change from higher symmetry to lower symmetry since the later one is always preferred in low temperature.
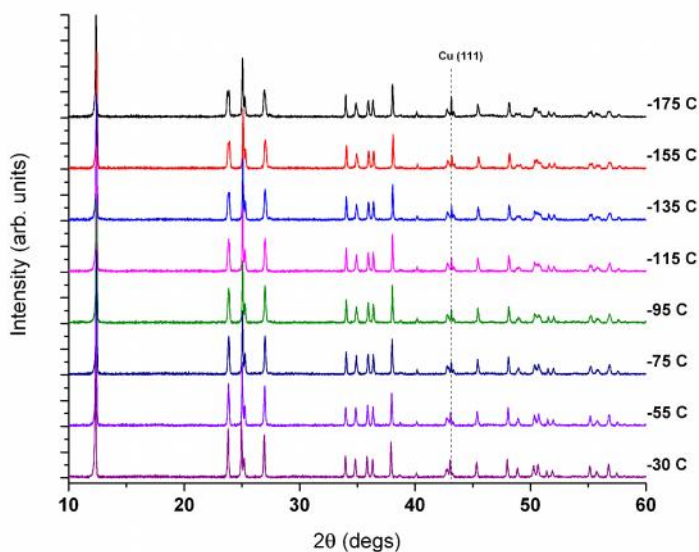
Figure 70: Background subtracted XRD patterns of $WO_3(pyz)_{0.5}$ from -30 °C to -175 °C.
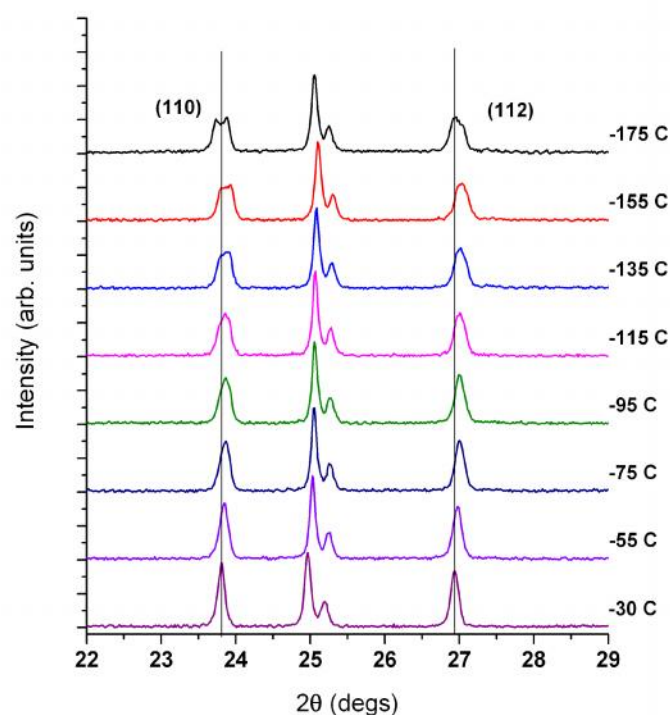
Figure 71: Background subtracted XRD patterns of WO$_3$(*pyz*)$_{0.5}$ from -30 °C to -175 °C for two theta values between 22° and 29°.

3.7 Summary

In summary, we have designed a new class of inorganic organic hybrid semiconductors with one-dimensional, two-dimensional and three-dimensional periodically ordered nanostructures with chainlike and layered inorganic VI-VI structural motifs under mild solvothermal conditions. By controlling the dimensionality and topology of the VI-VI inorganic component using organic spacers, hybrid semiconductors with tunable optical properties can be effectively designed and fabricated to meet the specific needs in device applications. Benefited from the good

thermal stability of new hybrid structures, we are able to study a series of physical properties such as thermoelectric, dielectric and thermal expansion properties which require high-temperature sample treatment. In these property studies, our VI-VI hybrid structures display desired and significantly low thermal conductivities and high dielectric constants caused by interface induced phonon scattering and space charge polarization respectively, while negative thermal expansions is related to the similar structural features between inorganic layer of $MoO_3(4,4'-bpy)_{0.5}$ and the 2D-MoO_3 layered structure. The interesting properties generated by the unique inorganic organic hybrid structures open a new and promising approach to multifunctional materials in advanced technology.

4. I-VII inorganic organic hybrid semiconductors

Concerns about global warming have led to a worldwide effort in the science community to reduce greenhouse gas emissions and to increase energy efficiency. Conservation of energy through gradual diversion of resources to renewable green energy paves the way for tomorrow's consumption and a cleaner environment. Solid-state lighting (SSL) technology in the form of light-emitting diodes (LEDs) generates high-efficient light sources, converts electricity into light up to 25% more effectively than conventional lighting sources.[113] The U.S. Department of Energy has estimated that switching to LED lighting over the next two decades could save the country $250 billion in energy costs over that period; this reduces the electricity consumption for lighting by nearly one half, and avoid 1,800 million metric tons of carbon emission. Low-cost and high-efficiency white light-emitting diodes or WLEDs (144 lm/W) are considered a potential light source to replace conventional incandescent (15 lm/W) or fluorescent lighting (114 lm/W) prevalent in major infrastructures.[12] Other applications in everyday lives range from computer displays to car headlights. However, major setbacks of SSL are the cost of using RE (rare-earth) elements and its lack of recyclability, which is destructive to the environment. Today, the purchase price of WLED lighting products is significantly higher than that of their conventional counterparts, and the energy savings often are not enough to offset the difference within an attractive payback period. Common approaches to produce WLEDs include blending of three primary colored

LEDs, namely red, green, and blue (RGB) diodes, or combination of a blue (or UV) LED with a yellow phosphor (or multiphosphors). Either process requires complex doping/mixing and delicate control of multiple materials and colors, which proves both challenging and costly.[114-117] At the present time, commercially available WLEDs are predominantly phosphor based (e.g. a yellow-emitting phosphor, yttrium aluminum garnet or (YAG):Ce3+, coupled with a blue-emitting InGaN/GaN diode).[118] While less expensive than the RGB diodes, the $(YAG):Ce^{3+}$ type phosphors and WLEDs have issues such as unsuitability for solution process, poor color rendering index (CRI), high correlated color temperature (CCT) and dependence on rare earth component which then limits their widespread commercialization in general lighting market. Developing new white phosphors that are energy efficient while also cost effective and, REs free, is of great interest worldwide.[117,119]

A good candidate for white phosphors of this type is CuI based hybrid materials. These materials are built on environmentally friendly CuI which has sharp emission between 400 nm to 450 nm and organic ligands such as 2,6-dimethylpyrazine, which can emits at in the UV range. When integrating the inorganic modules and organic ligands into the single crystal structure with coordination bond between the copper ions and nitrogen atoms, interesting yellow fluorescence is obtained, very different from both of its components. Our preliminary studies show that the emission of CuI(2,6 dimethylpyrazine) is primarily a band gap emission, namely, electrons are first excited

to the conduction band upon irradiation, then relaxed to the valence band, giving the emission in the visible light region. A closer look at the DFT calculation results reveals that the valence band of the compound mainly consists of the 3d orbitals of copper and the 5p orbitals of iodide, while the conduction band is mainly made of the 2p orbitals of carbon and nitrogen atoms. This result suggests the band gap emission involves a charge transfer from the organic molecules to the CuI inorganic orbitals. Based on this observation, by changing the functional group (electron donating or electron withdrawing group) on the organic molecules, the LUMO energy of the organic molecules, and thereby the conduction band of the hybrid structures, can be systematically tuned. The strong tunability of the band structure may lead to white light emission. The application of copper iodide complexes in OLEDs has recently been demonstrated that codeposition of CuI and 3,5-bis(carbazol-9-yl)pyridine (mCPy) is an efficient way to utilize CuI complexes as emissive materials in OLEDs.[120] Devices made using CuI:mCPy films shows pure green electroluminescence (EL) from a Cu(I) emitting species.
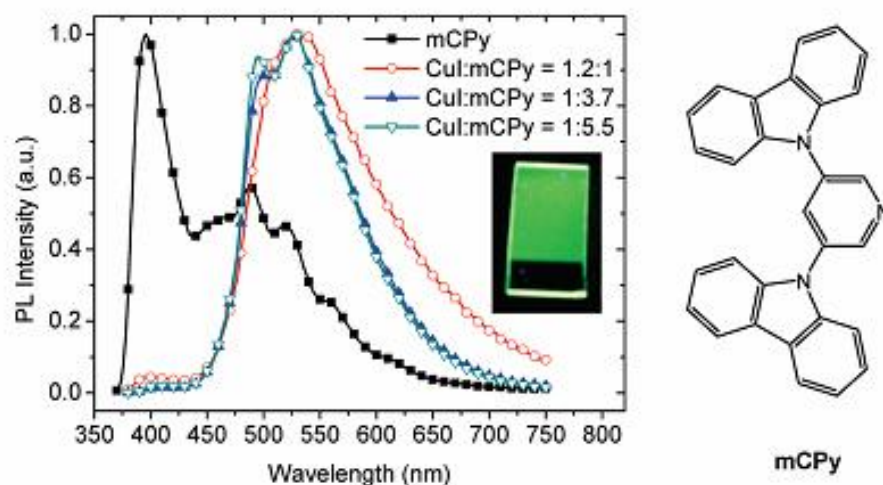
Figure 72[120]: (left) PL spectra (λex = 350 nm) of a neat mCPy film at 77 K and CuI:mCPy films at rt. Inset: photo of a CuI:mCPy film under UV light (365 nm). (right) Chemical structure of mCPy. (Reproduced with permission from ref 120. Copyright © 2012 American Chemical Society.)

Though the electroluminescence behavior is attractive, the green light emission OLED is still needed to be processed in conjunction with red and blue (RGB) diodes to produce WLEDs. As discussed above, this process requires complex doping/mixing and delicate control of multiple materials and colors, which proves both challenging and costly.

In this chapter, we report the synthesis of a series of hybrid structures containing CuI 1D chain and various organic linkers. These compounds can emit light with different color under UV lamp. Especially, the emission of the CuI(5-bromopyrimidine) and CuI(4-bromopyridine) crystals cover most of visible light area (from 400 nm to 700

nm), with CIE coordinates of (0.26, 0.35) and (0.36, 0.41), respectively. These results indicate the emission color is within white light area. In order to further increase the emission coverage of our hybrid materials, we have synthesized the CuI(L) hybrid structures with mixed organic ligands. To be specific, during the crystallization process of CuI(pyridine), a small amount of pyrimidine was added to the solution. Although the resulting crystals still adapts the structure of CuI(*pyridin*e) confirmed by the x-ray diffraction results, the emission range of the single crystals strongly changes and differs from CuI(*pyridine*) and CuI(*pyrimidine*) (see Figure 74). The emission of these uniform colorless single crystals covers the whole visible light area, with CIE coordinates of (0.31, 0.33), right on the pure white light spot. This result has opened a new way of designing WLED based on semiconducting bulk structures.
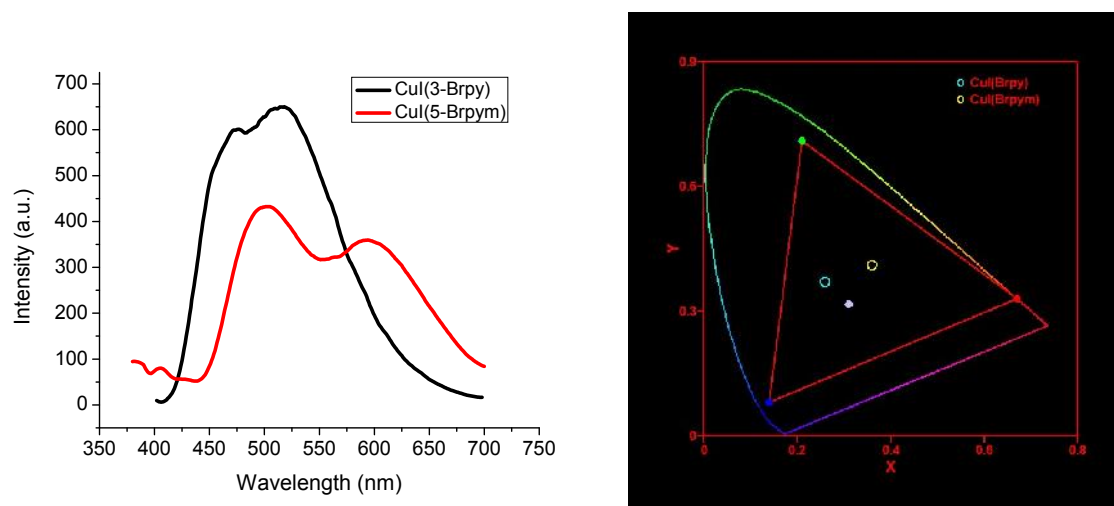
Figure 73: The PL spectra (left) and CIE coordinates (right) of CuI(*3-bromopyridine*) (black curve and light blue circle) and CuI(5-*bromopyrimidine*) (red curve and light yellow circle).
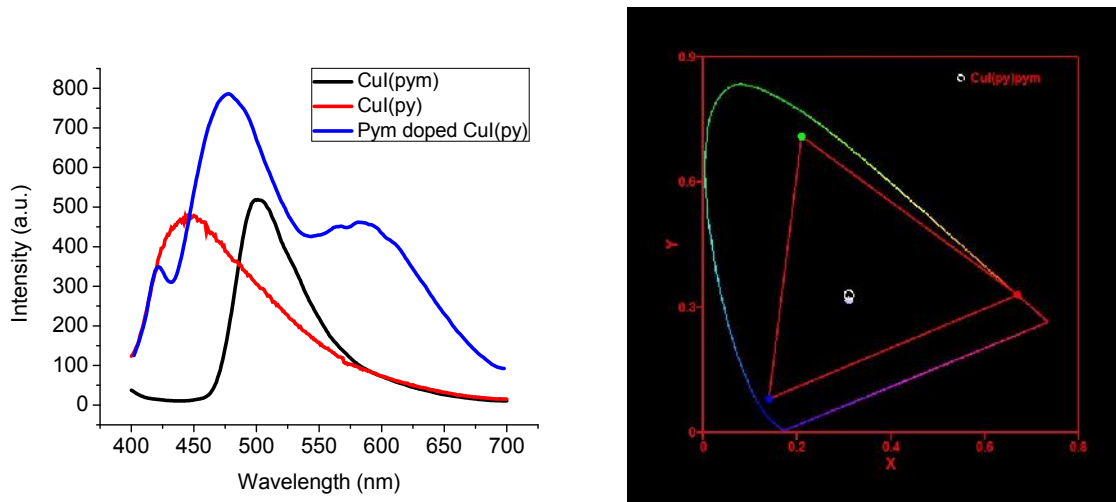
Figure 74: Left: The PL spectra of CuI(*pyridine*)$_x$(*pyrimidine*)$_{1-x}$ (blue), CuI(*pyridine*) (red)

and CuI(*pyrimidine*) (black). Right: CIE (coordinates) (right)of pyrimidine CuI(*pyridine*).

4.1 CuI(L) (L = organic ligand) structures

4.1.1 CuI(*L*) (*L = organic ligand*) structures based on s-CuI

4.1.1.1 3D-Cu₂I₂(*1,3,5-triazine*)

Synthesis of 3D-Cu₂I₂(*1,3,5-triazine*) (**1**): A solution of CuI (0.020 g; 1.05×10^{-4} mol) in acetonitrile (10 mL) was added to a solution of 1,3,5-triazine (0.0043 g; 0.53×10^{-4} mol) in dichloromethane (10 mL). The mixture was left at room temperature overnight and the resulting yellow precipitate collected after filtration, washed with dichloromethane and dried in vacuum.

1 is composed of single layer copper iodide sheets linked by 1,3,5-triazine molecules acting as bidentate bridging ligands. Each asymmetric unit of the structure contains one copper cation, one iodide anion, and half a 1,3,5-triazine molecule. The CuI layer consists of both three-coordinated copper and iodine atoms which form the honeycomb structure with six-membered rings, which is exactly same as the layer in wurzite CuI structure. The fourth position of the tetrahedral copper center in 3D-Cu₂I₂(*1,3,5-triazine*)$_{0.5}$ is occupied by a nitrogen of a 1,3,5-triazine which bridges to a copper atom in a second CuI layer giving the alternating copper iodide and 1,3,5-triazine layers (see Figure 75).
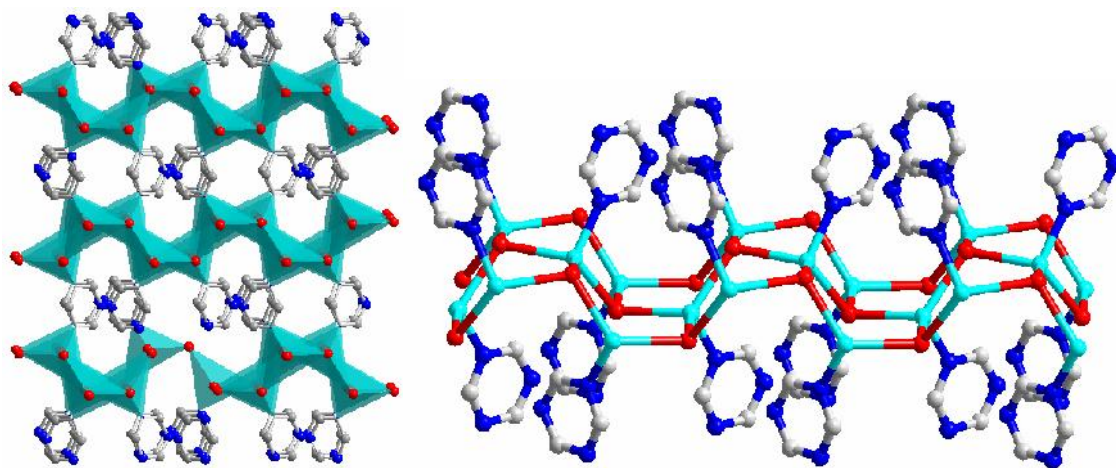
Figure 75: Crystal structures of CuI(*1,3,5-triazine*)0.5 (Cu: green; I: red; N: blue; C: grey).

X-ray diffraction studies of the as-prepared 3D-CuI(*1,3,5-triazine)*0.5 samples indicate the pure phase of the product and high crystallinity. The TG analysis was performed under N_2 protection with a heating rate of 10 $^{\circ}$C/min in the temperature range 25–450 C. The TG curve of **1** shows that it is thermally stable up to 120 $^{\circ}$C. Above this temperature, the structure decomposes and only CuI remains. The remaining weight (84%) is close to the percentage of CuI in the hybrid stucture. (see Figure 76)

Figure 76: Up: Comparison between experimental and simulated pattern of 3D-CuI(*1,3,5-triazine*)0.5. Down: TGA profile of CuI(*1,3,5-triazine*)0.5.

4.1.2 CuI(*L*) (*L* = *organic ligand*) structures based on x-CuI

4.1.2.1 1D-CuI(*2,6-dimethylpyrazine*)

Synthesis of 1D-CuI(*2,6-dimethylpyrazine*) (**2**): A solution of CuI (0.190 g; 1mmol) in saturated potassium iodide solution (2 mL) was added with a solution of 2,6-dimethylpyrazine (0.108 g; 1mmol) in acetone (2 mL). Acetonitrile (2m) was used as interlayer between the above two solutions to help crystal growth. The mixture was left at room temperature overnight and the resulting yellow crystals were collected after filtration.

In the crystal structure of **2**, all Cu(I) atoms in the Cu2I2 ribbon are 3-fold coordinated to I, and all I atoms bridge to three copper metal centers giving Cu-I distances varying from 2.6320(7) to 2.6530(6) Å. The Cu_2I_2 ribbon has same atomic ratio, valence state and coordination type as its parent rock salt CuI structure. Each 2,6-dimethylpyrazine binds to one copper atoms via its N sites which completes the fourth coordination of Cu(I) with a stable and preferred tetrahedral geometry.
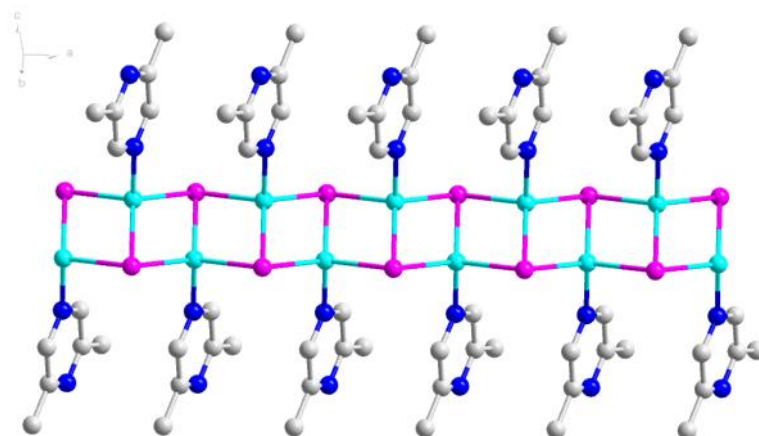
Figure 77: Crystal structure of CuI(*2,6-dimethylpyrazine*). (Cu: light blue; I: purple; N: blue; C: grey)

Comparison between experimental and simulated X-ray diffraction patterns 3D-CuI(*2,6-dimethylpyrazine)* indicates the pure phase and high crystallinity of the product. The TG analysis was performed in N_2 atmosphere with a heating rate of 10 °C/min in the temperature range 25–450 °C. The TG curve of **2** shows that it is thermally stable up to 100 °C. Above this temperature, the structure decomposes and only CuI remains. The remaining weight (63%) is close to the percentage of CuI.
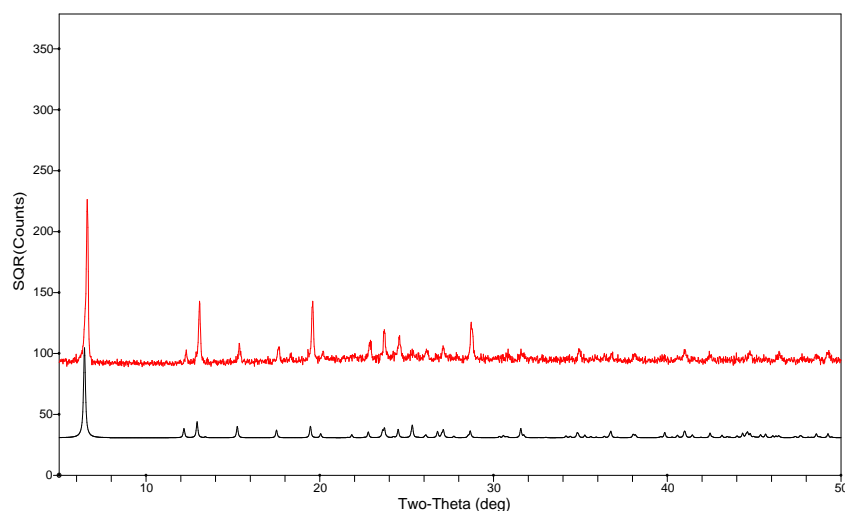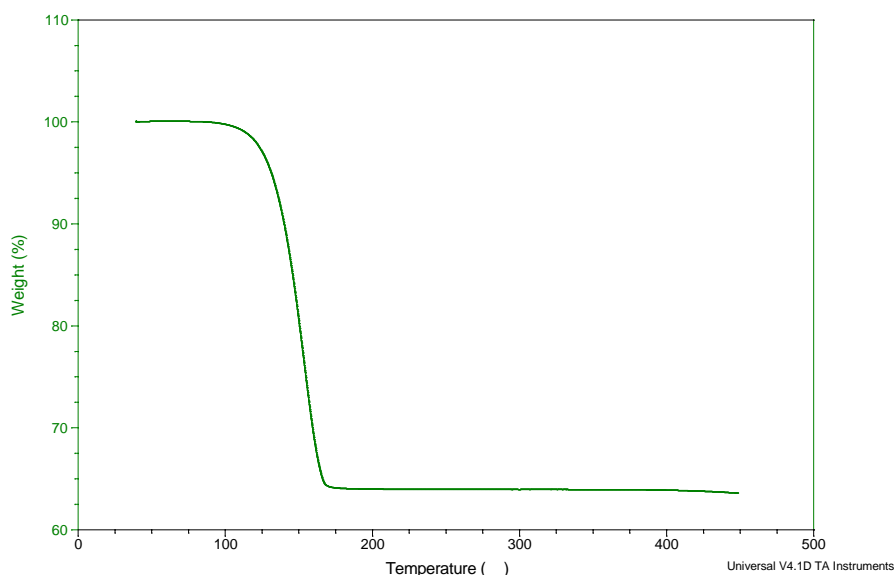
Figure 78: Top: Comparison between experimental and simulated XRD pattern of CuI(*2,6-dimethylpyrazine*). Bottom: TGA profile of CuI(*2,6-dimethylpyrazine*).

4.1.2.2 1D-CuI(*5-bromopyrimidine*)

Synthesis of 1D-CuI(*5-bromopyrimidine*) (**3**): Single crystals of 1D-CuI(*5-bromopyrimidine*) was acquired from solution diffusion method: A solution of CuI (0.190 g; 1mmol) in saturated potassium iodide solution (2 mL) was added with a solution of 5-bromopyrimidine (0.159 g; 1mmol) in acetone (2 mL). 2ml of acetonitrile was used as interlayer between the above two solutions to help crystal growth. The mixture was left at room temperature overnight and the resulting colorless crystals of **3** were collected after filtration.

X-ray structural analysis of compound **3** shows that the structure is built from one-dimensional Cu_2I_2 double-stranded stair. The asymmetric unit contains one crystallographically unique tetrahedral Cu^+ cation, one unique I^- anion and one 5-bromopyrimidine ligand. The rule of charge balance indicates the valences of Cu to be +1. All Cu(I) atoms in the Cu2I2 double-stranded stair are 3-fold coordinated to $\mu3\text{-}I^-$, and all $\mu3\text{-}I^-$ also bridge to three copper atoms giving Cu–I distances varying from 2.607(3) to 2.675(3) Å.
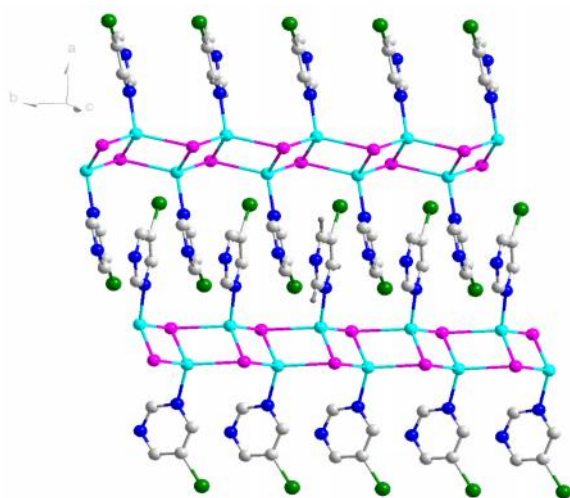
Figure 79: Crystal structure of CuI(*5-bromopyrimidine*). (Cu: light blue; I: purple; Br: green; N: blue; C: grey.)

Comparison between experimental and simulated X-ray diffraction patterns of the 3D-CuI(*5-bromopyrimidine)* sample indicates the pure phase and high crystallinity of the product. The TG analysis was performed under N_2 atmosphere with a heating rate of 10 °C/min in the temperature range 25–450 °C. The TG curve of **3** shows that it is

thermally stable up to 110 °C. Above this temperature, the structure decomposes and only CuI remains. The experimental weight (54%) is close to the percentage of 5-bromopyrimidine in the structure.
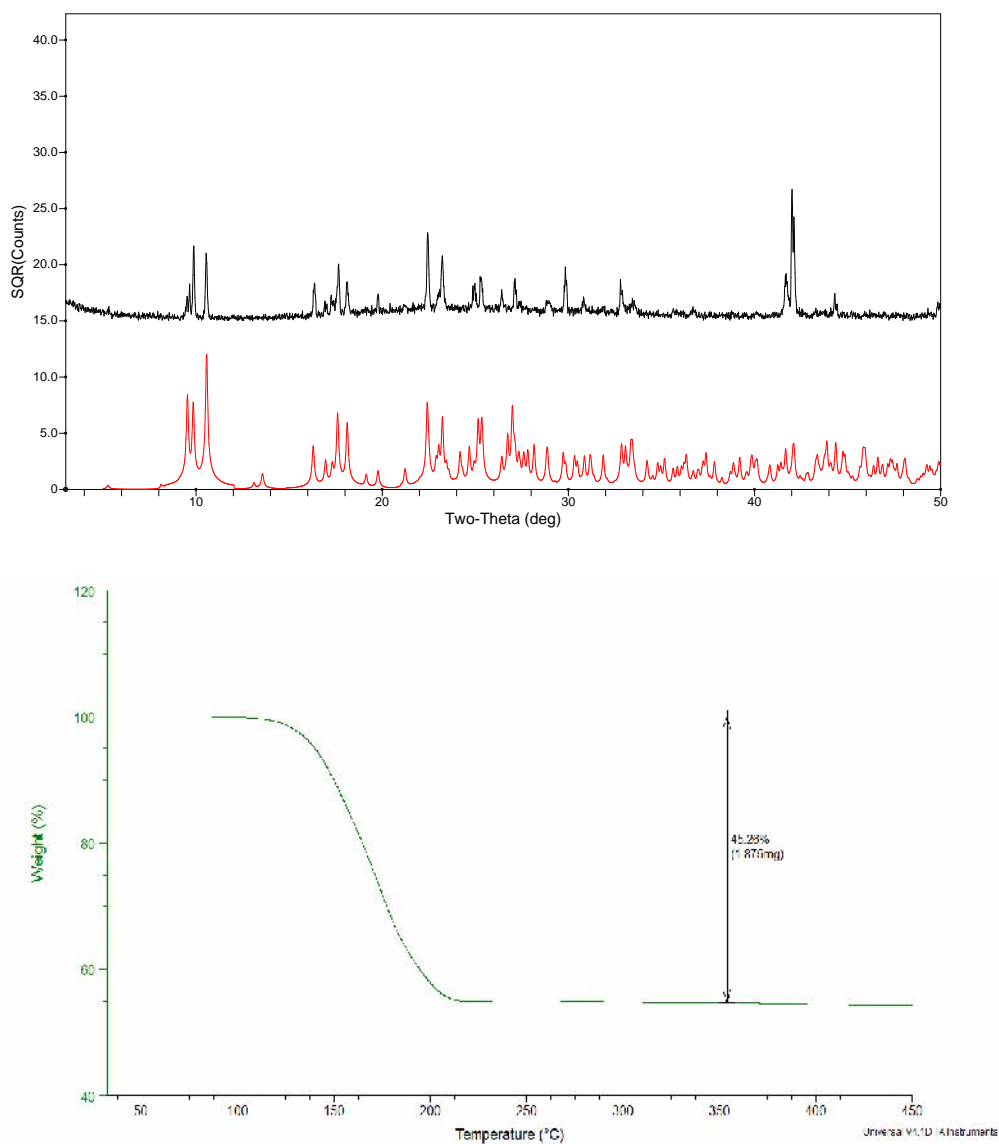
Figure 80: Up: Comparison between experimental and simulated patterns of 3D-CuI(*5-bromopyrimidine*)$_{0.5}$. Down: TGA profile of CuI(*5-bromopyrimidine*)$_{0.5}$.

4.1.2.3 1D-CuI(*3-iodopyridine*)

Synthesis of 1D-CuI(*3-iodopyridine*) (**4**): A solution of CuI (0.190 g; 1mmol) in saturated potassium iodide solution (2 mL) was added with a solution of 3-iodopyridine (0.205 g; 1mmol) in acetone (2 mL). 2ml acetonitrile was used as interlayer between the above two solutions to help crystal growth. The mixture was left at room temperature overnight and the resulting colorless crystals were collected after filtration.

Same as compound **2** and **3**, all Cu(I) atoms in the Cu2I2 ladder are 3-fold coordinated to iodide, and all iodide atoms also bridge to three copper metal centers giving Cu-I distances varying from 2.6344(6) to 2.6711(7) Å. The Cu2I2 double-stranded stair can also be regarded as a ribbon that is formed by connecting the two CuI zigzag single chains via Cu—I bonds.
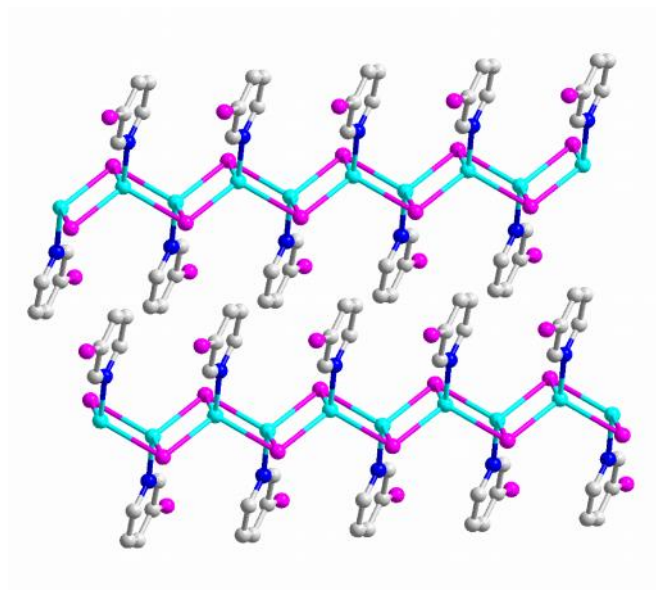
Figure 81: Crystal structures of CuI(*3-iodopyridine*). (Cu: light blue; I: purple; N: blue; C: grey)

Comparison between experimental and simulated X-ray diffraction patterns of 3D-CuI(*3-iodopyridine)* confirms the pure phase of the product. The TG curve of **4** shows that it is thermally stable up to 100 $^{\circ}$ C. Above this temperature, the structure decomposes and only CuI remains. The remaining weight (49%) is close to the percentage of CuI in the hybrid structure.
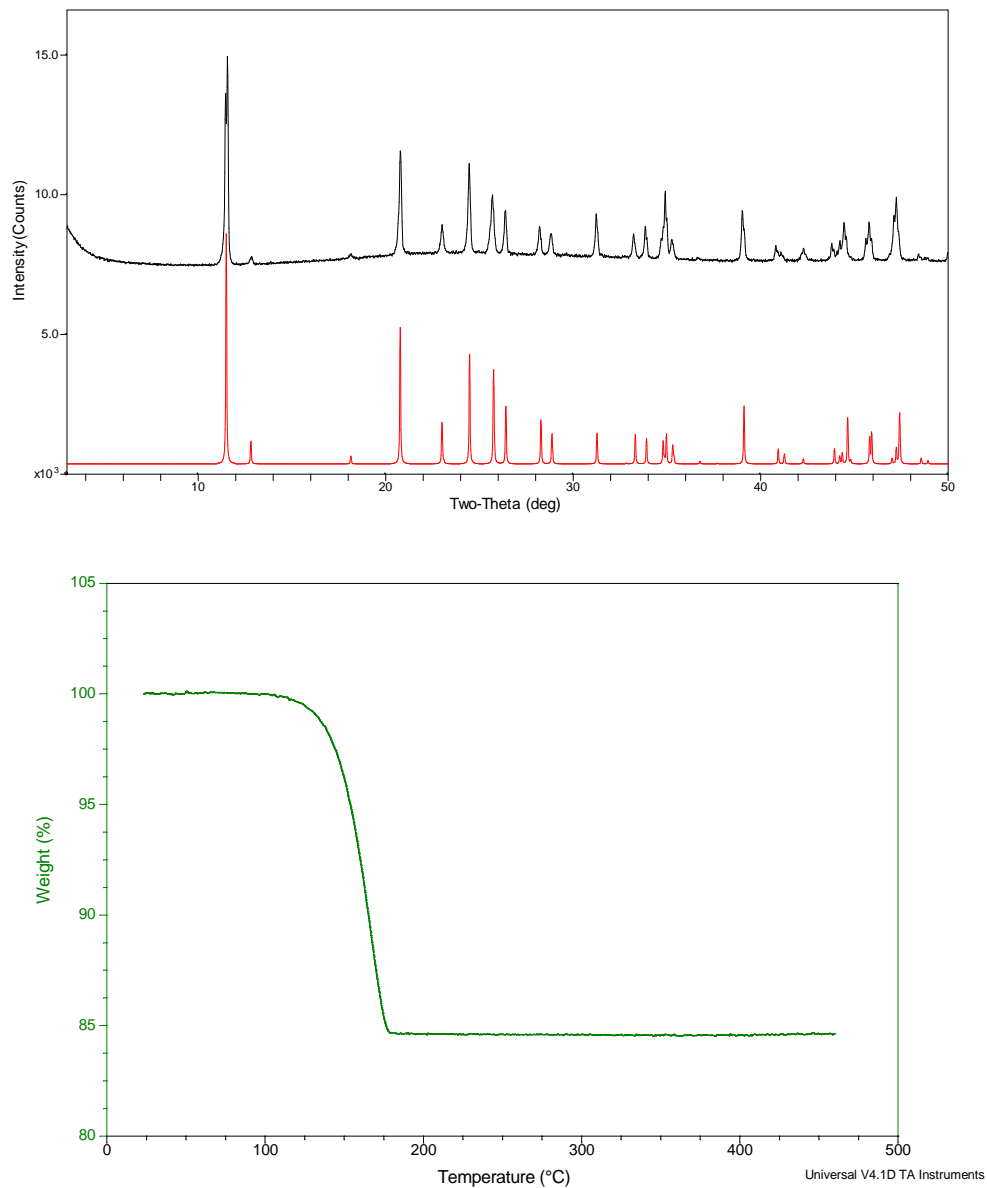
Figure 82: Up: Comparison between experimental and simulated pattern of 3D-CuI(*3-iodopyridine*).Down: TGA profile of CuI(*3-iodopyridine*).

4.1.2.4 1D-CuI(*4-amino-5-iodopyridine*)

Synthesis of 1D-CuI(*4-amino-5-iodopyridine*) (**5**): A solution of CuI (0.190 g; 1 mmol) in saturated potassium iodide solution (2 mL) was added with a solution of 4-

amino-5-iodopyridine (0.220 g; 1 mmol) in acetone (2 mL). 2ml acetonitrile was used as interlayer between the above two solutions to help crystal growth. The mixture was left at room temperature overnight and the resulting yellow crystals were collected after filtration.

Compound **5** crystallizes in the monoclinic structure with space group C2/c. The asymmetric unit of **5** consists of one Cu, one I and one 4-amino-5-iodopyridine ligand, each Cu^+ ion has a tetrahedral geometry composed of three I^- ions and one N from one 4-amino-5-iodopyridine ligand. The Cu–N distance is 2.031(6) Å, and Cu–I bond lengths vary from 2.6411(12) to 2.6820(13) Å. The distance between adjacent Cu ions is 2.9154(14) Å, which shows a weak Cu–Cu interaction.
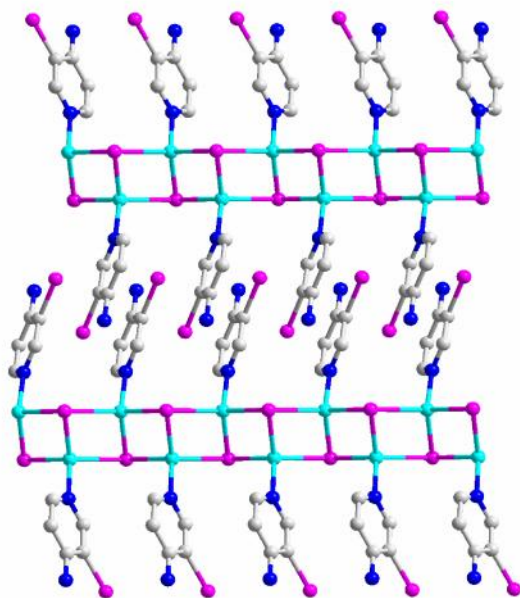
Figure 83: Crystal structures of CuI(*4-amino-5-iodopyridine*)$_{0.5}$. (Cu: light blue; I: purple; N: blue; C: grey).

Comparison between experimental and simulated X-ray diffraction patterns of the CuI(*4-amino-5-iodopyridine*) indicate the pure phase of the product and high crystallinity. The TG analysis was protected by N$_2$ gas with a heating rate of 10 $^{\circ}$C/min in the temperature range 25–450 $^{\circ}$C. The TG curve of **5** shows that it is thermally stable up to 100 $^{\circ}$C. Above this temperature, the structure decomposes and only CuI remains. The remaining weight (47.4%) is close to the percentage of CuI.
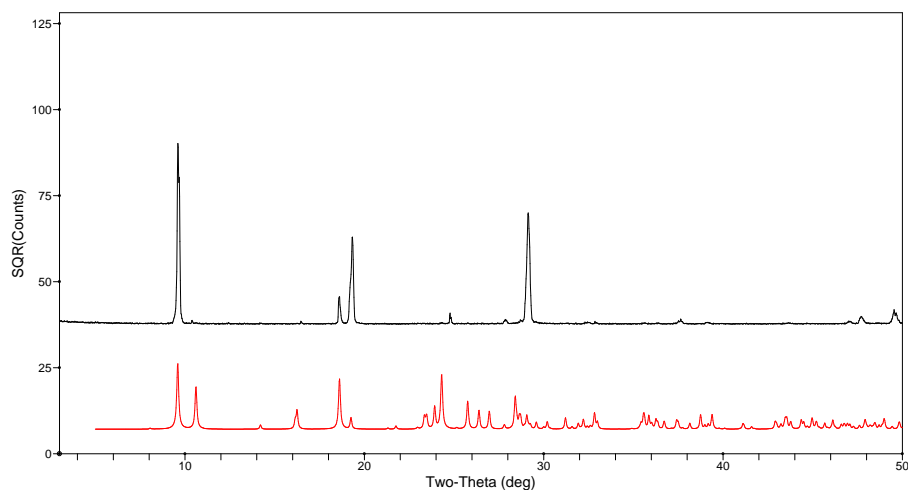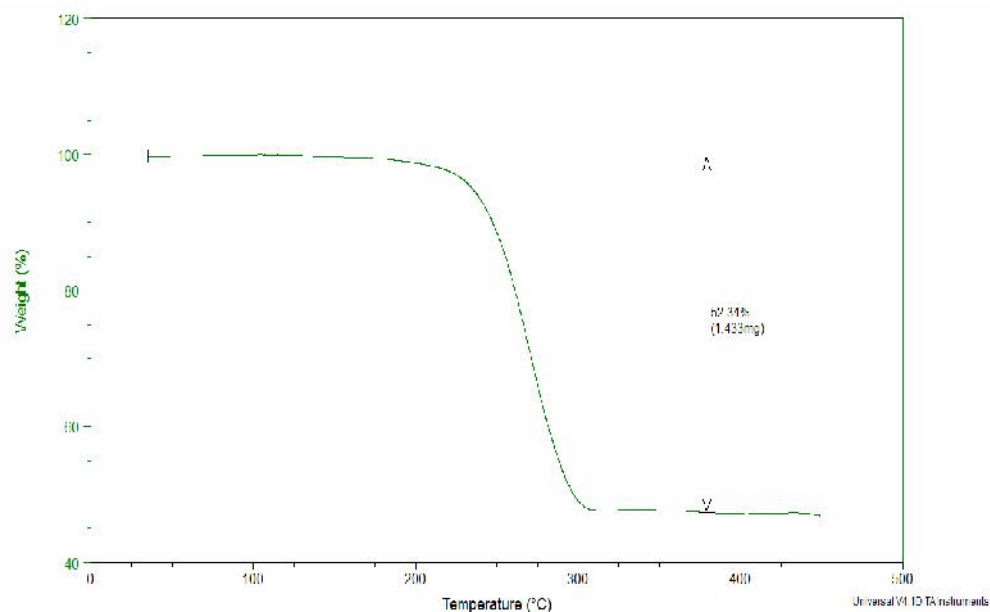
Figure 84: (a) Comparison between experimental and simulated patterns of 3D-CuI(*4-amino-5-iodopyridine*).(b) TGA profile of CuI(*4-amino-5-iodopyridine*).

4.1.2.5 1D-CuI(*3-bromopyridine*)

Synthesis of 1D-CuI(*3-bromopyridine*) (**6**): Pure phase of compound **6** was obtained from a mixture of CuI (0.019 g; 0.1 mmol), 5-bromopyrimidine (0.016 g; 0.1 mmol) and 3 ml acetonitrile. After leaving the mixture over night, the pure white powder of **6** precipitated from solution.

Single crystals of **6** were acquired when a solution of CuI (0.190 g; 1 mmol) in saturated potassium iodide solution (2 mL) was added with a solution of 3-bromopyridine (0.158 g; 1 mmol) and 3-chloropyridine (0.113 g; 0.1 mmol) in acetone (2 mL). 2 ml of acetonitrile was used as interlayer between the above two solutions to help

crystal growth. The mixture was left at room temperature overnight and the resulting colorless crystals were collected after filtration.
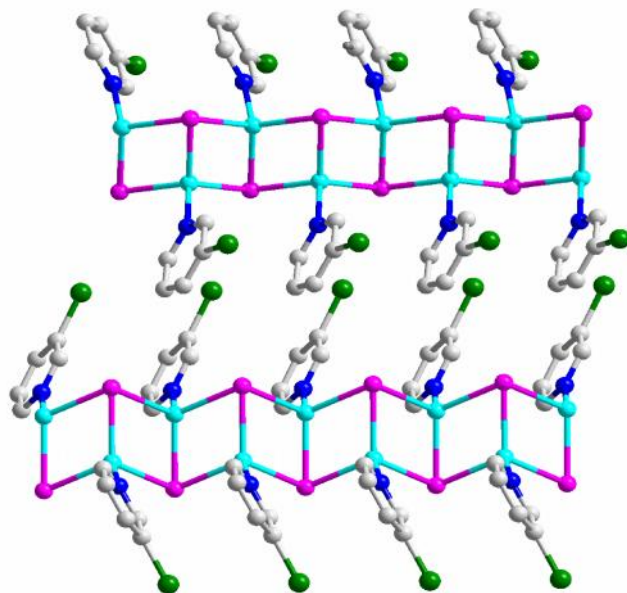
Figure 85: Crystal structures of CuI(*3-bromopyridine*). (Cu: light blue; I: purple; Br: green; N: blue; C: grey)

Compound **6** crystallizes in the monoclinic structure with space group C2/c. The asymmetric unit of **6** consists of one Cu, one I and one 3-bromopyridine ligand, each Cu$^+$ ion has a tetrahedral geometry composed of three I$^-$ ions and one N from one 3-bromopyridine ligand. The Cu–N distance is 2.055(14) Å, and Cu–I bond lengths vary from 2.607(3) to 2.675(3) Å. The distance between adjacent Cu ions are ranging from 2.772(5) to 2.960(5) A °, which shows a weak Cu–Cu interaction.

Comparison between experimental and simulated X-ray diffraction patterns of 3D-CuI(*3-bromopyridine*)$_{0.5}$ samples demonstrates high crystallinity and the pure phase of the product. The TG analysis was performed in N$_2$ atmosphere with a heating rate of 10 $^{\circ}$C/min in the temperature range 25–450 $^{\circ}$C. The TG curve of **6** shows that it is thermally stable up to 100 $^{\circ}$C. Above this temperature, the structure decomposes and only CuI remains. The remaining weight (37%) is close to the percentage of CuI.
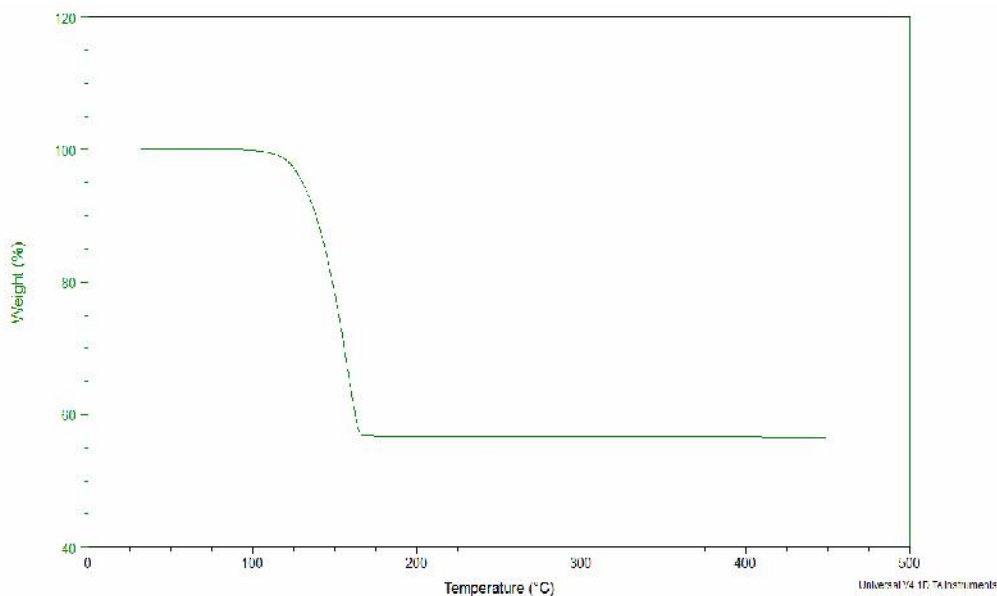
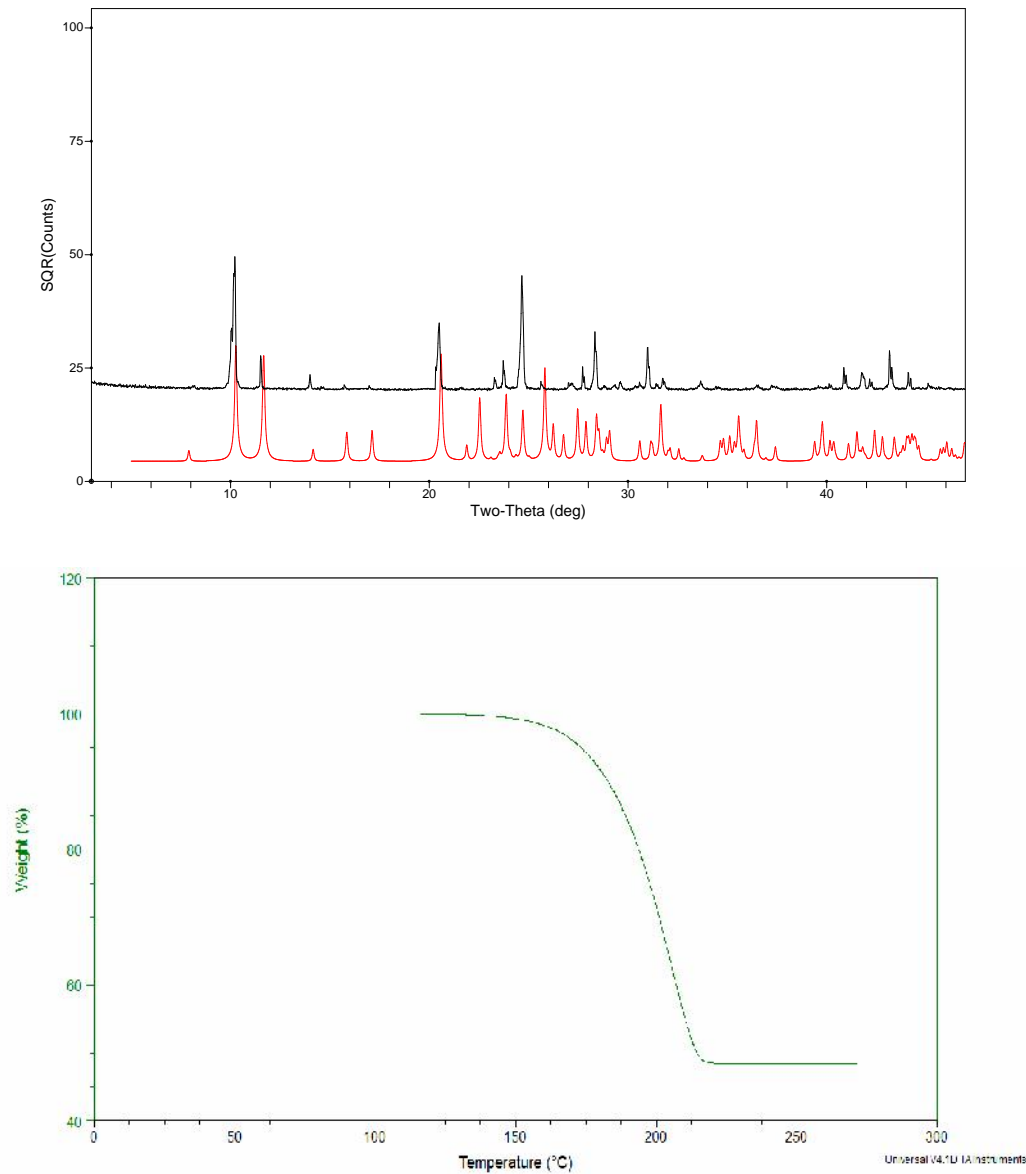Figure 86: (Up) Comparison between experimental and simulated XRD pattern of 3D-CuI(*3-bromopyridine*).(Down) TGA profile of CuI(*3-bromopyridine*).

4.1.2.6 Pyrimidine substituted 1D-CuI(*pyridine*)

Synthesis of pyrimidine doped 1D-CuI(*pyridine*) (**7**): Pure phase of compound **7** was obtained by adding bromopyrimidine (0.016 g; 0.1mmol) in 1ml of acetone drop by drop into a solution of CuI (0.019 g; 0.1mmol) in 2ml of saturated potassium iodide solution. The pure white powder of **7** immediately precipitated from solution.

Single crystals of **7** were acquired when a solution of CuI (0.190 g; 1 mmol) in saturated potassium iodide solution (2 mL) was added to a solution of pyridine (0.079 g; 1 mmol) and pyrimidine (0.004 g; 0.05 mmol) in acetone (2 mL). The mixture was left in the solution at room temperature overnight resulting in colorless crystals.
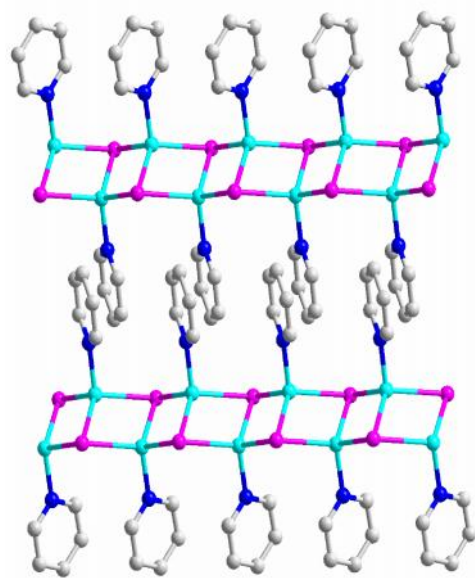
Figure 87: Crystal structure of CuI(*pyridine*). (Cu: light blue; I: purple; N: blue; C: grey)

Comparison between experimental pattern of pyrimidine substituted CuI(*pyridine*) and simulated pattern of CuI(*pyridine*) suggest the substituted compound has the same structure as CuI(*pyridine*). The TG analysis was performed in N_2 atmosphere with a heating rate of 10 °C/min in the temperature range 25–450 °C. The TG curve of **7** shows that it is thermally stable up to 80 °C. Above this temperature, the structure decomposes and only CuI remains. The remaining weight (71%) is close to the percentage of CuI.
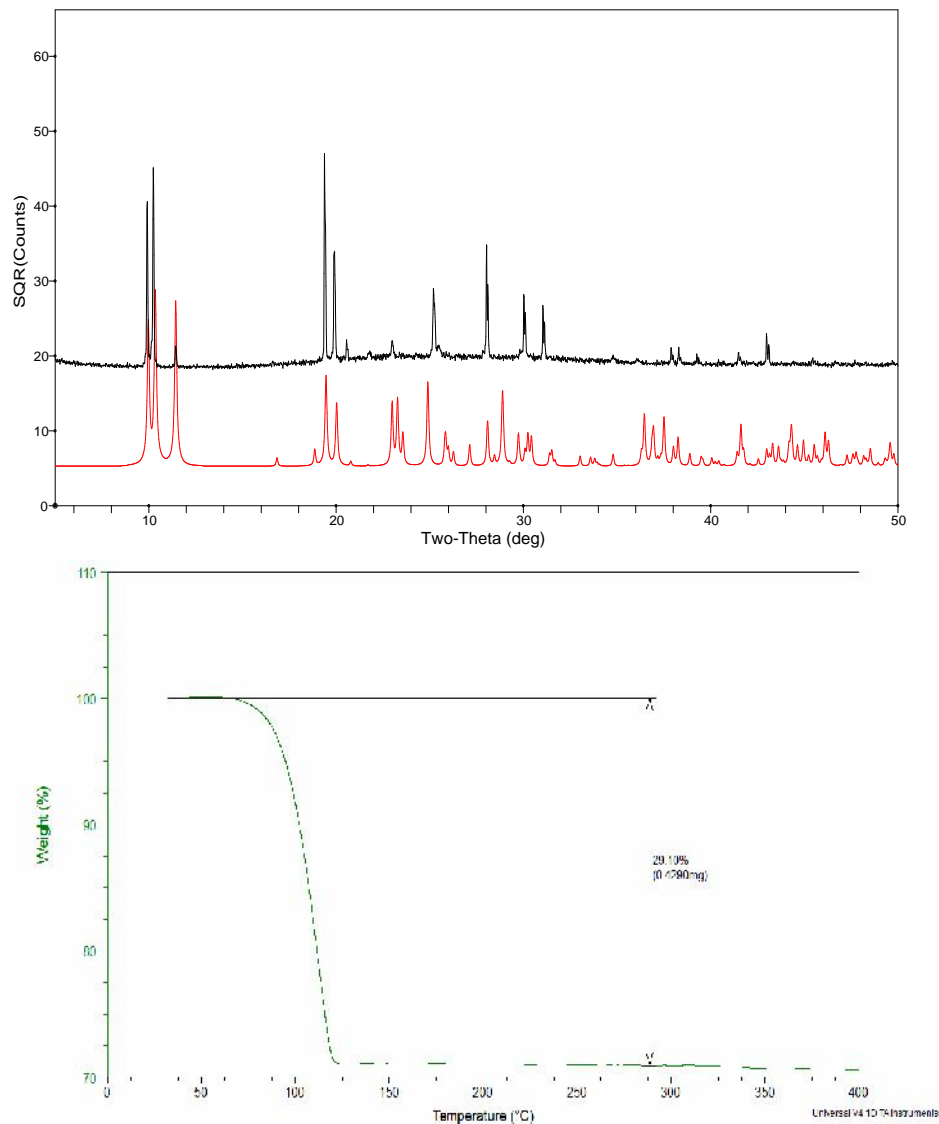
Figure 88: (a) Comparison between experimental pattern of pyrimidine substituted CuI(*pyridine*) and simulated pattern of CuI(*pyridine*).(b) TGA profile of pyrimidine substituted CuI(*pyridine*).

4.2 Optical absorption and emission properties of CuI(L) (L = organic ligand)

4.2.1 3D-CuI(*1,3,5-triazine*)$_{0.5}$

The optical absorption spectra of CuI and CuI(*1,3,5-triazine*)$_{0.5}$ were measured by diffuse reflectance experiments at room temperature with a Shimadzu UV-3101PC double beam, double monochromator spectrophotometer. Data were collected in the wavelength range of 300-800 nm and converted using the Kubelka-Munk function. BaSO$_4$ powder was used as a standard (100% reflectance). The scattering coefficient (S) was treated as a constant since the average particle size of the samples used in the measurements was greatly larger than 5 nm, and the results are plotted in Figure 89. The absorption edges of Cu$_2$I$_2$(*1,3,5-triazine*) are found to be 2.5 eV. Compared to the measured value of 3.0 eV for β-CuI, it clearly indicates a significant red shift.
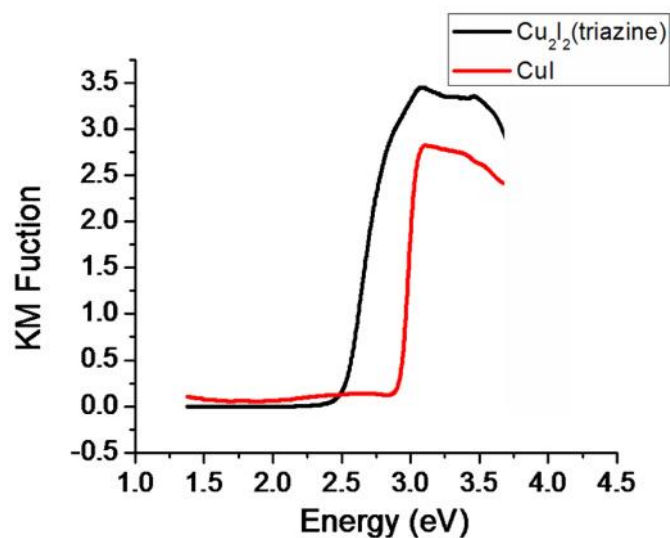
Figure 89: Optical absorption of CuI and CuI(1,3,5-*triazine*)$_{0.5}$.

In order to understand the optical absorption behavior of Cu_2I_2(*1,3,5-triazine*), DFT calculation were performed on both CuI and Cu_2I_2(*1,3,5-triazine*). The band gap structures of both compounds are shown in Figure 90 and Figure 91. The calculated band structure of CuI indicates the direct band gap of 0.991 eV, about 2 eV lower than its experimental band gap. For Cu_2I_2 (*1,3,5-triazine*), it shows direct band gap of 0.835 eV, which is also about 2 eV lower than its experimental value. The relative band gap value between two compounds from calculation is consistent with their experimental value.
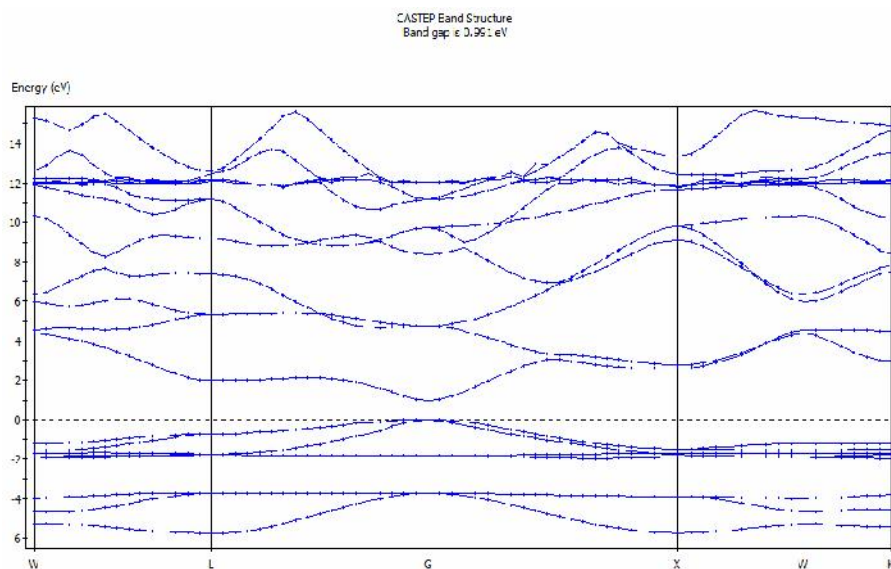
Figure 90: Band structure of CuI from DFT calculation.
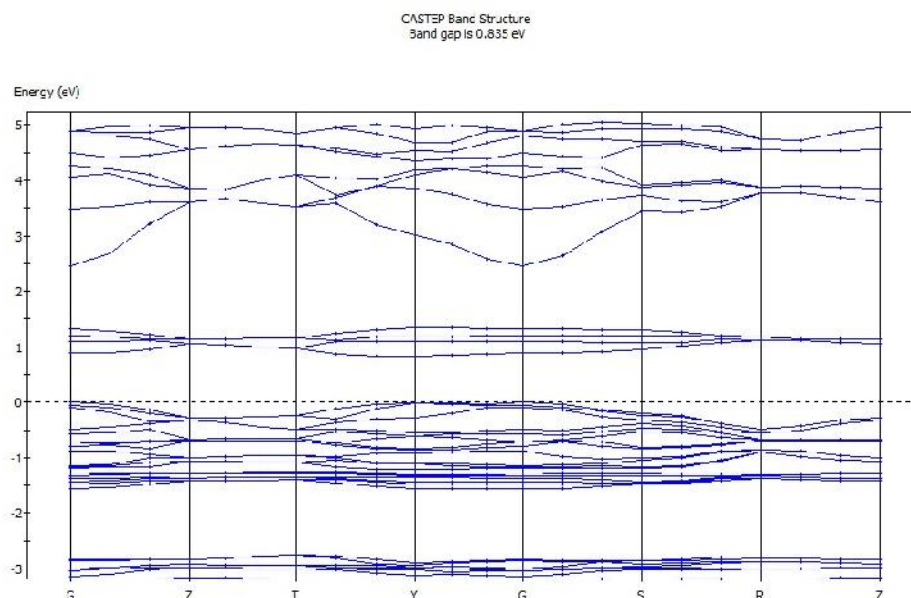
Figure 91: Band structure of Cu₂I₂ (*1,3,5-triazine*) from DFT calculation.

Density of states (DOS) analysis has revealed some interesting information about the composition of the bands. As shown in Figure 93(a), the valence band is mainly contributed by the Cu (3d), I (5p) and Cu (4p) orbitals from inorganic module and the band shape is similar to the valance band shape of CuI (see Figure 92), while the conduction band is mainly contributed by the atomic orbitals of C (2p) and N (2p) from organic ligands (see Figure 93(b)). There is another continuous energy band above conduction band energy level and its band shape is similar to CuI conduction band and is mostly contributed by the atomic orbitals of inorganic modules such as Cu (4s), Cu (4d), Cu(3p) and I(5s). The energy gap between two "inorganic bands" (valence band and the band above conduction band) is about 2.9eV (2.9eV – 0eV), about 1.9 eV higher than 0.991 eV of CuI band gap. These results may be explained by quantum

confinement effect when the inorganic layers are separated between each other and the spatial confinement of electrons cause the separation of energy levels. This phenomenon was first observed in our II-VI inorganic organic hybrid materials.
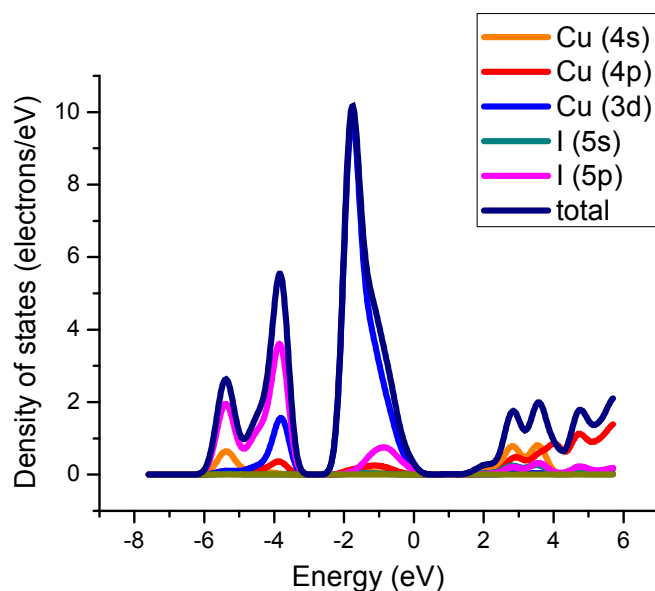
u

Figure 92: Density of states of CuI from DFT calculation.

(a)　　　(b)
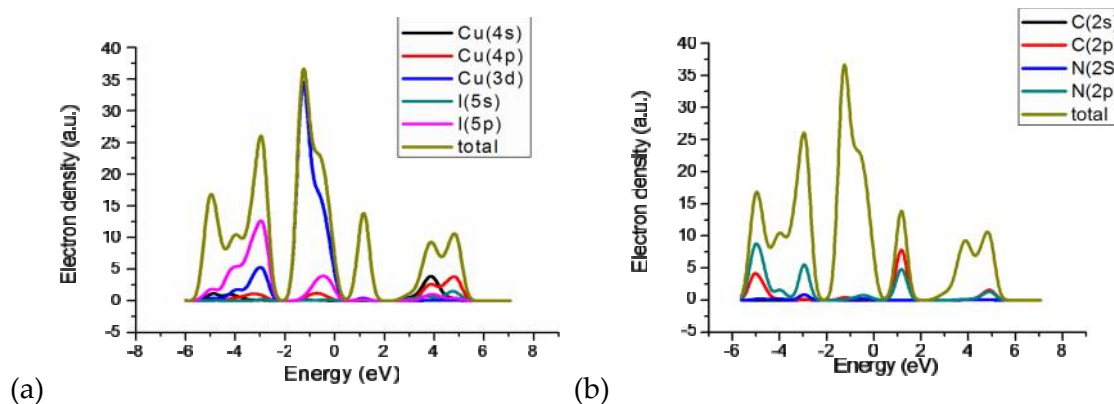
Figure 93: Density of states of (a) inorganic parts and (b) organic parts of Cu_2I_2(*1,3,5-triazine)* from DFT calculation.

Figure 94 shows the photoluminescence of $Cu_2I_2(1,3,5\text{-}triazine)$ and CuI with the excitation wavelength of 320 nm. Compared to the sharp peak of CuI at 410nm, the $Cu_2I_2(1,3,5\text{-}triazine)$ shows a broad PL coverage ranging from 470 nm to 750 nm, covering much of visible light area.
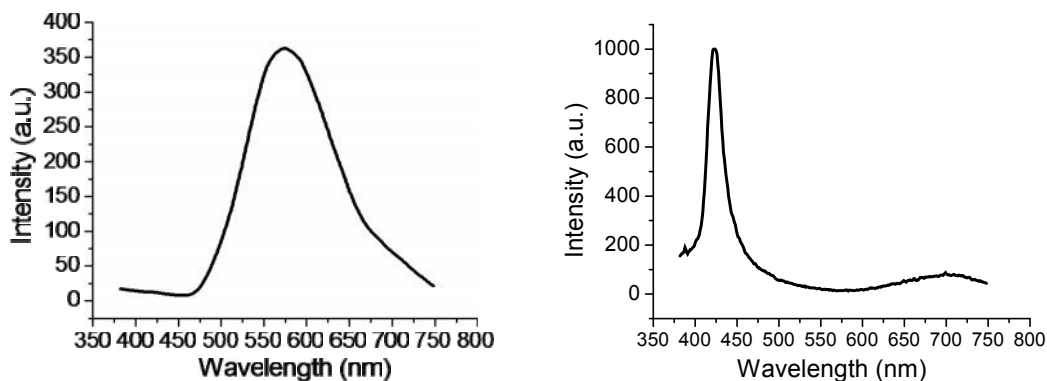
Figure 94: Photoluminesence of $Cu_2I_2(triazine)$ and CuI with the excitation wavelength of 320 nm.

4.2.2 1D-CuI(*L*)

The optical absorption and emission behavior were also tested on 1D-CuI(*L*) structures, the parent structure of which is α-CuI. The results are summarized in Table 13. Keeping the 1D chain inorganic module intact, the band gap has been systematically tuned from 2.2 eV to 3.2 eV just by changing organic ligands. The starting wavelengths in PL spectra of these materials are strongly related to their band gap. The structure with larger band gap generally have lower starting wavelength in its PL spectrum. When the numbers of starting wavelengths are transferred to electron voltages using Einstein's photoelectric equation, the values are just a little larger than their relative band gap.

These results again suggest that 1D-CuI(*L*) inorganic organic hybrid semiconductors exhibit band gap emission.

Table 13: Summary of optical absorption and emission behavior of 1D-CuI(*L*) inorganic organic hybrid structures.

Structures	Band Gap	Emission Peak (nm)	Emission Range(nm)	Emission Color
CuI(*2,6-dimethylpyrazine*)	2.2 eV	500 (C)	460-580	yellow
CuI(*pyrimidine*)	2.6 eV	525 (C)	470-670	green
CuI(*5-bromopyrimidine*)	2.5 eV	500,610nm	440-700	yellow white
CuI(*3-iodopyrimidine*)	2.8 eV	NA	NA	NA
CuI(*3-bromopyridine*)	2.8 eV	450,530	400-650	blue white
CuI(*pyridine*)	3.0 eV	450	380-550	light Blue
CuI(*4-amino-5-iodopyrimidine*)	3.2 eV	NA	NA	NA

(a)

(b)

(c)

(d)

(e)

(f)

(g)
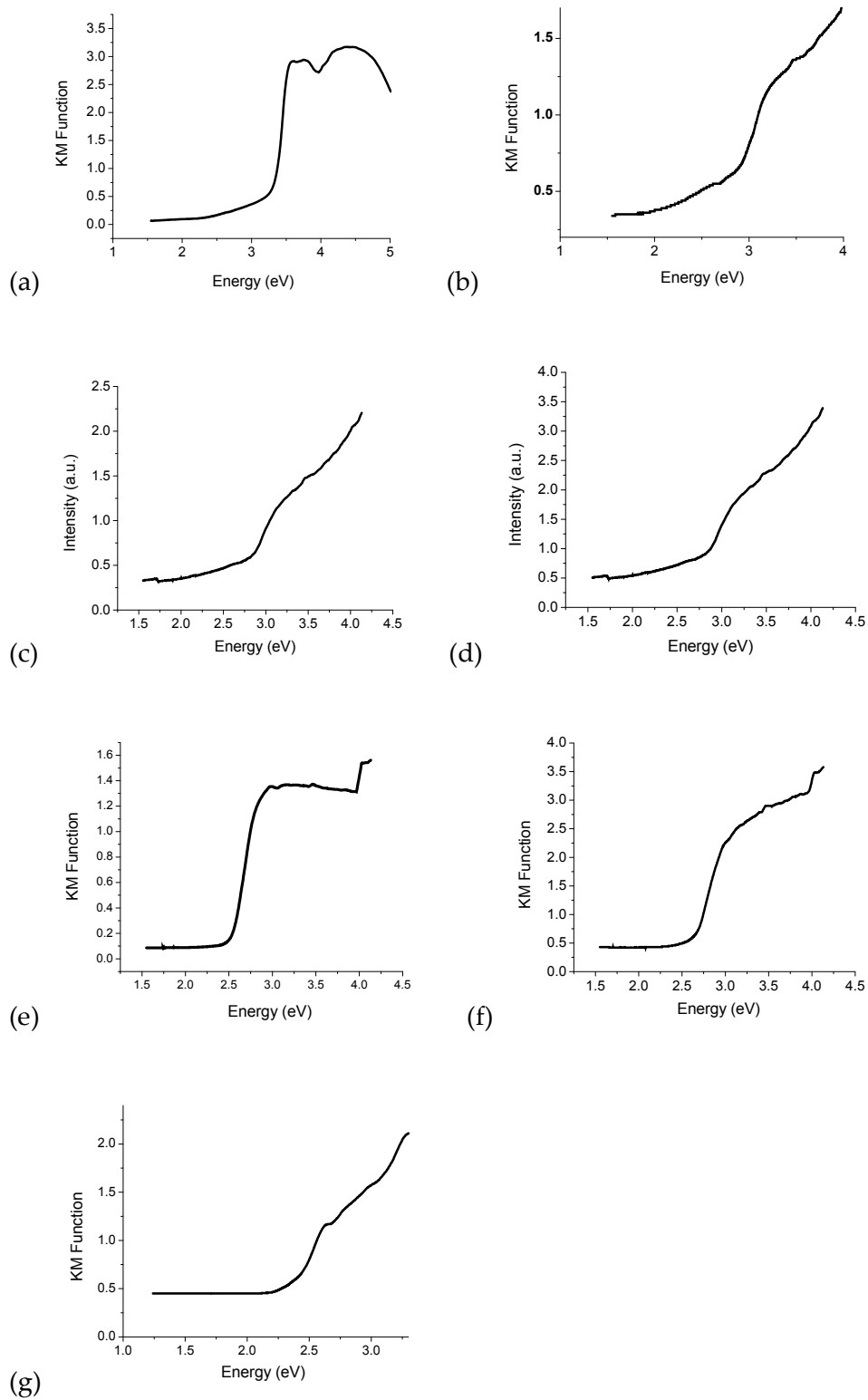
Figure 95: The optical absorption behavior of (a) CuI(*4-amino-5-iodopyridine*), (b) CuI(*3-iodopyridine*), (c) CuI(*3-iodopyridine*), (d) CuI(*pyrdine*), (e) CuI(*5-bromopyrimidine*), (f) CuI(*pyrimidine*) and (g) CuI(*2,6-dimethylpyrazine*).

DFT calculation was performed on the selected compounds CuI(*4-amino-5-iodopyridine*) and CuI(*2,6-dimethylpyrazine*) to understand their band structures.

The calculated band gap of CuI(*4-amino-5-iodopyridine*) is 1.8 eV, 1.5 eV less than its experimental value, which is common for DFT calculation. A closer look at the density of states reveals that the valence band of CuI(*4-amino-5-iodopyridine*) mainly consists of the 3d orbitals of copper and the 5p orbitals of iodide (see Figure 96), while the conduction band is mainly contributed by the 2p orbitals of carbon and nitrogen atoms. The results suggest that the band gap absorption and emission processes of CuI(*4-amino-5-iodopyridine*) involves charge transfer between the organic molecules and the inorganic CuI modules.
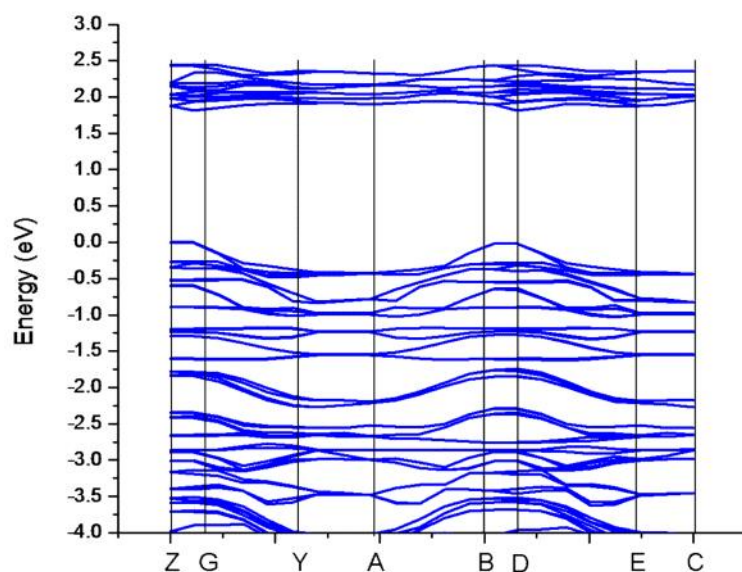
Figure 96: Band structure of Cu$_2$I$_2$(*4-amino-5-iodopyridine*) from DFT calculation.
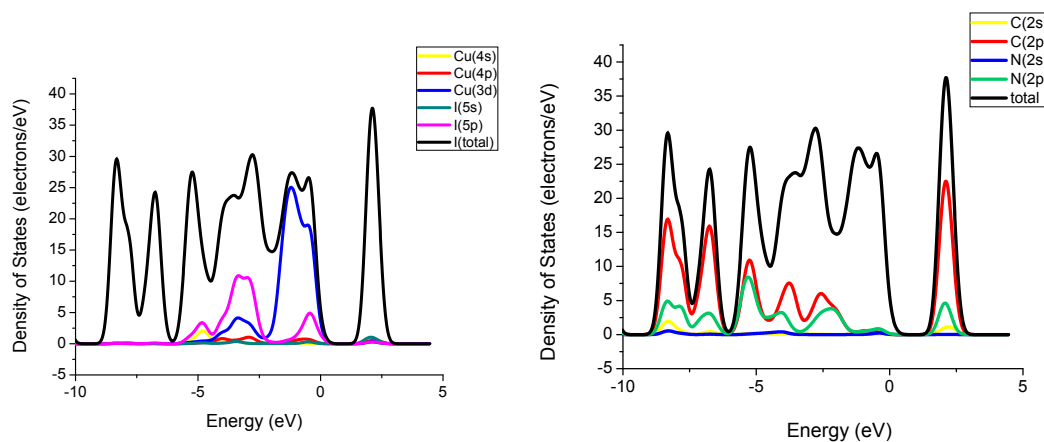
Figure 97: Density of states of (a) inorganic parts and (b) organic parts of CuI(*4-amino-5-iodopyridine*) from DFT calculation.

To further confirm the theory, we have also calculated the band gap and density of states of CuI(*2,6-dimethylpyrazine*). Band structure plotted from calculation results are

shown in Figure 98, which demonstrates the indirect band gap of CuI(*2,6-dimethylpyrazine*). The calculated value of its band gap is 0.991 eV, about 1.3eV less than its experimental value. The density of states diagram of CuI(*2,6-dimethylpyrazine*) resembles that of CuI(*4-amino-5-iodopyridine*). The valence band of CuI(*4-amino-5-iodopyridine*) is also composed of the 3d orbitals of copper and the 5p orbitals of iodide (see Figure 99), while the conduction band is made of the 2p orbitals of both carbon and nitrogen atoms. This result further confirms the band gap absorption in 1D-CuI(*L*) involves charge transfer from HOMO of CuI modules to the LUMO of organic molecules.
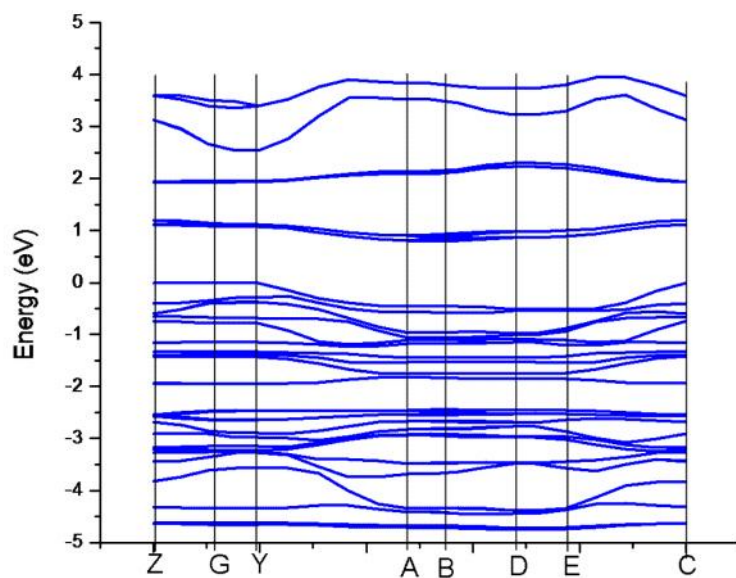
Figure 98: Band structure of CuI(*2,6-dimethylpyrizine*) from DFT calculation.
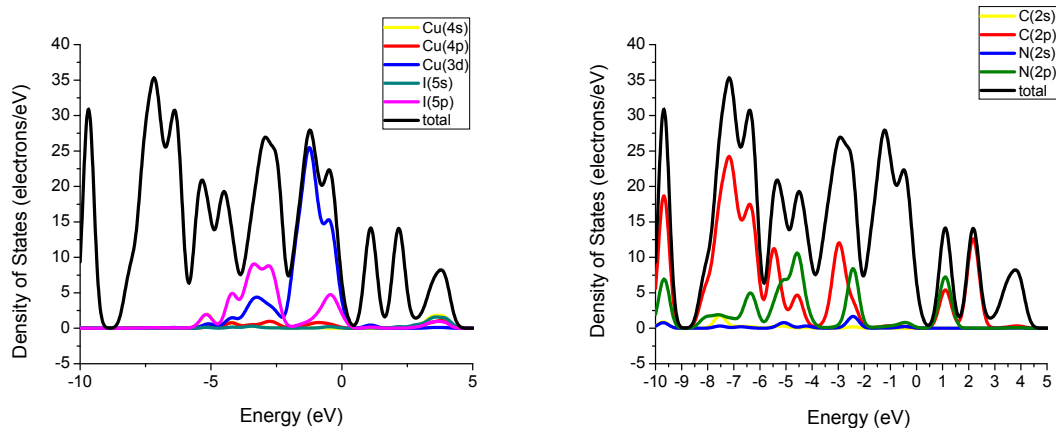
Figure 99: Density of states of (a) inorganic parts and (b) organic parts of CuI(*2,6-dimethylpyrizine*) from DFT calculation.

To further understand the impact of LUMO energy levels of organic ligands on the band gap of 1D-CuI(*L*) inorganic organic hybrid structures, we have also calculated the HOMO and LUMO energy levels of different organic ligands on Guassian [09] with the hybrid functional: [B3LYP]. Three basis sets, 3-21G, 6-311+G and DGDZVP were used for the calculation and results are listed in Table 13. The 3-21G basis set is smaller than 6-311+G* and DGDZVP, so the results can only be used as rough comparison. Although the 6-311+G* basis set is more accurate than 3-21G, it is not suitable in calculating the molecules containing fifth row element such as iodine. DGDZVP (density Guass double-zeta with polarization functions) is a full-electron basis set that contains 36 basis functions and 114 Guassian primitive functions. And it has been demonstrated giving better results in terms of describing the geometries of iodine-containing compounds than basis sets with pseudopotential. Therefore DGDZVP basis set is most

suitable in calculating the listed organic molecules. The calculation results demonstrate the significant correlation between the electronic affinity of functional groups and the energy levels of HOMO and LUMO as show in Table 14. To be specific, molecules (i) - (v) are pyridine and its derivatives. For the molecule (iii) – (v), there is only halide group (I, Br, Cl) on the pyridine ring. The electron withdrawing effect of halide group in these structures declines both the HOMO and LUMO energy levels compared to pyridine. In contrary, when an electron donating group such as amino group is further attached to the pyridine ring, as in case (ii), the HOMO and LOMO energy levels become higher than pyridine. Similar phenomena are also observed in pyrimidine's and pyrazine's derivatives. For example, 2,6-dimethylpyrazine (vii) has two methyl groups (electron donating functional group) on the pyrazine framework, and its LUMO and HOMO are higher than pyrazine (viii). The 5-bromopyrimidine (ix) has electron withdrawing bromo group attached to pyrimidine ring and its energy levels become lower than pyrimidine (vi). These results can be summarized as both HOMO and LUMO energy levels of aromatic molecules are decreased by electron withdrawing functional group and increased by electron donating functional group.

Based on this conclusion and the idea that the energy levels of conduction bands of 1D-CuI(L) structures are then determined by LUMO energy level of organic ligands, we have proposed a method to tune the band gap absorption and emission behavior of 1D-CuI(L) inorganic organic semiconductors. We maintain the one dimensional CuI

chain while varying the functional group (electron donating or electron withdrawing group) on the organic molecules, the LUMO energy of the organic molecules, and thereby the conduction band of the hybrid structures can be systematically tuned.

Table 14: Calculated HOMO and LUMO energy levels of organic molecules with different basis sets.

Method	B3LYP[1-3]					
Basis Set	3-21G		6-311+G*		DGDZVP	
Name	HOMO (eV)	LUMO (eV)	HOMO (eV)	LUMO (eV)	HOMO (eV)	LUMO (eV)
pyridine (i)	-6.571	-0.559	-7.226	-1.103	-7.175	-1.041
4-amino-5-iodopyridine(ii)	-6.028	-0.850	N/A	N/A	-6.571	-1.278
3-chloropyridine (iii)	-7.105	-1.099	-7.390	-1.472	-7.340	-1.428
3-bromopyridine (iv)	-6.919	-0.916	-7.272	-1.485	-7.228	-1.441
3-iodopyridine (v)	-6.763	-1.028	N/A	N/A	-6.981	-1.454
pyrimidine (vi)	-6.611	-1.139	-7.288	-1.608	-7.237	-1.549
2,6-dimethyl pyrazine (vii)	-6.242	-1.094	-6.896	-1.632	-6.829	-1.552
pyrazine (viii)	-6.537	-1.372	-7.181	-1.874	-7.125	-1.795
5-bromo pyrimidine (ix)	-6.923	-1.485	-7.587	-1.982	-7.550	-1.943

1. A. G. Yurieva, O. K. Poleshchuk, V. D. Filimonov, *J Struct Chem* **2008**, *49*, 548-552.

2. N. Godbout, D. R. Salahub, J. Andzelm, E. Wimmer, *Canadian Journal of Chemistry* **1992**, *70*, 560-571.

3. C. Sosa, J. Andzelm, B. C. Elkin, E. Wimmer, K. D. Dobbs, D. A. Dixon, *The Journal of Physical Chemistry* **1992**, *96*, 6630-6636.

This idea has been tested by comparing the experimental band gap and the PL spectra of the new 1D-CuI(*L*) structures with the calculated LUMO energy level of their ligands. The results are summarized in Table 15. The band gap of these structures increase in the order of **3** < **4** < **5** < **7** < **6** and the starting wavelengths decrease in the order of **7** > **4** > **3** (5 and 6 are not fluorescent), similar to the calculated LUMO trend of **4** < **3** < **5** < **7** < **6**. This result further validates our hypothesis.

Table 15: The comparison between the band gap of 1D-CuI(*L*) structures, calculated LUMO energy level at B3LYP/DGDZVP and emission range.

1D-CuI(*L*) structures	Band Gap	Calculated LUMO position	PL emission range
CuI(*2,6-dimethylpyrazine*) (**2**)	2.2 eV	-1.552	460-580nm
CuI(*5-bromopyrimidine*) (**3**)	2.5 eV	-1.943	440-700nm
CuI(*3-iodopyrimidine*) (**4**)	2.8 eV	-1.454	NA
CuI(*3-bromopyridine*)(**6**)	2.8 eV	-1.441	400-650nm
CuI(*4-amino-5-iodopyrimidine*) (**5**)	3.2 eV	-1.278	NA

During the fluorescence measurement of new CuI(*L*) inorganic organic hybrid structures, we found the ligands with bromo group such as 3-bromopyridine and 5-

bromopyrimidine can give wide and balanced spectra. Compared to other CuI(*L*) compounds with single and sharp emission peak, both the CuI(*Br-pyridine*) and CuI(*Br-pyrimidine*) display double peaks which cover more than 250 nm out of 300 nm in the visible light range (400 nm-700 nm). The CIE calculation gives (0.26, 0.35) for CuI(*Br-pyridine*) and (0.36, 0.41) for CuI(*Br-pyrimidine*) as their CIE coordinates. These results indicate the emission color is already within white light area.

(a)

(b)

(c)
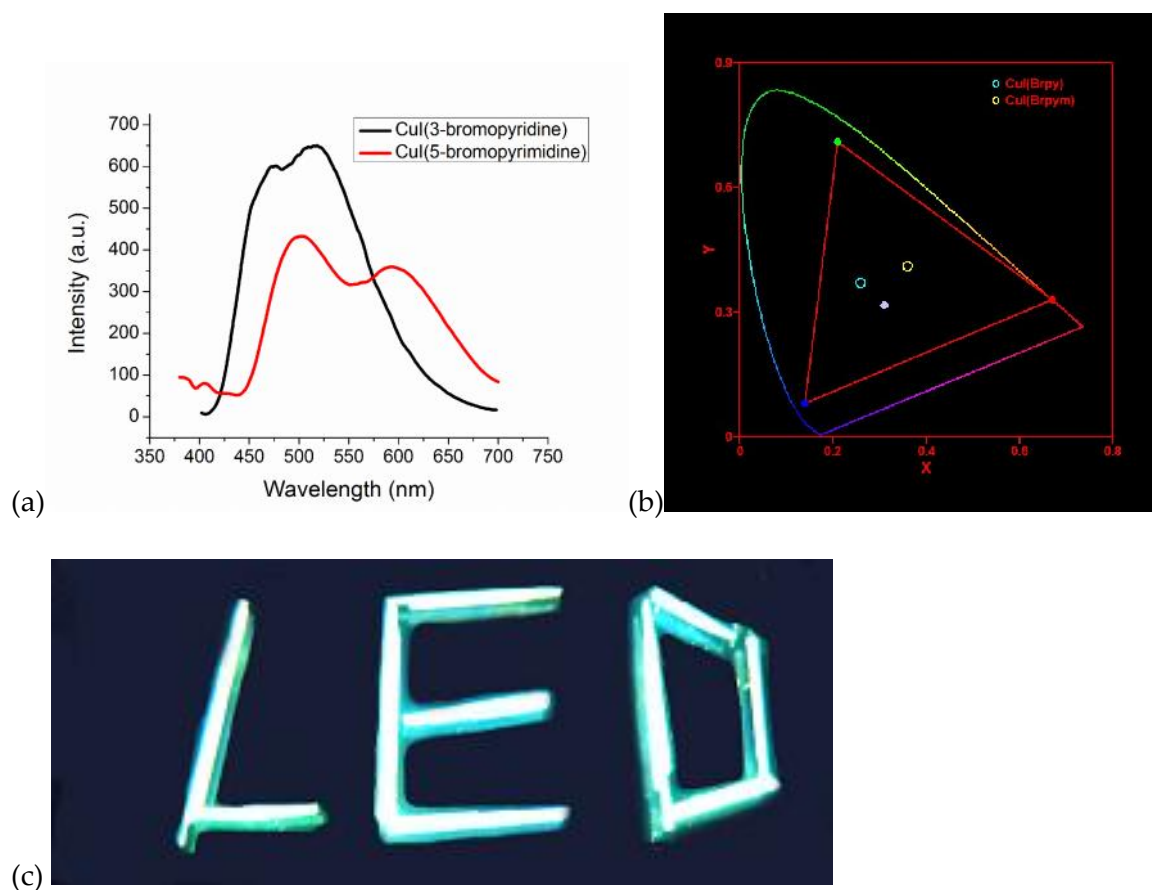
Figure 100: The PL spectra (left) and CIE coordinates (right) of CuI(*3-bromopyridine*) (black curve and light blue circle) and CuI(5-*bromopyrimidine*) (red curve and light

yellow circle). (c) Logo made from white light emitting pyrimidine substituted CuI(*pyridine*) powders.

To further increase the white light coverage, we have tried to synthesize CuI(*L*) structures with mixed ligands. CuI(*pyrimidine*) and CuI(*pyridine*) show 0.3 eV difference of band gap as shown in Figure 101. The reason of the difference is that LUMO energy level of pyridine is higher than that of pyrimidine. There are two electron-rich nitrogen atoms in the aromatic ring of pyrimidine compared to one nitrogen atom in pyridine and it cause both HOMO and LUMO energy levels in pyrimidine to increase. The PL spectra show the emission range of CuI(*pyrimidine*) and CuI(*pyridine*) start from 400nm and 460 nm, respectively, corresponding to their band gap values. The emission intensity is strong, but both compounds suffer from the narrow coverage. To solve the problem, we have prepared pyrimidine substituted CuI(*pyridine*) as discussed in previous chapter. The colorless crystals of substituted compounds have same XRD pattern as unsubstituted CuI(*pyridine*) structure and it does not show changes in UV spectrum either. However, the emission from the crystals surprisingly covers the whole visible light area from 400 nm to 700 nm, giving CIE coordinates (0.31, 0.33), right on the pure white light spot. The Color Rendering Index (CRI) and Correlated Color Temperature (CCT) of the compound are computed to be 87.4 and 6455K, indicating its strong ability to reproduce the colors of various objects faithfully.
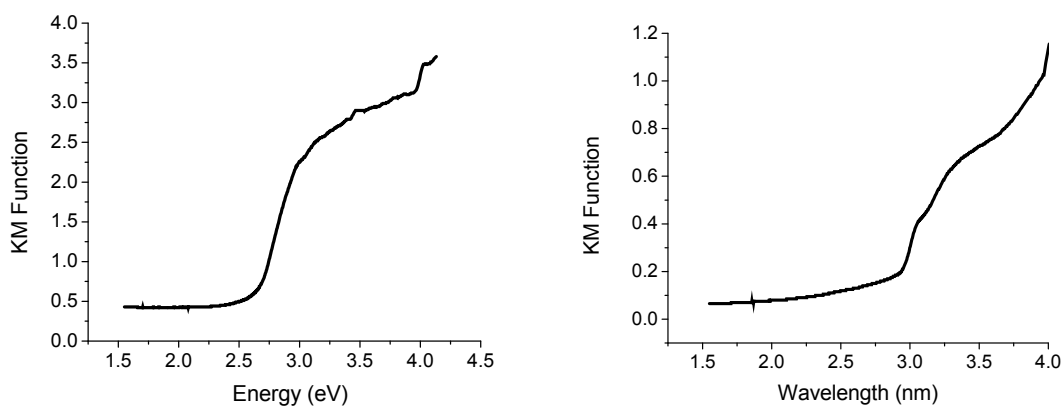
Figure 101: The optical absorption spectrum of CuI(*pyrimidine*)$_{0.5}$ (left) and CuI(*pyridine*) (right).

(a)

(b)

(c)

(d)

(e)
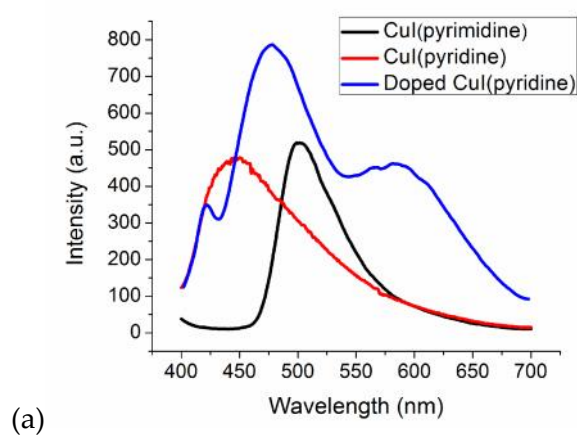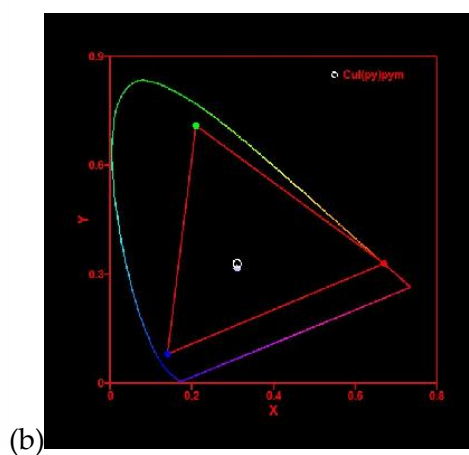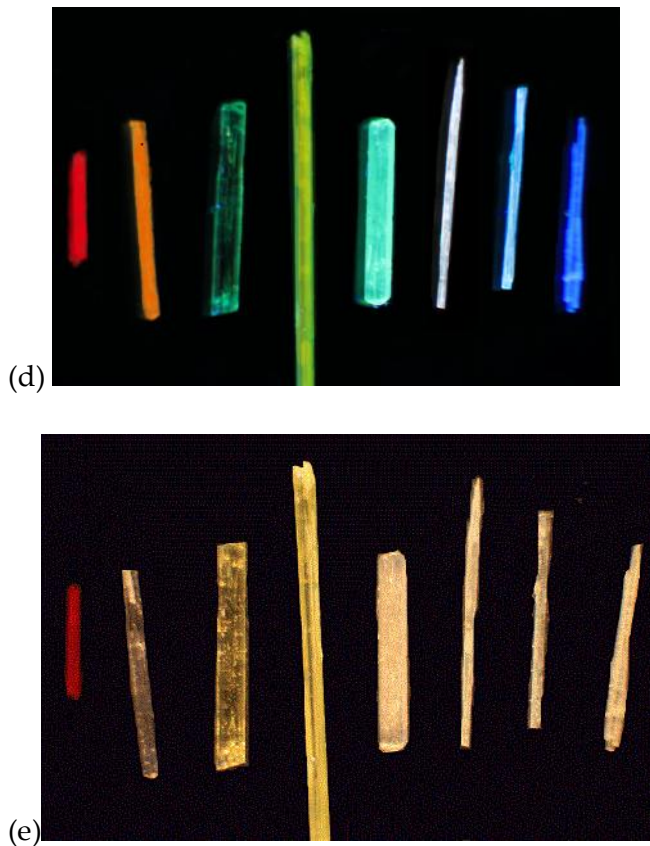
Figure 102: (a): The PL spectra of pyrimidine substituted CuI(*pyridine*) (blue), CuI(*pyridine*) (red) and CuI(*pyrimidine*) (black). (b): CIE coordinates of pyrimidine substituted CuI(*pyridine*). (c) Logo made from white light emitting pyrimidine substituted CuI(*pyridine*) powders. (d) Comparison between white light emitting pyrimidine substituted CuI(*pyridine*) crystal with other 1D-CuI(L) crystals under the UV light. (e) Comparison between white light emitting pyrimidine substituted CuI(*pyridine*) crystal with other 1D-CuI(L) crystals under the ambient light.

4.4 Mechanochromic properties of CuI(L) (L = organic ligand)

During the process of investigating luminescence properties of hybrid materials based on 1D-CuI(*L*) inorganic organic hybrid semiconductors, we have also discovered mechanochromic properties in CuI(*2,6-dimethylpyrazine*) and CuI(*pyrimidine*).

The CuI(*2,6-dimethylpyrazine*) cluster is a light yellow powder under ambient light. Under UV irradiation (peak wavelength at 365 nm), the structure gives strong yellow emission as shown in Figure 103. The mechanochromic properties were observed when grinding the samples in mortar. The yellow emission becomes red under UV light after grinding.

Solid state emission was recorded for the cluster before and after grinding at room temperature. For the crystals before grinding, a broad emission band is observed at λ_{max} = 530 nm under excitation at λ_{ex} = 365 nm. This is in agreement with the observed yellow emission. After grinding, a broad emission band is observed at λ_{max} = 625 nm (λ_{ex} = 360 nm) in agreement with the red emission. Comparison between the XRD patterns before and after griding suggest the structural change under the applied pressure when grinding.
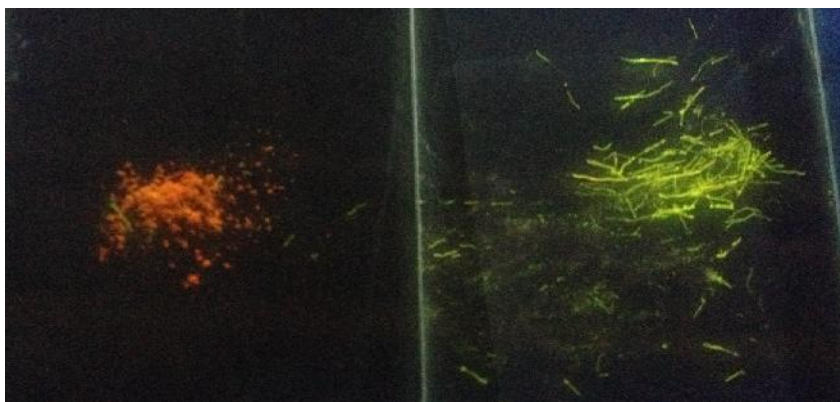
Figure 103: Photos showing the photoluminescence change of CuI(*2,6-dimethylpyrazine*) after (left) and before (right) griding.
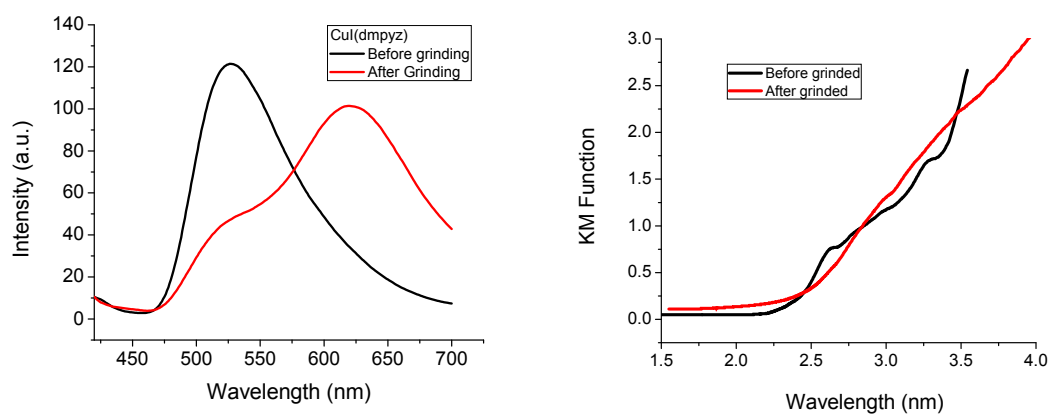
Figure 104: (left) PL changes of CuI(*2,6-dimethylpyrazine*) before and after grinding. (right) UV changes of CuI(*2,6-dimethylpyrazine*) before and after grinding.
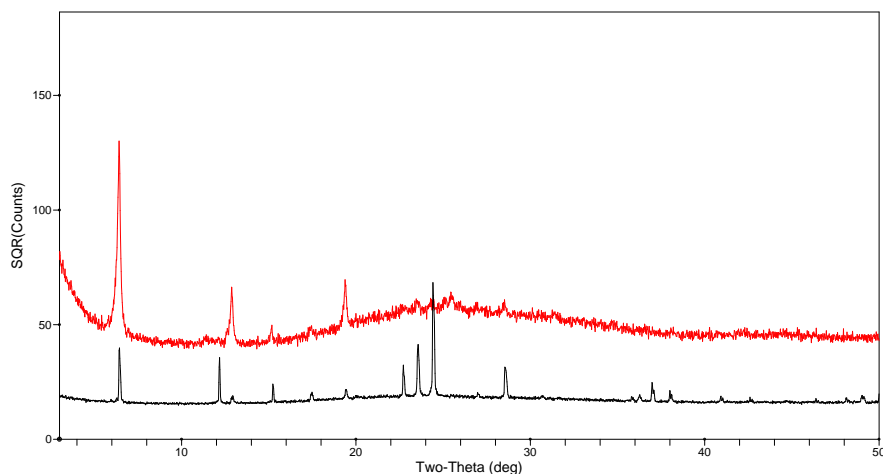
Figure 105: Comparison of XRD patterns before (black) and after (red) griding.

Another compound showing the mechanochromic property is the CuI(*pyrimidine*)$_{0.5}$. The CuI(*pyrimidine*)$_{0.5}$ crystals is shining with green light under ambient light. At room temperature and under UV lamp irradiation (peak wavelength at 365 nm), a strong orange emission was observed as shown in Figure 106. The mechanochromic properties were observed when grinding the samples in mortar. The green emission becomes orange under UV light after grinding.

Solid state emission was recorded for the cluster before and after grinding at room temperature. For the crystals before grinding, a broad emission band is observed at λ_{max} = 500 nm under excitation at λ_{ex} = 365 nm. This is in agreement with the yellow emission observed. After grinding, the original emission peak decease while another peak is observed at λ_{max} = 610 nm (λ_{ex} = 360 nm) in agreement with the orange emission

observed. Comparison of XRD patterns before and after griding suggest the structural

change under the applied pressure when grinding.
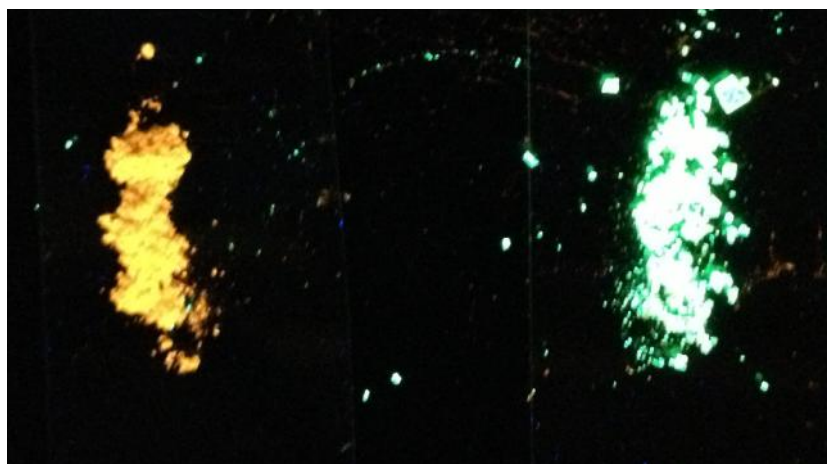
Figure 106: Photos showing the luminescence change of CuI(*2,6-dimethylpyrazine*) after

and before griding.
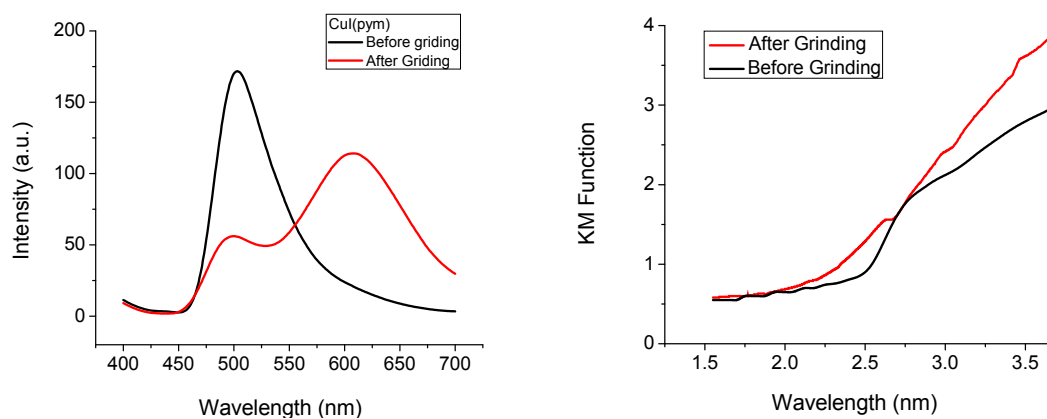
Figure 107: (left) PL changes of CuI(*2,6-dimethylpyrazine*) before and after grinding. (right)

UV changes of CuI(*2,6-dimethylpyrazine*) before and after grinding.
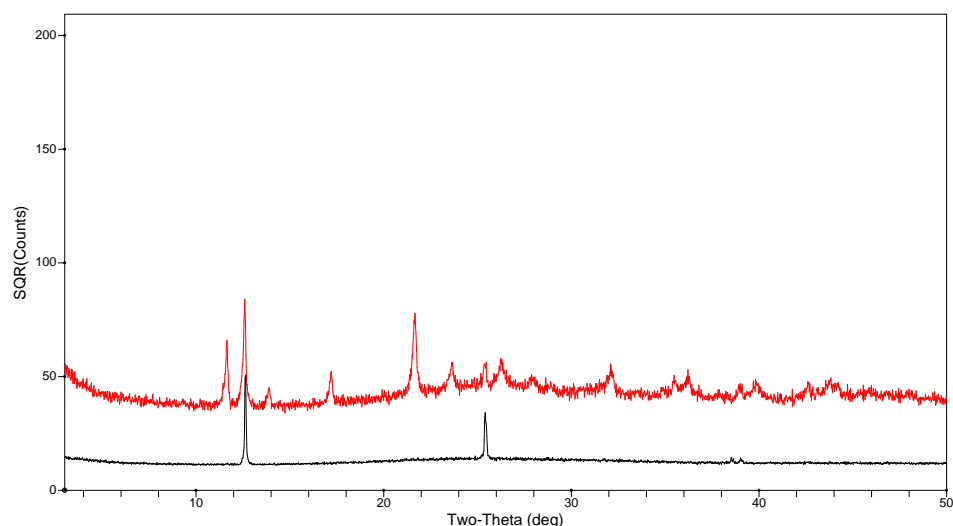
Figure 108: Comparison of XRD patterns before (black) and after (red) griding.

4.4 Summary

In summary, we have developed a novel class of I-VII inorganic organic hybrid semiconductors. A number of new 1D-CuI(*L*) (*L* = organic ligand) inorganic organic hyrbid materials were acquired under solvent diffusion method and their crystal structures were solved. The 1D-CuI(*L*) hybrid structures display tunable optical absorption and emission behavior and some of the structures such as CuI(*3-bromopyridine*) and CuI(*5-bromopyrimidine*) are able to give close-to–white-light photoluminesence. The DFT calulation results of selected 1D-CuI(*L*) structures show that the valance band is contributed by the atomic orbitals in inorganic modules while the

conduction band is determined by LUMO of organic ligands. By adjusting the functional group on the organic molecules, their LUMO energy levels as well as the band gap of hybrid structures can be systematically tuned. This discovery further lead us to design 1D-CuI(*L*) structures with mixed ligand to get white light emission. Eventually, we have prepared pyrimidine substituted CuI(*pyridine*) crystals which can emit strong and pure white light with CIE coordinates of (0.31, 0.33).

References

(1)   Mitzi, D. B. *Adv Mater* **2009**, *21*, 3141.

(2)   Ingham, B.; Chong, S. V.; Tallon, J. L. *J. Phys. Chem. B* **2005**, *109*, 4936.

(3)   Chen, D. L.; Wen, H. J.; Chen, H. M.; Wang, H. L.; Zhang, R.; Xu, H. L.; Yang, D. Y.; Lu, H. X. *Mater. Chem. Phys.* **2009**, *116*, 507.

(4)   Gauthron, K.; Lauret, J. S.; Doyennette, L.; Lanty, G.; Al Choueiry, A.; Zhang, S. J.; Brehier, A.; Largeau, L.; Mauguin, O.; Bloch, J.; Deleporte, E. *Opt Express* **2010**, *18*, 5912.

(5)   Wu, M.; Rhee, J.; Emge, T. J.; Yao, H. B.; Cheng, J. H.; Thiagarajan, S.; Croft, M.; Yang, R. G.; Li, J. *Chem. Commun.* **2010**, *46*, 1649.

(6)   Huang, X. Y.; Li, J.; Fu, H. X. *J. Am. Chem. Soc.* **2000**, *122*, 8789.

(7)   Huang, X. Y.; Li, J.; Zhang, Y.; Mascarenhas, A. *J. Am. Chem. Soc.* **2003**, *125*, 7049.

(8)   Huang, X. Y.; Li, J. *J. Am. Chem. Soc.* **2007**, *129*, 3157.

(9)   Huang, X. Y.; Roushan, M.; Emge, T. J.; Bi, W. H.; Thiagarajan, S.; Cheng, J. H.; Yang, R. G.; Li, J. *Angew Chem Int Edit* **2009**, *48*, 7871.

(10)   Yao, H. B.; Zhang, X. A.; Wang, X. H.; Yu, S. H.; Li, J. *Dalton T* **2011**, *40*, 3191.

(11)   Roushan, M.; Zhang, X.; Li, J. *Angew Chem Int Edit* **2012**, *51*, 436.

(12)   Ki, W.; Li, J. *Journal of the American Chemical Society* **2008**, *130*, 8114.

(13)   Sleight, A. W. *Endeavour* **1995**, *19*.

(14)   Zhang, Y.; Islam, Z.; Ren, Y.; Parilla, P. A.; Ahrenkiel, S. P.; Lee, P. L.; Mascarenhas, A.; McNevin, M. J.; Naumov, I.; Fu, H. X.; Huang, X. Y.; Li, J. *Phys Rev Lett* **2007**, *99*.

(15)   Jing Li, W. B., Wooseok Ki, Xiaoying Huang, and Srihari Reddy *J. Am. Chem. Soc.* **2007**, *129* 14140.

(16)   Zhang, X.; Ren, Y.; Roushan, M.; Li, J. *Eur J Inorg Chem* **2012**, 5966.

(17)   Chernova, N. A.; Roppolo, M.; Dillon, A. C.; Whittingham, M. S. *J. Mater. Chem.* **2009**, *19*, 2526.

(18)   Zheng, H. D.; Ou, J. Z.; Strano, M. S.; Kaner, R. B.; Mitchell, A.; Kalantar-Zadeh, K. *Adv. Funct. Mater.* **2011**, *21*, 2175.

(19)   Esposito, D. V.; Forest, R. V.; Chang, Y. C.; Gaillard, N.; McCandless, B. E.; Hou, S. Y.; Lee, K. H.; Birkmire, R. W.; Chen, J. G. G. *Energ Environ Sci* **2012**, *5*, 9091.

(20)   Tacca, A.; Meda, L.; Marra, G.; Savoini, A.; Caramori, S.; Cristino, V.; Bignozzi, C. A.; Pedro, V. G.; Boix, P. P.; Gimenez, S.; Bisquert, J. *Chemphyschem* **2012**, *13*, 3025.

(21)   Mao, A.; Kim, J. K.; Shin, K.; Wang, D. H.; Yoo, P. J.; Han, G. Y.; Park, J. H. *J Power Sources* **2012**, *210*, 32.

(22)   Mi, Q. X.; Zhanaidarova, A.; Brunschwig, B. S.; Gray, H. B.; Lewis, N. S. *Energ Environ Sci* **2012**, *5*, 5694.

(23)   Ho, G. W.; Chua, K. J.; Siow, D. R. *Chem Eng J* **2012**, *181*, 661.

(24)   Zhang, K.; Shi, X. J.; Kim, J. K.; Park, J. H. *Phys Chem Chem Phys* **2012**, *14*, 11119.

(25)   Liu, X.; Wang, F. Y.; Wang, Q. *Phys Chem Chem Phys* **2012**, *14*, 7894.

(26)   Goncalves, R. H.; Leite, L. D. T.; Leite, E. R. *Chemsuschem* **2012**, *5*, 2341.

(27)   Hsiao, P. T.; Chen, L. C.; Li, T. L.; Teng, H. S. *J Mater Chem* **2011**, *21*, 19402.

(28)   Su, J. Z.; Feng, X. J.; Sloppy, J. D.; Guo, L. J.; Grimes, C. A. *Nano Lett* **2011**, *11*, 203.

(29)   Ishihara, H.; Kannarpady, G. K.; Khedir, K. R.; Woo, J.; Trigwell, S.; Biris, A. S. *Phys Chem Chem Phys* **2011**, *13*, 19553.

(30)   Bar, M.; Weinhardt, L.; Marsen, B.; Cole, B.; Gaillard, N.; Miller, E.; Heske, C. *Appl Phys Lett* **2010**, *96*.

(31)   Alexander, B. D.; Kulesza, P. J.; Rutkowska, I.; Solarska, R.; Augustynski, J. *J Mater Chem* **2008**, *18*, 2298.

(32)   Wang, H. L.; Deutsch, T.; Turner, J. A. *J Electrochem Soc* **2008**, *155*, F91.

(33)   Gratzel, M. *Nature* **2001**, *414*, 338.

(34)   Santato, C.; Ulmann, M.; Augustynski, J. *J. Phys. Chem. B* **2001**, *105*, 936.

(35)   Zheng, H. D.; Tachibana, Y.; Kalantar-zadeh, K. *Langmuir* **2010**, *26*, 19148.

(36)   Xia, Q.; Zhao, H. L.; Du, Z. H.; Wang, J.; Zhang, T. H.; Wang, J.; Lv, P. P. *J Power Sources* **2013**, *226*, 107.

(37)   Fu, X. M. *Rare Metal Mat Eng* **2012**, *41*, 488.

(38)   Sasidharan, M.; Gunawardhana, N.; Noma, H.; Yoshio, M.; Nakashima, K. *B Chem Soc Jpn* **2012**, *85*, 642.

(39)   Tang, W.; Liu, L. L.; Zhu, Y. S.; Sun, H.; Wu, Y. P.; Zhu, K. *Energ Environ Sci* **2012**, *5*, 6909.

(40)   Meduri, P.; Clark, E.; Kim, J. H.; Dayalan, E.; Sumanasekera, G. U.; Sunkara, M. K. *Nano Lett* **2012**, *12*, 1784.

(41)   Liang, Q. Q.; Li, Y. M.; Li, J. H. *J Nanosci Nanotechno* **2012**, *12*, 2839.

(42)   Saji, V. S.; Lee, C. W. *Chemsuschem* **2012**, *5*, 1146.

(43)   Sen, U. K.; Mitra, S. *Rsc Adv* **2012**, *2*, 11123.

(44)   Li, S.; Han, C. H.; Mai, L. Q.; Han, J. H.; Xu, X.; Zhu, Y. Q. *Int J Electrochem Sc* **2011**, *6*, 4504.

(45)   Liu, X. L.; He, Y. H.; Wang, S. L.; Zhang, Q. *J Alloy Compd* **2011**, *509*, S408.

(46)   Xue, X. Y.; Chen, Z. H.; Xing, L. L.; Yuan, S.; Chen, Y. J. *Chem Commun* **2011**, *47*, 5205.

(47)   Dewangan, K.; Sinha, N. N.; Sharma, P. K.; Pandey, A. C.; Munichandraiah, N.; Gajbhiye, N. S. *Crystengcomm* **2011**, *13*, 927.

(48)   Kang, J. H.; Paek, S. M.; Choy, J. H. *B Korean Chem Soc* **2010**, *31*, 3675.

(49)   Mai, L. Q.; Xu, L.; Han, C. H.; Xu, X.; Luo, Y. Z.; Zhao, S. Y.; Zhao, Y. L. *Nano Lett* **2010**, *10*, 4750.

(50)   Mohan, V. M.; Bin, H.; Chen, W. *J Solid State Electr* **2010**, *14*, 1769.

(51)   Mai, L. Q.; Xu, L.; Hu, B.; Gu, Y. H. *J Mater Res* **2010**, *25*, 1413.

(52)   Yang, L. C.; Guo, W. L.; Shi, Y.; Wu, Y. P. *J Alloy Compd* **2010**, *501*, 218.

(53)   Scanlon, D. O.; Watson, G. W.; Payne, D. J.; Atkinson, G. R.; Egdell, R. G.; Law, D. S. L. *J Phys Chem C* **2010**, *114*, 4636.

(54)   Riley, L. A.; Lee, S. H.; Gedvilias, L.; Dillon, A. C. *J Power Sources* **2010**, *195*, 588.

(55)   Gao, Q. S.; Yang, L. C.; Lu, X. C.; Mao, J. J.; Zhang, Y. H.; Wu, Y. P.; Tang, Y. *J Mater Chem* **2010**, *20*, 2807.

(56)   Tong, W.; Yoon, W. S.; Hagh, N. M.; Amatucci, G. G. *Chem Mater* **2009**, *21*, 2139.

(57)   Lee, S. H.; Kim, Y. H.; Deshpande, R.; Parilla, P. A.; Whitney, E.; Gillaspie, D. T.; Jones, K. M.; Mahan, A. H.; Zhang, S. B.; Dillon, A. C. *Adv Mater* **2008**, *20*, 3627.

(58)   Yang, L. C.; Gao, Q. S.; Tang, Y.; Wu, Y. P.; Holze, R. *J Power Sources* **2008**, *179*, 357.

(59)   Dillon, A. C.; Mahan, A. H.; Deshpande, R.; Parilla, R.; Jones, K. M.; Lee, S. H. *Thin Solid Films* **2008**, *516*, 794.

(60)   Yang, L. C.; Gao, Q. S.; Zhang, Y. H.; Tang, Y.; Wu, Y. P. *Electrochem Commun* **2008**, *10*, 118.

(61)   Reddy, C. V. S.; Qi, Y. Y.; Jin, W.; Zhu, Q. Y.; Deng, Z. R.; Chen, W.; Mho, S. I. *J Solid State Electr* **2007**, *11*, 1239.

(62)   Zhang, M.; Jiao, L. F.; Yuan, H. T.; Wang, Y. M.; Guo, J.; Zhao, M.; Wang, W.; Zhou, X. D. *Solid State Ionics* **2006**, *177*, 3309.

(63)   Wang, L. Q.; Jiao, L. F.; Yuan, H. T.; Guo, J.; Zhao, M.; Li, H. X.; Wang, Y. M. *J Power Sources* **2006**, *162*, 1367.

(64)   Wen, Z. H.; Wang, Q.; Li, J. H. *J Nanosci Nanotechno* **2006**, *6*, 2117.

(65)   Kerr, T. A.; Wu, H.; Nazar, L. F. *Chem Mater* **1996**, *8*, 2005.

(66)   Spahr, M. E.; Novak, P.; Haas, O.; Nesper, R. *J Power Sources* **1995**, *54*, 346.

(67)   Anilkumar, K. R.; Parveen, A.; Badiger, G. R.; Prasad, M. V. N. A. *Ferroelectrics* **2009**, *386*, 88.

(68)   Blake, A. J.; Brooks, N. R.; Champness, N. R.; Cooke, P. A.; Deveson, A. M.; Fenske, D.; Hubberstey, P.; Li, W. S.; Schroder, M. *J Chem Soc Dalton* **1999**, 2103.

(69)   Niu, Y. Y.; Song, Y. L.; Zhang, N.; Hou, H. W.; Che, D. J.; Fan, Y. T.; Zhu, Y.; Duan, C. Y. *Eur J Inorg Chem* **2006**, 2259.

(70)   Lu, J. Y.; Cabrera, B. R.; Wang, R. J.; Li, J. *Inorg Chem* **1999**, *38*, 4608.

(71)   Graham, P. M.; Pike, R. D.; Sabat, M.; Bailey, R. D.; Pennington, W. T. *Inorg Chem* **2000**, *39*, 5121.

(72)   Hou, Q.; Qu, X. J.; Jin, J.; Zhao, J. J.; Yu, J. H.; Xu, J. Q. *J Clust Sci* **2011**, *22*, 715.

(73)   Hu, S.; Yu, F. Y.; Yan, Y.; Hao, Z. F.; Yu, L.; Tong, M. L. *Inorg Chem Commun* **2011**, *14*, 622.

(74)   Cullity, B. D. *Elements of X-ray Difffraction-Second Edition.*

(75)   Goodwin, A. L. *J. Am. Chem. Soc.* **2005**, *127*, 17980.

(76)   Sleight, A. W. *Annu. Rev. Mater. Sci.* **1998**, *28*, 29.

(77)   Likubo, S. K., K.; Takenaka, K.; Takagi, H.; Takigawa, M.; Shamoto, S. *Phys. Rev. Lett.* **2008**, *101*, 205901.

(78)   Shirane, G. T., A. *J. Phys. Soc. Jpn.* **1951**, *7*, 1.

(79)   Shirane, G. H., S. *J. Phys. Soc. Jpn.* **1951**, *6*, 265.

(80)   Holcombe, C. E. S., D. D. *J. Am. Ceram. Soc* **1978**, *61*, 163.

(81)   Evans, J. S. O. M., T. A.; Vogt, T.; Subramanian, M. A.; Sleight, A. W *Chem. Mater.* **1996**, *8*.

(82)   Mary, T. A. E., J. S. O.; Vogt, T.; Sleight, A. W *Science* **1996**, *272*, 90.

(83)   Lind, C. W., A. P.; Hu, Z. B.; Short, S.; Jorgensen, J. D *Chem. Mater.* **1998**, *10*, 2335.

(84)   Korthuis, V. K., N.; Sleight, A. W.; Roberts, N.; Dupree, R.;Warren, W. W *Chem. Mater.* **1995**, *7*, 412.

(85)   Evans, J. S. O. M., T. A.; Sleight, A. W *J. Solid State Chem* **1997**, *133*, 580.

(86)   Lightfoot, P. W., D. A.; Maple, M. J.; Villaescusa, L. A.; Wright,P. A *J. Mater. Chem.* **2001**, *11*, 212.

(87)   Williams, D. J. P., D. E.; Lincoln, F. J.; Kouvetakis, J.; O'Keeffe,M *J. Solid State Chem* **1997**, *134*, 164.

(88)   Benjamin K. Greve, K. L. M., Peter L. Lee, Peter J. Chupas, Karena W. Chapman, and Angus P. Wilkinson* **2010**, *132*.

(89)   Tao, J. Z. S., A. W *J. Solid State Chem* **2003**, *173*, 45.

(90)   Karena W. Chapman, P. J. C., and Cameron J. Kepert *J. Am. Chem. Soc.* **2005**, *127*, 15630.

(91)   Serena Margadonna, K. P., and Andrew N. Fitch *J. Am. Chem. Soc.* **2004**, *126*, 15390.

(92)   Karena W. Chapman, P. J. C., ‡ and Cameron J. Kepert *J. Am. Chem. Soc.* **2006**, *128*, 7009.

(93)   Jayaraman, A. B., E.; Dernier, P. D.; Longinotti, L. D *Phys. Rev. Lett.* **1973**, *31*, 700.

(94)   Arvanitidis, J. P., K.; Margadonna, S.; Prassides, K.; Fitch, A. N *Nature* **2003**, *425*, 599.

(95)   Keller-flaig, R. A., E. *Adv. Eng. Mater.* **2002**, *4*.

(96)   Takenaka, K. T., H. *Appl. Phys. Lett.* **2009**, *94*.

(97)   Salvador, J. R. G., F.; Hogan, T.; Kanatzidis, M. G. *Nature* **2003**, *425*, 702.

(98)   Fluegel, B. Z., Y.; Mascarenhas, A.; Huang, X. Y.; Li, J. *Phys. Rev. B* **2004**, *70*.

(99)   Huang, X. Y. H. I., H. R.; Le, V.; Li, J. *Chem. Mater.* **2001**, *13*.

(100)   Huang, X. Y. L., J.; Fu, H. *J. Am. Chem. Soc.* **2000**, *122*.

(101)   Huang, X. Y. L., J.; Zhang, Y.; Mascarenhas, A. *J. Am. Chem. Soc.* **2003**, *125*, 7049.

(102)   Huang, X. Y. L., J. *J. Am. Chem. Soc.* **2007**, *129*.

(103)   Huang, X. Y. R., M.; Emge, T.J.; Bi, W.; Thiagarajan, S.; Cheng, J.; Yang, R.; and Li, J. *Angew. Chem. Int. Ed.* **2009**, *48*.

(104)   Y. Zhang, Z. I., Y. Ren, P. A. Parilla, S. P. Ahrenkiel, P. L. Lee, A. Mascarenhas, M. J. McNevin, I. Naumov,H.-X. Fu, X.-Y. Huang, and J. Li *Phys. Rev. Lett.* **2007**, *99*, 215901.

(105)   Zhang, Y. D., G.M.; Fluegel, B.; Wei, S.H.; Mascarenhas, A.; Huang, X. Y.; Li, J.; Wang, L.W. *Phys. Rev. Lett.* **2006**, *96*.

(106)   Lee, S. H.; Deshpande, R.; Parilla, P. A.; Jones, K. M.; To, B.; Mahan, A. H.; Dillon, A. C. *Adv. Mater.* **2006**, *18*, 763.

(107)   Xu, Y.; Lu, J. J.; Goh, N. K. *J Mater Chem* **1999**, *9*, 1599.

(108)   Hagrman, P. J.; LaDuca, R. L.; Koo, H. J.; Rarig, R.; Haushalter, R. C.; Whangbo, M. H.; Zubieta, J. *Inorg. Chem.* **2000**, *39*, 4311.

(109)   Yan, B. B.; Xu, Y.; Goh, N. K.; Chia, L. S. *Chem. Commun.* **2000**, 2169.

(110)   Fluegel, B.; Zhang, Y.; Mascarenhas, A.; Huang, X.; Li, J. *Phys Rev B* **2004**, *70*.

(111)   Fu, H. X.; Li, J. *J. Chem. Phys.* **2004**, *120*, 6721.

(112)   Waser, R.; Böttger, U.; Tiedke, S. *Polar Oxides WILEY-VCH Verlag GmbH & Co.* **2005**

(113)   Bergh, A.; Craford, G.; Duggal, A.; Haitz, R. *Physics Today* **2001**, *54*, 42.

(114)   Bowers, M. J.; McBride, J. R.; Rosenthal, S. J. *Journal of the American Chemical Society* **2005**, *127*, 15378.

(115)   Hines, M. A.; Guyot-Sionnest, P. *J Phys Chem B* **1998**, *102*, 3655.

(116)   Mueller, A. H.; Petruska, M. A.; Achermann, M.; Werder, D. J.; Akhadov, E. A.; Koleske, D. D.; Hoffbauer, M. A.; Klimov, V. I. *Nano Lett* **2005**, *5*, 1039.

(117)   Nag, A.; Sarma, D. D. *J Phys Chem C* **2007**, *111*, 13641.

(118)   Yang, W. J.; Luo, L. Y.; Chen, T. M.; Wang, N. S. *Chem Mater* **2005**, *17*, 3883.

(119)   Ki, W. L., J. *J. Am. Chem. Soc.* **2008**, *130*.

(120)   Liu, Z. W.; Qayyum, M. F.; Wu, C.; Whited, M. T.; Djurovich, P. I.; Hodgson, K. O.; Hedman, B.; Solomon, E. I.; Thompson, M. E. *Journal of the American Chemical Society* **2011**, *133*, 3700.